ELSEVIER

Surface Science Reports 32 (1998) 1–90

surface science reports

Oxide surfaces and metal/oxide interfaces studied by grazing incidence X-ray scattering

Gilles Renaud[1]

CEA-Grenoble, Département de Recherche Fondamentale sur la Matière Condensée, Service de Physique des Matériaux et des Microstructures[2], Interfaces et Rayonnement Synchrotron, 17, rue des Martyrs, 38054 Grenoble Cédex 9, France

Manuscript received in final form 23 April 1998

Abstract

Experimental determinations of the atomic structure of insulating oxide surfaces and metal/oxide interfaces are scarce, because surface science techniques are often limited by the insulating character of the substrate. Grazing incidence X-ray scattering (GIXS), which is not subject to charge effects, can provide very precise information on the atomic structure of oxide surfaces: roughness, relaxation and reconstruction. It is also well adapted to analyze the atomic structure, the registry, the misfit relaxation, elastic or plastic, the growth mode and the morphology of metal/oxide interfaces during their growth, performed in situ. GIXS also allows the analysis of thin films and buried interfaces, in a non-destructive way, yielding the epitaxial relationships, and, by variation of the grazing incidence angle, the lattice parameter relaxation along the growth direction. On semi-coherent interfaces, the existence of an ordered network of interfacial misfit dislocations can be demonstrated, its Burger's vector determined, its ordering during in situ annealing cycles followed, and sometimes even its atomic structure can be addressed. Careful analysis during growth allows the modeling of the dislocation nucleation process.

This review emphasizes the new information that GIXS can bring to oxide surfaces and metal/oxide interfaces by comparison with other surface science techniques. The principles of X-ray diffraction by surfaces and interfaces are recalled, together with the advantages and properties of grazing angles. The specific experimental requirements are discussed. Recent results are presented on the determination of the atomic structure of relaxed or reconstructed oxide surfaces. A description of results obtained during the in situ growth of metal on oxide surfaces is also given, as well as investigations of thick metal films on oxide surfaces, with lattice parameter misfit relaxed by an array of dislocations. Recent work performed on oxide thin films having important physical properties such as superconductivity or magnetism is also briefly reviewed.

The strengths and limitations of the technique, such as the need for single crystals and surfaces of high crystalline quality are discussed. Finally, an outlook of future prospects in the field is given, such as the study of more complex oxide surfaces, vicinal surfaces, reactive metal/oxide interfaces, metal oxidation processes, the use of surfactants to promote wetting of a metal deposited on an oxide surface or the study of oxide/liquid interfaces in a non-UHV environment.

[1] Tel.: +33 4 76 88 35 58; fax: +33 4 76 88 51 38; e-mail: grenaud@cea.fr.

[2] Laboratory associated with the Joseph Fourier University of Grenoble.

0167-5729/98/$ – see front matter
PII: S0167-5729(98)00005-3

1. Introduction

Oxide surfaces [1–5] and metal/oxide interfaces [6–10] are involved in various technologically important areas such as composites, protective coatings, thin film technology, electronic as well as nuclear combustible and waste packaging, heterogeneous catalysis, gas sensors and the glass industry. Interfaces where either the metal or the oxide has magnetic properties are of growing interest, since they may find applications in future devices for magnetic recording. The electrical, mechanical, chemical or thermal properties of many technologically important devices are often intimately related to the structure, composition and morphology of internal metal/oxide interfaces, which in turn depend on the structure of the oxide surface.

It is now a widely accepted idea [11] that scientific computing will become a major research field in the future. It will allow predicting the properties of materials before they are elaborated, and thus development of new technological materials with specific properties may be expected. However, before this is achieved, the theoretical models used in numerical simulations need to be very detailed and have proven accuracy.

Whereas theoretical models allowing the prediction of the surface or interface structure are now fairly well developed in the case of metals and semiconductors, much less is known about oxide surfaces because of their ionic character, and about metal/oxide interfaces because of the complexity of the bonding between such dissimilar materials. The interfacial energy is composed of competing terms, which often have the same order of magnitude. In particular, an important component is believed to be the image interaction [12]. In the recent years, the matter has drawn a number of theoretical contributions [13–15] and the development of more powerful computers resulted in improvements in the microscopic modeling of these surfaces and interfaces [16–18].

One of the major objectives of experiments on oxide surfaces and metal/oxide interfaces is to determine some parameters that allow testing the theoretical models.

Among the questions one would like to address on *oxide surfaces*, one may ask:

- Is the surface "ideal", or does it have defects? Is it stoichiometric or does it have vacancies? Are there steps, regular or not, on the surface? Is the surface free of any contaminants (like carbon)? How to remove them?
- What is the equilibrium structure and morphology of the surface: is it a simple truncation of the bulk, or is it relaxed or reconstructed? How well do the available theories predict this structure? How is it affected by defects or by different surface treatments, for instance annealing in oxygen partial pressure or ion sputtering?
- What are the different reconstructions undergone by an oxide surface upon reduction by heating in UHV? Can these different surface reconstructions be predicted theoretically?
- Are polar surfaces (according to the definition of Tasker [19]) unstable or can they be stabilized by a reconstruction?
- How does the surface evolve upon exposure to different gases (H_2, CO, NO, H_2O, CO_2, NO_2, etc); does the surface dissociate water?
- Are there general trends between similar surfaces?

The questions one would like to address on *metal/oxide interfaces* are also numerous:

- Is the interface reactive?

- What is the equilibrium morphology of the interface?
- What is the growth mode: layer-by-layer (2D or Van-der-Merwe), 2D followed by 3D (Stranski–Krastanov), three-dimensional (3D or Volmer–Weber), or 2D for a fraction of the first monolayer, followed by 3D (2DI) [20]? How are the growth mode and the structure of the metallic overlayer affected by the characteristics of the oxide surface listed above?
- What are the growth kinetics and how is the growth mode modified by changing the substrate temperature or the flux of incoming atoms? Can the growth be modified by a surfactant, like oxygen or carbon monoxide?
- What are the structure and morphology of the growing film, and their evolution as a function of thickness, substrate temperature and incoming flux? When does the film start to coalesce; when does it become continuous? Is there epitaxy? What are the orientational relationships between the growing film and the substrate?
- What are the epitaxial sites and the interfacial distance between the last oxide plane and the first metal atomic plane?
- How is the lattice parameter mismatch between the substrate and the adsorbate accommodated as a function of the film thickness?
- Are there growth defects such as stacking faults, twins or dislocations in the growing film? When and why do they appear? More generally, what is the crystalline quality of the film? Can it be improved either with the help of a surfactant or by changing the growth temperature or by post-annealing?

Metal/oxide interfaces may be prepared by very different routes, such as internal oxidation of alloys, hot pressure bonding, sputtering, laser ablation, etc. We will restrict ourselves here to those prepared under ultra high vacuum (UHV) conditions, by molecular beam epitaxy (MBE) on well-characterized and clean oxide surfaces. More and more studies have been devoted to oxide surfaces and metal/oxide interfaces prepared under "clean" conditions in the recent years. A few model surfaces have been selected both by theoreticians and by experimentalists, either because of their simplicity, because of their important applications, or because of their availability as large single crystals. Among them, α-Al_2O_3, MgO, TiO_2, ZnO and $SrTiO_3$ surfaces are the most studied. Theoreticians have also chosen model metal/oxide interfaces, like Ag/MgO(0 0 1) or Pd/MgO(0 0 1), and minimized the interfacial energy with respect to two structural parameters, the epitaxial site and the interfacial distance, for which they crucially need experimental determination. Other oxides have also been studied to a less extent, such as: CaO, CeO_2, ZrO_2, Cr_2O_3, Fe_2O_3, Fe_3O_4, WO_2, NiO, CuO, Ga_2O_3, SnO_2, etc.

Despite this fast growing interest, often little is known of the structure and morphology of oxide surfaces and metal/oxide interfaces because of the difficulty to quantitatively characterize insulator surfaces and interfaces with the usual surface science techniques based on electron beams or tunneling effects. The atomic force microscope (AFM) usually lacks the required atomic resolution to characterize the atomic structure of insulators. Alternative techniques exist, like the scattering of beams of neutral atoms, He for instance, but they are only sensitive to the top atomic layer of the surface, and thus cannot probe buried interfaces. One way of avoiding charging effects is to prepare ultra-thin oxide films (for instance of Al_2O_3, Fe_2O_3, Fe_3O_4, Cr_2O_3, NiO, CoO, etc.) on conducting substrates, thus allowing the use of all surface science techniques, including the scanning tunneling microscope (STM). However, these thin films often have a large density of defects (vacancies, interstitials, dislocations,

domain walls, different phases and variants, grain and sub-grain boundaries, etc.), which may completely change their electronic properties and thus also their macroscopic properties. It is thus often mandatory to work on single crystals either to preserve given properties, such as a large gap and a high resistivity, or to control the type and the density of defects which may play a dominant role on the interfacial properties.

We will try to show in this review the power of the grazing incidence X-ray scattering (GIXS) technique to characterize single-crystal oxide surfaces and metal/oxide interfaces. Since its discovery [21] GIXS has emerged over the past decade as a new tool for studying the structure of surfaces and interfaces [22–30]. This probe has several advantages with respect to the more conventional electron based surface techniques such as low-energy electron diffraction (LEED) and reflection high-energy electron diffraction (RHEED). X-rays interact weakly with matter, so that in most cases, a simple quantitative analysis based on a single scattering (kinematic) calculation can be performed, while multiple-scattering effects dominate electron diffraction. Moreover, X-rays penetrate deeply in matter, enabling the study of buried interfaces. In addition, the scattering cross section is very well known for all atoms. X-ray diffraction peaks can be measured with very high resolution and over a large intensity range, thus enabling detailed lineshape analyses that are not accessible with other diffraction techniques. GIXS also benefits from the huge amount of work performed in conventional 3D crystallography, and hence allows the determination of the atomic structure of surfaces and interfaces with high accuracy. GIXS is especially suited to investigate the structure and morphology of oxide surfaces, because, unlike most surface techniques, it is not subject to charge build-up due to the insulating character of the surface.

The large intensity of today's synchrotron radiation sources allows getting measurable diffraction from less than one monolayer (ML) of material. The grazing incidence geometry can drastically reduce the X-ray penetration in matter, down to ~ 25 Å, and thus the unwanted bulk elastic and inelastic (i.e. Compton, Resonant Raman, Fluorescence, Thermal Diffuse) scattering with respect to the measured surface or interface elastic scattering [26]. Even under incidence conditions different from total external reflection, the surface sensitivity can be achieved by measuring diffraction rods that are specific to the surface, such as non-integer reflections arising from a surface reconstruction.

This review is organized as follows. The basis of X-ray scattering under grazing incidence will first be summarized. The diffraction by a surface will next be considered, with methods to quantitatively determine its atomic structure (roughness, relaxation or reconstruction), and to analyze the degree of order using lineshape analysis. The diffraction by an epilayer/substrate interface will next be recalled, with the possibilities to determine the registry and the lattice parameter relaxation on coherent interfaces, or analyze the interfacial network of dislocations in the case of semi-coherent interfaces. A few experimental considerations will next be given, in particular the sample requirements to obtain reliable quantitative measurements.

Several recent determinations of the atomic structure, relaxation or reconstructions of clean oxide surfaces will next be described. They will be followed by a review of several in situ studies of the first stages of formation of metal/oxide interfaces, and next by the investigations of thick metal films on oxides, exhibiting a network of interfacial dislocations that plastically relax the lattice parameter mismatch. A quick overview of the characterization of diverse oxide thin films by GIXS will next be given before concluding on the present and future possibilities of the technique applied to the field of oxide surfaces and metal/oxide interfaces.

2. X-ray scattering by surfaces and interfaces

2.1. Grazing incidence X-rays

2.1.1. Grazing incidence geometry

The grazing incidence X-ray scattering geometry, shown in Fig. 1, is identical to the three-dimensional case, except that, in order to decrease the bulk scattering contributions, the incident X-ray beam, of wavevector $\boldsymbol{k}_i$, is kept at a glancing incidence angle α_i with respect to the surface. The scattered beam, of wavevector $\boldsymbol{k}_f$, is detected at an angle α_f with respect to the sample surface and at an in-plane angle 2θ with respect to the transmitted beam. The momentum transfer is defined as $\boldsymbol{Q} = \boldsymbol{k}_f - \boldsymbol{k}_i$, and is often decomposed into two components, $\boldsymbol{Q}_{//}$ and $\boldsymbol{Q}_\perp$, respectively, parallel and perpendicular to the surface. The absolute value of $\boldsymbol{Q}_\perp$ is a function of α_i and α_f: $Q_\perp = k(\sin\alpha_i + \sin\alpha_f)$; $k = 2\pi/\lambda$, where λ is the wavelength. When α_i and α_f are very small, $\boldsymbol{Q} \sim \boldsymbol{Q}_{//}$, the scattering plane is nearly parallel to the surface, and diffracting net planes are perpendicular to it. The scattering geometry being defined by the incident beam and detector directions, one has only to rotate the sample about its surface normal to bring these net planes into diffraction condition, which occurs when they make an angle θ with respect to both the incident and the scattered beam. In this way, the long-range periodicity parallel to the surface is probed. It is often useful to measure the scattered intensity as a function of $Q_\perp$, which is often achieved by increasing α_f while keeping grazing incidence.

2.1.2. Refraction of X-rays at grazing angles

Because the incidence angle is small, it is necessary to consider the effects of refraction at the surface [31]. The refractive index, n, of matter for X-rays is slightly less than unity,

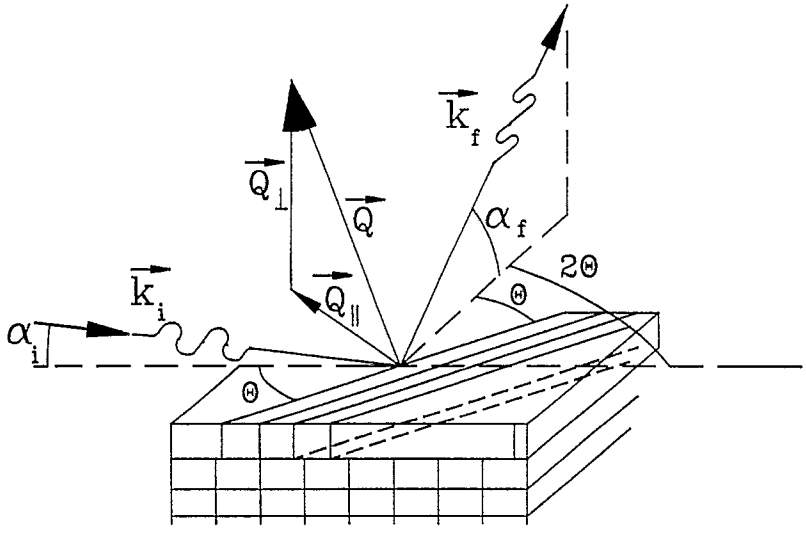

Fig. 1. Grazing incidence X-ray scattering geometry. All notations are defined in the text.

$n = 1 - \delta + i\beta$, with:

$$\delta = \frac{1}{2\pi}\frac{e^2}{mc^2}\frac{N_a \sum_i (Z_i - f_i')}{\sum_i A_i}\rho\lambda^2 = 2.701 \times 10^{-6}\frac{\sum_i (Z_i - f_i')[\text{el.units}]}{\sum_i A_i[\text{g/mol}]}\rho[\text{g/cm}^3]\lambda^2[\text{Å}], \quad (1)$$

$$\beta = \frac{1}{2\pi}\frac{e^2}{mc^2}\frac{N_a \sum_i f_i''}{\sum_i A_i}\rho\lambda^2 = \mu\frac{\lambda}{4\pi}, \quad (2)$$

where N_a is Avogradro's number, the summation is over all atomic species i; $(Z_i - f_i')$, f_i'' and A_i are, respectively, the scattering factor, the anomalous dispersion factor and the atomic weight of the i species, ρ is the density, λ the wavelength and μ the photoelectric absorption coefficient. Because of refraction, the transmitted beam is closer to the surface. When α_i is smaller than a critical value α_c, the beam is totally reflected, and only an evanescent wave, which decays over tens of angstroms, is present below the surface. When α_i is larger than the critical angle for total external reflection, the transmitted wave propagates. Typical orders of magnitude are: $\delta \sim 10^{-5}$ and $\beta \sim 10^{-6}$, so that $\alpha_c \sim (2\delta)^{1/2} \sim 0.1°$ to 0.5°. Due to time microreversibility, identical refractive effects occur as a function of the exit angle α_f.

2.1.3. *Scattering depth*

The perpendicular components of the incident and emergent wave vectors are modified upon crossing the surface and become complex due to refraction and absorption:

$$k'_{i,f,\perp} = \frac{2\pi}{\lambda}(A_{i,f} - iB_{i,f}),$$

where $A_{i,f}$ and $B_{i,f}$ are given by the following expressions, valid for small incidence and emergence angles:

$$A_{i,f} = \frac{1}{\sqrt{2}}\left(\sqrt{(\alpha_{i,f}^2 - \alpha_c^2)^2 + 4\beta^2} + \alpha_{i,f}^2 - \alpha_c^2\right)^{1/2}$$

and

$$B_{i,f} = \frac{1}{\sqrt{2}}\left(\sqrt{(\alpha_{i,f}^2 - \alpha_c^2)^2 + 4\beta^2} + \alpha_c^2 - \alpha_{i,f}^2\right)^{1/2} \quad (3)$$

and hence the perpendicular momentum transfer inside the sample $Q'_\perp = k'_{f\perp} - k'_{i\perp}$ becomes complex. The scattering depth given by

$$\Lambda = \frac{1}{\text{Im}(Q'_\perp)} = \frac{\lambda}{4\pi(B_i + B_f)} \quad (4)$$

is thus strongly affected by refraction when α_i or α_f are close to α_c. Fig. 2 shows the variation of the scattering depth as a function of α_i/α_c for different values of α_f/α_c. When $\alpha_i \ll \alpha_c$, and $\alpha_f \ll \alpha_c$, the scattering depth is of the order of tens of angstroms; it increases rapidly to thousands of angstroms when α_i and α_f are larger than α_c, through a transition region where $\Lambda \sim 100$ Å. The incidence and exit angles thus allow control of the depth contributing to a given measurement, which can be varied from ~ 10 to 1000 Å.

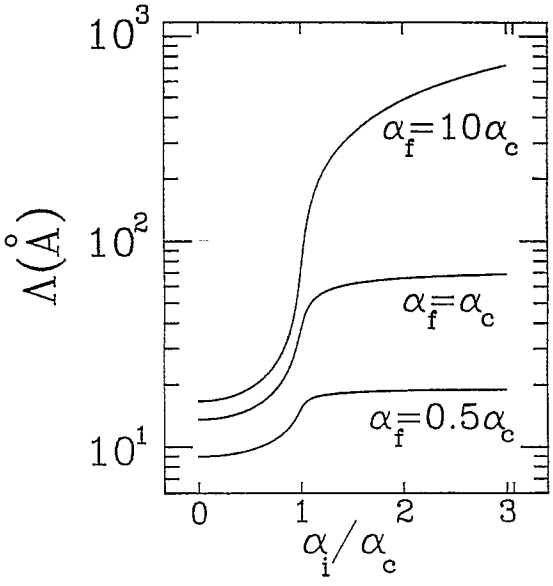

Fig. 2. Variation of the scattering depth as a function of the incidence angle, for three exit angles, equal to half, one time and ten times the critical angle, for a Pt surface and 1.5 Å wavelength.

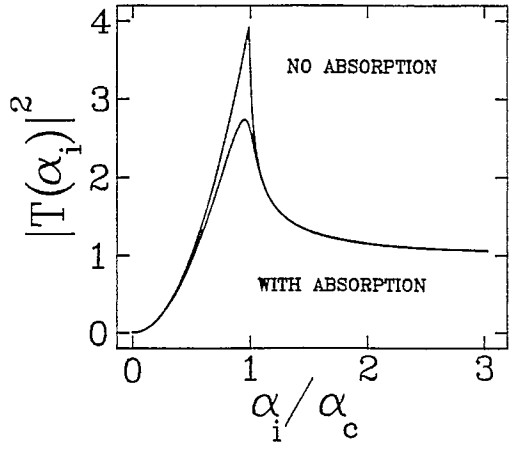

Fig. 3. Intensity transmission coefficient for a Pt surface and 1.5 Å wavelength, with and without considering absorption.

The reflection and transmission coefficients for the intensity are also strongly affected by refraction, according to:

$$R_{i,f}=\frac{\alpha_{i,f}^2-2\alpha_{i,f}A_{i,f}+A_{i,f}^2+B_{i,f}^2}{\alpha_{i,f}^2+2\alpha_{i,f}A_{i,f}+A_{i,f}^2+B_{i,f}^2} \quad \text{and} \quad T_{i,f}=\frac{4\alpha_{i,f}^2}{\alpha_{i,f}^2+2\alpha_{i,f}A_{i,f}+A_{i,f}^2+B_{i,f}^2}. \tag{5}$$

The variation of the transmission coefficient as a function of $\alpha_{i,f}$ is reported in Fig. 3. Below $\alpha_c, R_{i,f}=1$ is the regime of total external reflection. At α_c, the transmission coefficient is maximum

($T = 4$). This property is sometimes used in GIXS: α_i and/or α_f can be fixed at α_c, in order to enhance the surface scattering.

2.2. *Basic X-ray diffraction*

We recall briefly the basic expression of the intensity scattered by a three-dimensional crystal. The reader may refer to standard textbooks [32] for a more comprehensive introduction.

Since the interaction of hard X-rays with matter is small, the kinematical approximation of single scattering is valid in most cases, except for perfect crystals near Bragg scattering. The intensity scattered by a block-shaped crystal with N_1, N_2 and N_3 unit cells along the three crystal axes defined by the vectors $\boldsymbol{a}_1$, $\boldsymbol{a}_2$ and $\boldsymbol{a}_3$ takes the form:

$$I(\boldsymbol{Q}) = AF^2(\boldsymbol{Q})S^2_{N_1}(\boldsymbol{Q}\cdot\boldsymbol{a}_1)S^2_{N_1}(\boldsymbol{Q}\cdot\boldsymbol{a}_2)S^2_{N_3}(\boldsymbol{Q}\cdot\boldsymbol{a}_3) \tag{6}$$

where A is a constant and

$$S_N(\boldsymbol{Q}\cdot\boldsymbol{a}_j) = \sum_{n=0}^{N-1} \exp(\mathrm{i}\boldsymbol{Q}\cdot\boldsymbol{a}_j \cdot n), \quad j = 1,2,3. \tag{7}$$

$F(\boldsymbol{Q})$ is the structure factor, which is expressed as a function of atomic positions $\boldsymbol{r}_j$ within the unit cell as

$$F(\boldsymbol{Q}) = \sum_{j \text{ unit cell}} f_j \exp(\mathrm{i}\boldsymbol{Q}\cdot\boldsymbol{r}_j), \tag{8}$$

where f_j is the scattering factor (or atomic form factor) of atom j, and

$$S^2_{N_j}(\boldsymbol{Q}\cdot\boldsymbol{a}_j) = \frac{\sin^2(N_j\boldsymbol{Q}\cdot\boldsymbol{a}_j/2)}{\sin^2(\boldsymbol{Q}\cdot\boldsymbol{a}_j/2)}, \quad j = 1,2,3, \tag{9}$$

is the interference function of N_j diffracting units. The intensity is thus the product of the structure factor, which only depends upon the structure within the unit cell, and the form factor, related to the shape of the crystal. In the limit of large N, the S_N function tends to a periodic array of Dirac delta functions with Q spacing of $2\pi/a$, i.e. the intensity is non-zero only if $\boldsymbol{Q}\cdot\boldsymbol{a}_1 = 2\pi h$, $\boldsymbol{Q}\cdot\boldsymbol{a}_2 = 2\pi k$ and $\boldsymbol{Q}\cdot\boldsymbol{a}_3 = 2\pi l$, with h, k, l integers. In other words, the intensity is non-zero only if $\boldsymbol{Q}$ is a vector of the reciprocal lattice of basic vectors $\boldsymbol{b}_1$, $\boldsymbol{b}_2$ and $\boldsymbol{b}_3$, i.e. $\boldsymbol{Q} = h\boldsymbol{b}_1 + k\boldsymbol{b}_2 + l\boldsymbol{b}_3$. When this Laue condition is fulfilled, the intensity is given by

$$I_{hkl} = AF^2_{hkl}N_1^2N_2^2N_3^2. \tag{10}$$

The structure factor now takes the form:

$$F_{hkl} = \sum_{j \text{ unit cell}} f_j \exp[2\pi\mathrm{i}(hx_j + ky_j + lz_j)] \exp\, -M_j. \tag{11}$$

The summation extends over all atoms of the unit cell; f_j, x_j, y_j, z_j, M_j are, respectively, the scattering factor, fractional coordinates in the unit cell and Debye–Waller factor of atom j.

2.3. Diffraction by a surface

2.3.1. Rods of scattering from a reconstructed surface

Consider now a quasi-2D crystal of finite thickness. The basic cell vector a_3 perpendicular to the surface is chosen equal to this thickness. This crystal is handled by setting $N_3 = 1$ in Eq. (6). The diffraction is then still sharply peaked in both directions parallel to the surface, but the Laue condition on $Q_3 (= Q_\perp)$ is relaxed, and the intensity is continuous in the out-of-plane direction: the reciprocal space is made of rods perpendicular to the surface plane (Fig. 4). If we still define l by $\boldsymbol{Q}\cdot\boldsymbol{a}_3 = 2\pi l$, l is now taken as a continuous variable since intensity is present for non-integer values of l. The intensity is now given by:

$$I^{2D}_{hkl} = AF^2_{hkl}N_1^2N_2^2. \tag{12}$$

The intensity variation along the rod (i.e. as a function of Q_3 or l) is solely contained in the structure factor; it is thus related to the z-coordinates of the atoms within the unit-cell of this quasi-2D crystal. In general, the rod modulation period gives the thickness of the distorted layer and the modulation amplitude is related to the magnitude of the normal atomic displacements. This is the case of a reconstructed surface, for which rods are found for fractional order values of h and k, i.e. outside scattering from the bulk.

2.3.2. Ideal surface: crystal truncation rod (CTR)

A crystal truncated by a sharp surface (or semi-infinite crystal) can be represented by the product of a step function describing the electron density variation as a function of z, the coordinate perpendicular to the surface, and an infinite lattice. The diffraction pattern is then the convolution of the 3D reciprocal lattice with the Fourier transform of the step function. An infinity of Fourier components is necessary to build this latter, so that there remains non-zero intensity in between Bragg peaks as a function of l: the reciprocal space is made of rods of intensity, called crystal truncation rods (CTR), extending perpendi-

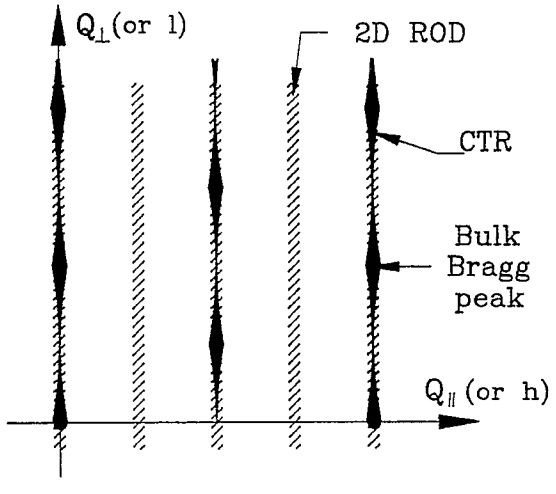

Fig. 4. Schematic representation of the reciprocal space of a quasi-2D crystal giving rise to continuous rods of diffraction (shaded rods), and of a 3D crystal truncated by a surface, giving rise to the crystal truncation rods (black filled) with maximum intensity at the bulk Bragg positions and quickly varying intensity in between.

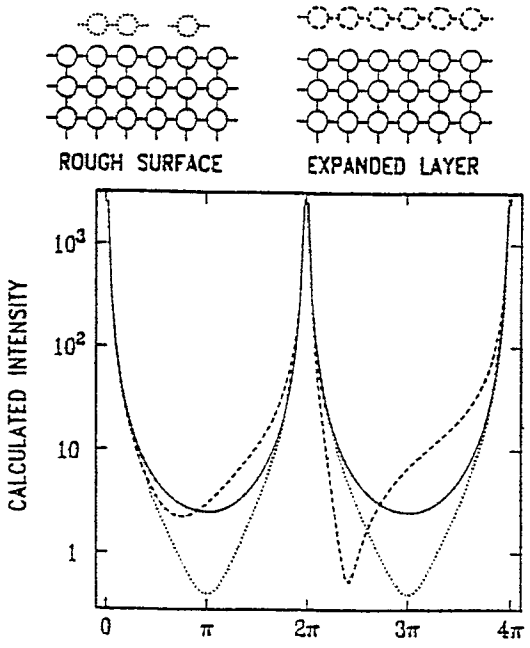

Fig. 5. Intensity variation along a crystal truncation rod, as a function of the out-of-plane phase shift $\boldsymbol{Q}\cdot\boldsymbol{a}_3 = 2\pi l$. The full curve shows the CTR profile for a perfectly sharp surface, as calculated in Eq. (13); the dotted curve shows the profile for a rough surface (i.e. exactly covered by half a monolayer) and the broken curve for a surface with an expansion of 10% of the last interplanar distance (reprinted from Ref. [22]).

cular to the surface, and connecting bulk Bragg peaks [33,34]. They are schematically represented in Fig. 4. The intensity variation as a function of Q_3 (or $Q_\perp$ or l) can be found by replacing $S_{N_3}(Q_3a_3)$ by $\sum_{n_3=-\infty}^{n_3=0}\exp(\mathrm{i}Q_3a_3n_3)$ in Eq. (6), which gives

$$I(\boldsymbol{Q}) = I_{hkl}^{\mathrm{CTR}} = \frac{\sin^2(N_1a_1Q_1/2)\sin^2(N_2a_2Q_2/2)}{\sin^2(a_1Q_1/2)\sin^2(a_2Q_2/2)}|F_{hkl}|^2|F_{\mathrm{CTR}}(Q_3)|^2$$

with

$$|F_{\mathrm{CTR}}(Q_3)| = \frac{1}{2\sin(Q_3a_3/2)}. \tag{13}$$

The intensity variation of $F_{\mathrm{CTR}}(Q_3)$ as a function of l is shown in Fig. 5. Bragg peaks are found for integer values of l, but there remains some intensity in between, even when l is a multiple of half-integer, i.e. when successive net planes scatter out-of phase. At these anti-node positions, I_{hkl}^{CTR} and I_{hkl}^{2D} have comparable magnitudes, the intensity diffracted by the semi-infinite lattice is of the order of the intensity diffracted by a single monolayer.

2.3.3. *Rough surface*

If the surface is rough on an atomic scale, the step function has to be replaced by a less abrupt function, which needs fewer Fourier components to be built, so that the intensity of the CTRs between Bragg peaks is smaller than for a perfectly sharp surface. As the roughness increases, the intensity

between Bragg peaks is reduced, and the result for an infinite 3D crystal is approached. Let us choose the lattice parameter perpendicular to the surface a_3 as being the interplanar distance in this direction. Let $\theta(p)$ be the occupancy of an atomic plane located at the height $z = pa$, i.e. the probability to find an atom at this height. The CTR term of the intensity is given by

$$F_{\mathrm{CTR}} = \sum_{p=-\infty}^{\infty} \theta(p) \mathrm{e}^{\mathrm{i}2\pi lp} \tag{14}$$

A simple model of the function $\theta(p)$, which yields an analytical solution, has been given by Robinson [34] by choosing

$$\theta(p) = \beta^p \quad \text{for } p > 0 \quad \text{and} \quad \theta(p) = 1 \quad \text{for } p \leq 0 \tag{15}$$

with $0 \leq \beta < 1$, we find:

$$|F_{\mathrm{CTR}}(l)| = (1-\beta)^2/(1+\beta^2-2\beta\cos(2\pi l)). \tag{16}$$

This model allows a fast calculation, and is sufficient in many cases to represent the data. However, it yields a discontinuity in electron density at $p = 0$, and gives significant occupancies for planes which are far away from the mean surface when the roughness is large. An alternative model consists in a Gaussian discrete distribution of terrace heights, hence modeling $\theta(p)$ by a complementary error function. The intensity must then be numerically estimated. For small deviation Δl with respect to the Bragg peak, the effect is analogous to a Debye–Waller factor [35]:

$$|F_{\mathrm{CTR}}(l)| \approx \mathrm{e}^{-\Delta l^2 \sigma^2}, \tag{17}$$

where σ is the root-mean-square roughness, in number of planes.

The sensitivity to roughness is illustrated in Fig. 5 where a CTR intensity profile is shown as a function of l for a perfectly sharp surface and for a surface covered by exactly half a monolayer. At anti-node position ($l = 1/2$), the uncovered surface (half monolayer) of the semi-infinite crystal interferes destructively with the top half monolayer, so that the intensity is strongly reduced with respect to the flat surface case.

2.3.4. *Relaxed surface*

The measurement of CTRs allows the determination of the atomic structure of a surface, or of an interface between two materials. The intensity variation along CTRs between two Bragg peaks, as a function of l, is particularly sensitive to the difference between the bulk and surface structures. Let us take for instance a surface whose last interplanar distance is b instead of a_3: the CTR structure factor is given by

$$F_{hkl}^{\mathrm{CTR}} = \left(\frac{\mathrm{e}^{\mathrm{i}\pi l}}{2\mathrm{i}\sin(\pi l)} + \mathrm{e}^{\mathrm{i}2\pi lb/a} \right). \tag{18}$$

This produces a large asymmetry of the CTR intensity around Bragg peaks, as illustrated in Fig. 5 for $b/a = 1.1$. The larger the maximum value of the perpendicular momentum transfer, the larger the interference term and thus the asymmetry, and the better the accuracy on this relaxation.

This extreme sensitivity of CTRs to the surface atomic structure has been used to determine the relaxation of the MgO(0 0 1), α-Al_2O_3(0 0 0 1) and TiO_2(1 1 0) surfaces, as will be shown in Section 4, as well as the structure of the Ca-segregated MgO(0 0 1) surface.

2.3.5. Integrated intensities

The above expressions of the scattered intensity show that, in general, the reflections have a finite width, which is related to the finite size of the crystal. In order to deduce the structure factor, containing the required structural information at the atomic level, the pertinent measurement is to integrate the intensity of each reflection according to

$$\int_{Q_{//}} I(\boldsymbol{Q}_{//} + \boldsymbol{Q}_{\perp})\, \mathrm{d}\boldsymbol{Q}_{//} = N_1 N_2 |F_{HK,l}|^2 |F_{\mathrm{CTR}}(l)|^2, \tag{19}$$

where H and K are integers and l is a continuous variable.

This is in general done by performing a scan along one direction, while integrating along the perpendicular direction, using sufficiently opened slits, i.e. an adapted resolution function. Several corrections have next to be applied, the Lorentz correction, due to the relationship between the reciprocal space coordinates and the angular coordinates, the polarization correction, which accounts for the polarization state of the incoming wave, the background correction, the normalization to the input intensity, and the illuminated active area correction. The statistical error bars are also estimated during this procedure, and systematic errors are determined through measurements of several equivalent reflections, related by symmetry. This procedure can be fairly complicated, in particular for surface rods or CTRs, for which the finite width of the rods, their rapidly varying intensity or the exact surface diffractometer resolution function have to be estimated properly. Although they are still in development, the simplest features of these correction procedures may be found in many recent references [22,36–42].

The corrected intensities are proportional to the square of the structure factors, with an arbitrary scale factor, which will have to be determined as a free parameter (unless absolute intensities are measured). A determination of the atomic structure of a reconstruction requires the quantitative measurement of as many allowed reflections as possible. Given the structure factors, standard Fourier methods of crystallography, such as Patterson function or electron-density difference function are used. The experimental Patterson function is the Fourier transform of the experimental intensities, which is directly the electron density–density autocorrelation function within the unit cell:

$$P(\boldsymbol{r}) = \sum_{hkl} |F_{hkl}|^2 \exp(-\mathrm{i}\boldsymbol{Q}\cdot\boldsymbol{r}) = \int \rho(\boldsymbol{r})\rho(\boldsymbol{r}+\boldsymbol{r}')\, \mathrm{d}^3\boldsymbol{r}' = \langle \rho(\boldsymbol{r})\rho(0)\rangle. \tag{20}$$

For in-plane measurements at $l = 0$, because of Friedel's law: $|F_{h,k,l=0}| = |F_{-h,-k,l=0}|$, the Patterson function $P(\boldsymbol{r})$ is real, and reduces to:

$$P(\boldsymbol{r}) = 2\sum_{hkl} |F_{hk}|^2 \cos[2\pi(hx + ky)].$$

Practically, a peak in the Patterson map means that the vector joining the origin to this peak is an interatomic vector of the atomic structure. Different techniques may be combined to deconvolute the Patterson map [43]. On the basis of a set of interatomic vectors obtained from a contour plot of the Patterson map, a trial structure can be derived and model structure factor amplitudes calculated and compared with experiment. This is in general followed by a least-squares minimization of the difference between the calculated and measured structure factors. Two kinds of functions may be minimized: the chi-squared factor χ^2 which allows one to properly take into account the experimental uncertainties

$\sigma^2_{F^{exp}_{hkl}}$ on the measured structure factors and the number p of parameters in the model, and the reliability factor R. They are given by

$$\chi^2 = \frac{1}{N-p}\sum_{hkl}\frac{(|F^{exp}_{hkl}| - |F^{calc}_{hkl}|)^2}{\sigma^2_{F^{exp}_{hkl}}} \quad \text{and} \quad R = \frac{\sum_{hkl}||F^{exp}_{hkl}| - |F^{calc}_{hkl}||}{\sum_{hkl}|F^{exp}_{hkl}|}, \tag{21}$$

where the summation is over the N measured diffraction peaks, hkl. A good agreement is obtained when $\chi^2 \sim 1$ or when $R \approx (1/N)\sum_{hkl}(\sigma_{F^{exp}_{hkl}}/|F^{exp}_{hkl}|)$, in which case no new parameter should be added to the model. Of help in the process of structure determination may be the difference Fourier map, which is a difference between the calculated electron density for the model structure, and the electron density obtained by a Fourier transform of the experimental structure factors, but by assigning them the phase calculated from the model. When the model is close to the real structure, this approximation may be valid, and yield a direct picture of excess or missing electron density in the unit cell. It may thus be very useful to refine a model.

Several examples will be given in this review of the determination of the projected atomic structure of a surface reconstruction, for instance for the α-$Al_2O_3(0\,0\,0\,1)(\sqrt{31}\times\sqrt{31})R\pm 9°$ and the NiO(1 1 1)-p(2 × 2) reconstructions.

2.3.6. Lineshape analysis

The above expression of the scattered intensity shows that in general, the surface diffraction peaks have a finite width, which is related to the finite "domain size" parallel to the surface. In the $Q_1 (= 2\pi h/a_1)$ direction, for instance, the peaks have a finite width $\Delta h \sim 1/N_1$. The "domain size" in this in-plane direction can be approximated by $D = N_1 a_1$, and is thus simply related to the peak full width at half maximum (FWHM) $\Delta\omega$ by

$$D = \frac{a_1}{\Delta h} \quad \text{or} \quad D = \frac{2\pi}{Q_{//}\Delta\omega}, \tag{22}$$

where $\Delta\omega$ is the in-plane angular width of the reflection, measured by rocking the sample around its surface normal. D represents the maximum distance between two atoms that scatter coherently, i.e. the average distance between surface defects such as steps, vacancies, stacking faults, dislocations, grain boundaries; etc. that perturb the long-range atomic order, since this distance is smaller than the X-ray coherence length in this direction. This notion of "domain size" is more rigorously described by a lateral correlation function $C(\boldsymbol{r}_{//})(C(r \to 0) = 1, C(r \to \infty) = 0)$, defined as the probability that two atoms separated by $\boldsymbol{r}_{//}$ scatter coherently. The scattered intensity may be written accordingly as

$$I(\boldsymbol{Q}) = |F_{hkl}|^2\,|F_{CTR}|^2\frac{A}{A_u^2}\left(\sum_{H,K}\delta(h-H)\delta(k-K)\right)\int_{\boldsymbol{r}_{//}} C(\boldsymbol{r}_{//})e^{i\boldsymbol{Q}_{//}\boldsymbol{r}_{//}}\,d\boldsymbol{r}_{//}, \tag{23}$$

where A is the active area and A_u the unit cell area. This shows that the lineshape of in-plane diffraction peaks corresponds to the Fourier transform of the lateral correlation function. The correlation function is in general taken as a simple analytical form: Gaussian or exponential. In the case of a Gaussian correlation function $C(r) = e^{-r^2/2L^2}$ and for a transverse scan integrated in the perpendicular direction, the intensity is given by

$$I(\boldsymbol{Q} + \Delta Q\boldsymbol{t}) = |F_{hkl}|^2|F_{CTR}|^2\frac{A}{A_u^2}(2\pi)^{3/2}Le^{-\Delta Q^2L^2/2}, \tag{24}$$

where $\boldsymbol{t} = (\boldsymbol{Q}_\perp \times \boldsymbol{Q}_{//})/\|\boldsymbol{Q}_\perp\| \, \|\boldsymbol{Q}_{//}\|$ is the transverse direction. The diffraction peak is thus also of Gaussian lineshape, with a root mean square value $1/L$, i.e. of FWHM given by

$$\Delta Q = 2\sqrt{2\ln 2}\frac{1}{L} \quad \Rightarrow \quad \Delta h = \sqrt{2\ln 2}\frac{a_1}{\pi L} \quad \text{and} \quad \Delta\omega = 2\sqrt{2\ln 2}\frac{1}{QL}. \tag{25}$$

In the case of an exponential correlation function $C(r) = \mathrm{e}^{-r/L}$, the intensity is written:

$$I(\boldsymbol{Q} + \Delta Q\boldsymbol{t}) = |F_{hkl}|^2 |F_{\mathrm{CTR}}|^2 \frac{A}{A_u^2}\frac{2a_2}{L}\frac{1}{1/L^2 + \Delta Q^2}. \tag{26}$$

The lineshape is thus Lorentzian, of FWHM:

$$\Delta Q = \frac{2}{L} \quad \Rightarrow \quad \Delta h = \frac{a_1}{\pi L} \quad \text{and} \quad \Delta\omega = \frac{2}{LQ} \tag{27}$$

and the "domain size" D is related to the correlation length L by $D = \pi L$.

In practice, before analyzing the lineshape in terms of correlation lengths, it has to be deconvoluted from the instrumental resolution function and from other contributions such as a mosaic spread or a distribution of lattice parameters parallel to the surface. This is in general done by measuring the lineshape for different orders of reflection, and in both directions, longitudinal and transverse to the momentum transfer. While a finite correlation function yields peaks of constant shape in reciprocal space, whatever the parallel momentum transfer value $Q_{//}$, a mosaic spread or a distribution of lattice parameters yield, respectively, a transverse and a longitudinal broadening proportional to $Q_{//}$. Several examples of lineshape analyses will be given (Section 5.2) in the cases of Ag/MgO, Pd/MgO, Fe/MgO and Ni/MgO interfaces.

2.4. *Diffraction by an epilayer/substrate interface*

2.4.1. *Reciprocal lattice of an epilayer/substrate interface*

Fig. 6 qualitatively shows the intensity scattered by an epilayer on top of a substrate, as a function of the in plane and out-of plane momentum transfers. The semi-infinite crystal yields CTRs, and the epilayer yields rods of intensity, which may be peaked at different $Q_\perp$ values if the out-of plane unit vector of the epilayer differs from the bulk one, or at different $Q_{//}$ values if the epilayer is laterally incoherent. This allows independent analysis of the epilayer structural properties, such as in plane and out-of plane relaxation, without interference with the substrate. The epilayer rod intensity distribution is broad in $Q_\perp$ because of the finite thickness of the epilayer, but sharply peaked in plane. The parallel and perpendicular strain relaxation in the epilayer can be analyzed separately by performing respectively $Q_{//}$ scans (such as scans 2 of Fig. 6) around in plane Bragg peaks and $Q_\perp$ scans (such as scans 1 of Fig. 6) around out-of-plane Bragg peaks. Examples of such measurements will be given in the case of different metal/MgO(0 0 1) interfaces in Section 5.2.

2.4.2. *Semi-coherent interfaces*

For incoherent but commensurate epilayers with large lattice parameter mismatches parallel to the interface, the film may be completely relaxed by an array of periodic misfit dislocations located at the interface or a few atomic planes away. This network of dislocations produces a supercell whose in-plane parameter is the average distance between two dislocations, but whose out-of-plane parameter is the

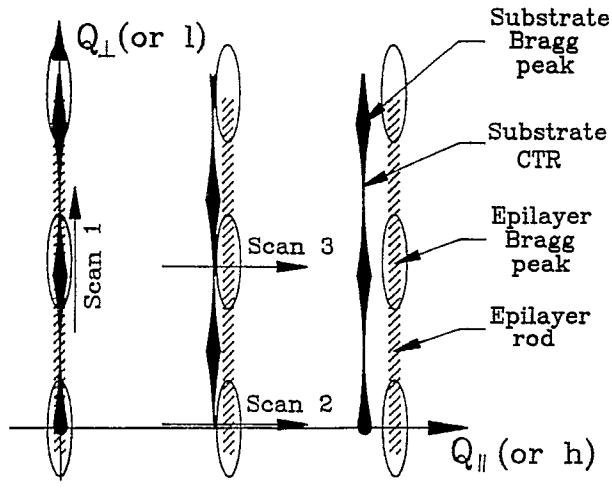

Fig. 6. Schematic representation of the reciprocal space of a substrate with an incoherent epilayer. Vertical dashed lines are the epilayer rods, which have peaks represented by ellipses; substrate CTRs are also represented. Scan 1, 2 and 3 are referred to in the text.

whole film thickness. This dislocation array will produce in-plane satellite peaks in reciprocal space, in addition to the substrate and epilayer diffraction peaks. If the lattice parameter of the film is smaller (respectively larger) than the one of the substrate, these satellites will be more intense at the low (respectively high)-Q side of the epilayer Bragg peak because the dislocations expand (respectively contract) the film lattice to match the substrate. These satellites should be rod-like if the film is sufficiently thin, and their intensity variation as a function of $Q_\perp$ is related to the curvature of the net planes near the dislocation. At $Q_\perp = 0$, the intensity is mostly sensitive to the deformation field far from the dislocation cores, while it becomes more sensitive to the dislocation core when $Q_\perp$ is increased. In principle, a crystallographic analysis of the intensity of a large number of satellites should allow the determination of the atomic structure of the dislocation. However, only very few satellites, if any, can in general be measured, because either of poor long-range coherence of the structure or large diffuse scattering from both the substrate and the epilayer or small epilayer domain size. It is thus in general necessary to resort to modeling of the interfacial structure and atomic displacement field in the epilayer. Several examples of measurements on semi-coherent metal/oxide interfaces will be given in Section 5.3, and will illustrate the new information that can be gained by X-ray diffraction on the orientation and structure of the dislocations, which is very complementary with the HRTEM results. In addition, GIXS allows kinetics studies during annealing, which may bring new results on the energetic of the nucleation and motion of misfit dislocations.

2.4.3. *Coherent interface: epitaxial site and interfacial distance*

If the whole epilayer, or part of it, is constrained to the substrate lattice parameter parallel to the interfacial plane, the epilayer rods appear at the same $Q_{//}$ position as the substrate CTRs. Analysis of the intensity as a function of $Q_\perp$ (e.g. during scan 1 of Fig. 6) may yield the interfacial distance and the relation (registry) between the epilayer and the substrate. In general, the epilayer domain size is much smaller than that of the substrate, which results in much broader rods from the epilayer. However, in most cases, the structural analysis mentioned above can be performed, even when the film does not

contain a pseudomorphic fraction. Indeed, an interference appears between the substrate CTR and the overlayer scattering, which is only due to the small fraction of the deposited atoms that are perfectly on-site and correlated over long lateral distances via the substrate. This fraction is selected by Fourier filtering, by measurement of the scattering along the CTRs. The registry can then be deduced by analysis of this interference, as will be illustrated in detail in the cases of Ag/MgO(0 0 1) and Pd/MgO(0 0 1) interfaces in Section 5.2.

2.4.4. Structure and morphology during growth

In general, the structure and morphology of an epilayer on a substrate depend upon many parameters, such as the initial structure of the substrate surface itself, the equilibrium structure of the deposited material, the balance between its surface energy, that of the substrate and the interfacial energy, the lattice parameter misfit and the growth kinetics. Because several energy terms depend on the thickness of the epilayer, the structure and morphology are likely to evolve during growth. GIXS is one of the very rare tools that can be used in situ to follow the evolution of the structure and morphology during growth, from sub-monolayer deposits to fairly thick films (up to μm in thickness). In principle, the factors influencing the overlayer growth, such as the defect density of the substrate, its temperature during growth and the incoming fluxes can be systematically varied. The structure of the substrate, either reconstructed or relaxed, should be investigated first. Its average roughness can be deduced from analysis of the CTRs integrated intensities, and the surface domain size and average terrace width deduced from CTRs lineshape analyses. Systematic measurements during growth may then provide the evolution of the most important parameters with the overlayer thickness. These include the interfacial distance, the average in plane and out-of plane lattice parameters and strain distributions, the mosaic spread and the domain size both parallel and perpendicular to the interface. In the case of metal/ceramic interfaces, the growth is in general of the Volmer–Weber type, i.e. three-dimensional, and the domain size is directly related to the size of growing islands. These growing islands can also be studied in situ by grazing incidence small angle X-ray scattering (GISAXS) experiments. As will be shown in the case of the Ag/MgO(0 0 1) interface (Section 5.2.1), this recently developed technique [44–46] allows the determination of the average island height, lateral size and shape as well as the average separation between islands. It can thus provide useful information on the growth laws. It is often energetically favorable to introduce structural defects in a growing film, in particular in order to accommodate the lattice parameter mismatch. GIXS can also be used to analyze different growth defects such as stacking faults, twins and dislocation nucleation. Indeed, stacking faults are planar defects, and thus yield rods of scattering perpendicular to the plane of the fault; twinned crystals yield Bragg peaks that are related by mirror symmetry to those of the untwinned stacking. Finally, the nucleation of dislocations in the growing film leads to inhomogeneous deformations that may be detected through $Q_{//}$ scans.

3. Experimental considerations

3.1. X-ray sources

Although some GIXS experiments can be performed with laboratory X-ray sources such as rotating anodes, the use of synchrotron radiation is often required because of its high brightness, high energy

and angular resolution, and its energy tunability. Count rates more than 10^5 ph/s can be obtained from a monolayer on the undulator beamlines of third generation synchrotron radiation rings such as the ESRF (European Synchrotron Radiation Facility), with double focusing of the X-rays. Several such beamlines and associated UHV diffractometers dedicated to in situ GIXS experiments are operational [47–53].

3.2. *X-ray diffractometers coupled to ultra-high vacuum chambers*

Surface studies require the sample to be in ultra-high vacuum (UHV), so that the necessary vacuum hardware has to be combined with an X-ray diffractometer. The main difficulty is to associate the necessary precise orientation movements of the sample with a UHV environment. Several diffractometers devoted to performing GIXS have recently been built with these requirements [47–53].

The most recent diffractometers all allow one to define very precisely the different angles, in particular the incidence angle, and to vary the incidence and exit angles from 0 to 45°, thus allowing reaching large out-of plane momentum transfer values. They also are all equipped with standard surface preparation and thin film deposition tools. The GIXS experiments from our group were performed using different experimental setups: the W21 setup [53] at LURE (Laboratoire pour l'Utilisation du Rayonnement Electromagétique, Orsay, France), the ID3 [52] and ID32 setups [54] at the ESRF (European Synchrotron Radiation Facility, Grenoble, France) as well as the SUV apparatus of the French CRG/IF beamline (BM32) [55] at the ESRF.

We briefly describe here this latter apparatus, which is not only designed for GIXS, but also allows the simultaneous use of surface extended X-ray absorption spectroscopies (SEXAFS, ReflEXAFS) and X-ray reflectivity. The diffractometer consists of a large and well-equipped UHV chamber mounted on a four-circle diffractometer for X-ray studies, coupled to several other UHV chambers located outside the X-ray hutch. The diffractometer supports the UHV chamber described below, allowing a rotation of the whole chamber defining the incidence angle α of the X-ray beam with respect to the vertical sample surface. A goniometric head allows alignment (two perpendicular tilts χ_1 and χ_2, translations) of the sample inside vacuum. A rotary motion (ω) of the sample around its surface normal is obtained through the rotation of the whole goniometric head with use of a differentially pumped rotary feedthrough. Two sample surface orientations (parallel and perpendicular) with respect to the X-ray beam polarization are possible. Two circles of the diffractometer are devoted to the two detector rotations defining the Bragg angle projections δ parallel to the surface and the outgoing angle β with respect to the surface.

The X-ray UHV chamber, with a base pressure of 2×10^{-11} mbar, is equipped with two 0.5 mm thick beryllium windows required to let the X-ray beam enter and the scattered beam exit the chamber. STAIB 35 keV reflection high energy electron diffraction (RHEED) and auger electron spectroscopy (AES) facilities are available. It is also equipped with several (up to 5 simultaneously) deposition sources for in situ epitaxial deposition; with a Meca-2000 sample furnace reaching 900°C by radiative heating, and 1600°C by electron bombardment of the back of the sample, with a cold cathode AG5000 ion gun from Fisons instrument for ion sputtering (IS), with residual gas analysis (RGA), and a quartz micro-balance for calibration of metal deposition. All sample preparations and characterizations can be performed using this X-ray chamber, without moving the sample from its position for GIXS experiments.

The remaining apparatus is made of three UHV chambers located outside the X-ray experimental hutch, coupled with each other and with the X-ray UHV chamber via a long UHV transfer system. These three chambers are: (i) a RIBER MBE system devoted to nitride III–V semiconductors; (ii) a

characterization chamber equipped with quantitative low and medium energy electron diffraction, AES and IS; (iii) a UHV chamber equipped with a variable temperature scanning tunneling microscope (STM) and with IS. All these chambers are equipped with the same electron-beam bombardment furnace and have the same, transferable, sample holder system.

3.3. Data collection, correction and normalization

The procedures for data collection, correction and normalization depend on the characteristics of the input beam, on the geometry of the diffractometer and on the sample characteristics (mosaic spread, domain size). If the corrections on in-plane data are simple, they may be fairly complicated for rods with large out of plane momentum transfer values. The reader is referred to many recent papers on the subject [36–41]. In the case of the SUV diffractometer presented above, which is of the z-axis type, the corrections are given by the following:

Area correction: $A = (\sin\delta)^1$ as long as the active beam area is only limited by the input and exit slits parallel to the samples surface (i.e. vertical slits in the SUV case). When the illuminated area is limited either by the sample or by the input or exit slits perpendicular to the sample surface, a slightly more complicated expression is used.

Lorentz correction:

$$L = (\sin\delta\cos\alpha\cos\beta)^{-1}. \tag{28}$$

Horizontal component of the polarization:

$$P_h = 1 - (\sin\alpha\cos\delta\cos\beta + \cos\alpha\sin\beta)^2. \tag{29}$$

Vertical component of the polarization correction:

$$P_v = 1 - (\sin\delta\cos\beta)^2. \tag{30}$$

Rod correction:

$$R = \cos\beta. \tag{31}$$

Detector arm correction:

$$D = \cos\beta. \tag{32}$$

The total polarization correction is given by $P = \varepsilon P_h + (1-\varepsilon)P_v$, where ε is the degree of horizontal polarization of the X-ray beam, which is of the order of 95% in the BM32 beamline case of vertically focused synchrotron radiation from a bending magnet.

Note that, depending on the detailed resolution function (i.e. the presence of an analyzer on the detector arm, or of Soller slits, or of fairly closed slits), on the width and shape of the peaks to be integrated, and on the detailed shape of the focused input beam, several other correction factors may be necessary [36].

3.4. Sample requirements

One of the most important requirements to perform GIXS is the quality of the sample. The sample should be a good single crystal, at least over a thickness of several hundreds of angstroms below the

surface. The surface flatness (i.e. the width of the angular distribution of surface normal over long length-scale parallel to the surface) should be much smaller than the critical angle for total external reflection, i.e. typically smaller than 0.01°. In addition, in order to measure the CTRs over an extended range, the surface roughness should not exceed a few angstroms. These conditions are not trivial, and are often the limiting factor for successful experiments. It is often very difficult, for instance, to obtain simultaneously a small roughness and a good flatness by polishing. Even when this is achieved, it results in near surface hardening that may be removed by chemical etching, but at the expense of flatness. For metal or for semiconductors, well developed procedures are available to prepare surfaces of high quality, for instance by ion sputtering and annealing cycles or by deposition and annealing of a buffer layer. This is often not the case for the surfaces of oxides, which in addition are not always stoichiometric. As shown below, specific preparation procedures have thus to be developed.

4. Oxide surfaces

4.1. Specific considerations

Only a few oxide surfaces have been quantitatively investigated by GIXS: mainly the sapphire α-Al_2O_3(0 0 0 1) surface, the MgO(0 0 1) surface and the rutile TiO_2(1 1 0) surface. In these three cases, specific experimental considerations apply, in particular for the measurements of the CTRs, in order for instance to determine the atomic relaxation of the surface. The two first systems are very light scatterers, with an average number of electrons per atoms of 10. Therefore, in order to get measurable CTRs, the intensity needs to be concentrated over a very narrow angular range along these CTRs. This requires two conditions: first a very good starting single crystal, with a very small mosaic spread, and second a very flat surface on the length scale of the coherence length of the X-ray beam, that is typically 1 μm. These conditions are not trivial, since commercially available sapphire or MgO single crystal surfaces have rocking curve widths of the order of a few 0.01°, and rms roughness of typically 1 nm. For α-Al_2O_3 and MgO(0 0 1), both the bulk crystalline quality and the surface flatness can be improved by an annealing in air or under partial oxygen pressure at high temperature ($\sim$1500°C). The rocking curve full width at half maximum then decreases from $\sim$ 0.03° down to 0.0025° in the case of sapphire, and from $\sim$0.01° down to 0.0 0 1° in the case of MgO, thus yielding a ten-fold enhancement of the peak intensity along the CTRs, while leading to a negligible rms roughness, of less than 0.05 nm in the case of α-Al_2O_3(0 0 0 1) and less than 0.25 nm in the case of MgO(0 0 1). These rms roughness values were deduced from fits of the measured CTRs in both cases, and confirmed by AFM measurements. However, in both cases, the high temperature anneal has the drawback of enabling surface segregation of bulk impurities. This phenomenon can be minimized in the case of sapphire by limiting the duration of the annealing to a few hours, while Ca segregates on the MgO(0 0 1) surface. Another difficulty is the large noise due to the bulk of the sample. Indeed, if we wish to get a high accuracy on the atomic coordinates, it is necessary to measure the CTRs over an extended range of $Q_\perp$, which requires an X-ray beam of large enough energy. The energy was fixed at 23 keV for the α-Al_2O_3(0 0 0 1) surface, and 18 keV for the MgO(0 0 1) surface. At this energy, as soon as the incidence angle is larger or equal to the critical angle for total external reflection, a large background scattering is present, arising from bulk point defects and Compton scattering that overcomes the surface scattering. Consequently, the experiment must be performed under very stringent conditions, with the incident

Table 1
Main characteristics of the oxide surfaces and metal/oxide interfaces which have been studied by GIXS and are discussed in this review

Oxide substrate	Substrate preparation	Substrate state	r.m.s. substrate roughness	Overlayer	$\Delta a/a$ (%)	Deposit	Thickness range (ML)	Growth mode	Site	Interfacial distance (Å)	Epitaxial relationships	In-plane mosaic spread	Interfacial dislocations
TiO_2(1 1 0)	Cycles of Ar^+ sputtering and annealing to 1100 K, + cooling in O_2	(1×1), relaxed	Negligible on the (110) terraces										
TiO_2(0 0 1)	Polished, Ar^+ sputtering at 700°C, + annealing at 1100°C	(1×3)	5.6 Å										
α-Al_2O_3(0 0 0 1)	Polished, air-annealed at 1500°C + UHV anneal at 900°C	(1×1), relaxed	Negligible on the (0 0 0 1) terraces										
α-Al_2O_3(0 0 0 1)	Polished, air-annealed at 1500°C + UHV anneal at 1400°C	$(\sqrt{31} \times \sqrt{31})R \pm 9°$	Not measured										
α-Al_2O_3(0 0 0 1)	Polished, air-annealed at 1500°C + UHV anneal at 1300°C	$(3\sqrt{3} \times 3\sqrt{3})R30°$	Not measured										
$SrTiO_3$(0 0 1)	Cycles of Ar^+ sputtering and annealing at 900 K + anneal at 900 K in 1×10^{-6} mbar O_2	(1×1) and (1×6)											
MgO(0 0 1)	Polished, IB at 900°C + pO_2 at 700°C	(1×1) very small relaxation and rumple	6 Å	Ag	2.98	In situ MBE 10^{-9} mbar 1 Å/min, 300 K	0.5–30	2DI	O	2.43±0.1	(001)//(001) [100]//[100] [010]//[010]	~1° for thin films (<50 Å)	Yes above ~5 ML

MgO(0 0 1)	Polished, IB at 1550°C + pO_2 at 700°C	(1×1) very small relaxation and rumple	2.4 Å 6000 Å wide terraces	Ag	2.98	In site MBE 10^{-10} mbar 0.73 Å/min, 300 K	0.2–2500	VW	O	2.52±0.1	(001)//(001) [100]//[100] [010]//[010]	For 1500 Å thick, 0.25° before anneal, 0.1°after anneal 750°C	Yes above ~4 ML Ordered above 30 ML
MgO(0 0 1)	Polished, IB at 1550°C + pO_2 at 700°C	(1×1) very small relaxation and rumple	2.4 Å 6000 Å wide terraces	Pd	7.6	In situ MBE 10^{-9} mbar 1 Å/min, 300 K	0.2–183	VW	O	2.216±0.02	(001)//(001) [100]//[100] [010]//[010]	For 356 Å thick, 0.7°; 0.1° after anneal 750°C	Yes above ~5 ML
MgO(0 0 1)	Polished UHV annealed 800°C		?	Pd	7.6	Ex situ MBE 1 Å/s 873 K	2.5–200	?	?	?	(001)//(001) and (111)//(001) with four variants	?	Not detected
MgO (0 0 1)	Polished, IB at 1550°C + pO_2 at 700°C	(1×1) very small relaxation and rumple	2.4 Å 6000 Å wide terraces	Ni	16.4	In situ MBE 10^{-10} mbar 1 Å/min, 300 K	0.5–125	VW	O	?	(001)//(001) and (110)//(001) all variants	For 254 Å thick, 3.6°; 0.65° after anneal at 950°C for 1 h	Not ordered
MgO (0 0 1)	Polished, UHV heated at 360°C	Well ordered LEED pattern	High density of step edges	Fe	1.9	sputtering at 630 K 3 mTorr Ar 0.25 Å/s	1–200	VW	?	?	(001)//(001) and [110]/[100] [1$\bar{1}$0]//[010]	Neglected	Yes, not ordered
α-Al_2O_3 (0 0 0 1)	Polished, heated in UHV	1.4° miscut along [11$\bar{2}$0]	1.5 Å	Nb	1.9	Ex situ	86 Å Nb + 53 Å Nb oxide	Not studied	?	?	Nb(111)//Al_2O_3(0001), Nb[1$\bar{1}$0]//Al_2O_3[11$\bar{2}$0]	?	Yes, soliton-like
TiO_2(1 1 0)	Cycles of Ar^+ sputtering and annealing to 110 K + cooling in O_2	(1×1), relaxed		Cu			4 ML				(111)//(110)		

angle kept below the critical angle for total external reflection. Since in this region, the amplitude of the wavefield varies very rapidly with the incident angle, the diffractometer as well as the sample alignment have to be of the topmost quality. This of course also requires that the sample surface is very flat and well defined. In the case of TiO_2, the experiments seem to be less stringent, since titanium is a heavier scatterer, and very good single crystals, with low surface roughness are readily available from the suppliers. As soon as the atomic species become heavier, such as in the case of the NiO(1 1 1) surface, the above constrains relax dramatically. The intensity scattered by the surface is larger, and the bulk background decreases because the X-ray absorption is larger. Easy quantitative measurements were performed on sample having a 0.1° to 0.5° mosaic spread, while a very small mosaic spread is mandatory in the case of lighter metal-oxide surfaces.

The GIXS results presented below on different metal-oxide surfaces are summarized in Table 1.

4.2. *MgO(0 0 1) surface [56]*

The MgO(0 0 1) surface has been the object of numerous studies because it is widely used as a substrate for the epitaxial growth of metals [57–59] and as a model support for finely dispersed catalytic particles. It is also used as a substrate to grow high-temperature superconductors because of its close lattice match to $YBa_2Cu_3O_{7-x}$ and its low chemical reactivity. Since the detailed structure and morphology of the surface may play a significant role on the overlayer properties, developing well-defined procedures to prepare MgO surfaces of very high quality is of importance in a number of areas of surface physics and material science.

Getting a precise knowledge of the MgO(0 0 1) surface atomic structure is also important because this surface is often chosen as a model system for testing calculations on ionic oxides [60]. In particular, the top plane relaxation and the differential relaxation between anions and cations (rumpling) have been extensively studied, both theoretically [18,61–68] and experimentally [69–78]. These relaxations were always found extremely small on this surface. As shown below, when it is performed on a surface of very high quality, GIXS is well adapted for studying such small deviations from the ideally truncated surface.

The procedure for preparing surfaces of high quality necessarily involves a first step of annealing at high temperature (1500–1600°C). However, this annealing also results in a strong surface segregation of bulk impurities, mainly calcium. Despite numerous investigations [19,79–89], the atomic structure of the resulting Ca-segregated MgO(0 0 1) surface was still unresolved. GIXS was thus used first to analyze this Ca-segregated MgO(0 0 1) surface.

4.2.1. *Structure of the Ca-segregated MgO(0 0 1) surfaces [56]*

Atomic force microscopy (AFM) and fluorescence scanning electron microscopy (SEM) showed that the annealed MgO(0 0 1) surface was composed of very large terraces, several 1000 Å wide and running over distances of microns, separated either by monolayer high steps, or by steps that are several nanometers high. In addition, large, nearly equidistant "droplets" of hemispherical shape with diameter varying from 0.1 to 10 μm were found on these terraces. The droplets were found to have a rich chemical composition: Mg, P, Ca, Si, C, O and V, with ratios of ~ 100 : 60 : 30 : 15 : 10 : 3 : 1, respectively. In between, the terraces are atomically flat. Outside the droplets, on the flat surface, only Ca, in a quantity of about one monolayer, was detected.

Low energy electron diffraction (LEED), AES and GIXS were performed in UHV. In addition to the main spots, which were very sharp, half order diffuse spots were present, corresponding to a

$(\sqrt{2} \times \sqrt{2})$R45° surface reconstruction. The atomic structure of this reconstruction was investigated by quantitative measurements and analysis of the MgO(0 0 1) CTRs.

On the MgO(0 0 1) surface, there are two non-equivalent CTRs: (i) "strong" ones with h and k even, whose intensity is proportional to the square of the sum of the atomic form factors of O and Mg, and (ii) "weak" ones, with h and k odd, whose intensity is proportional to the square of the difference of the form factors. When h and k have a different parity, the CTRs are forbidden by symmetry. Note that, whatever their structure, crystalline or not, it is very unlikely that the droplets contribute to the measured intensity because they almost certainly do not have the same in-plane lattice parameter as MgO, and have a much smaller correlation length. Hence, in the worst case, they yield intensity that appears as background below the rocking scans, and is thus not integrated. However, the substrate below these droplets does indeed contribute to the CTR, with the main effect of a surface roughness introduced by the non-flat interface between the substrate and these droplets. The modifications of the CTRs due to the surface reconstruction arise from the interference between the clean substrate, of structure factor F_{CTR}, and the Ca surface scattering, of structure factor F_{Ca}. This interference is noticeable only when $|F_{CTR}| \leq |F_{Ca}|$. Hence, the "strong" CTRs are mainly sensitive to surface roughness, while the "weak" CTRs are much more sensitive to the presence of Ca. Fig. 7 shows the measured (11l) CTR as a function of the out-of plane reduced coordinate l. The pronounced asymmetry of the (11l) rod around the (1 1 1) Bragg peak is due to scattering by segregated calcium. The (20l) and (11l) CTRs were simultaneously fitted. The fitting procedure was based on the following assumptions: (i) the Ca is in substitutional sites, which is theoretically predicted [19,82–84] and experimentally shown (ii) Ca is present only in the topmost atomic plane, which is also expected from theory and experiments. Only the model represented in Fig. 8, with 50% Ca coverage and a $(\sqrt{2} \times \sqrt{2})$R45°

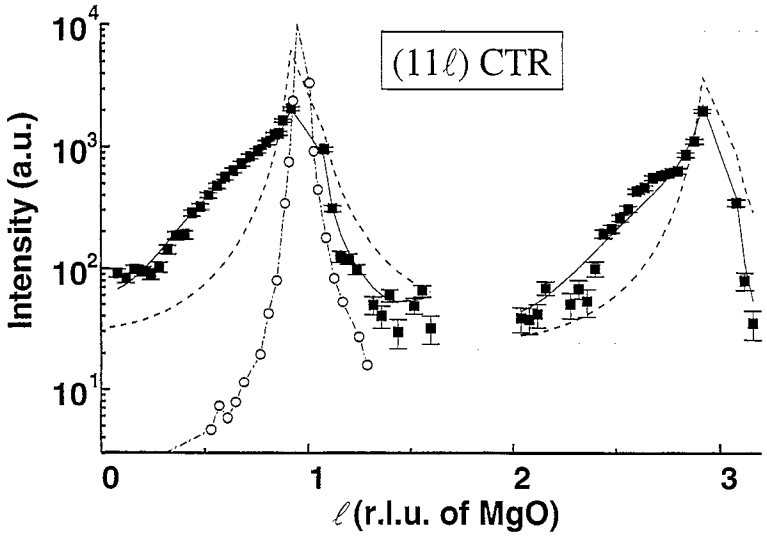

Fig. 7. (11l) Crystal truncation rod measured on a MgO(0 0 1) surface annealed 18 h in air at 1500°C. The logarithm of the intensity is reported as a function of the perpendicular momentum transfer, l, in reciprocal lattice units of the MgO lattice. Squares: experimental data with error bars; continuous line: result of the best fit to the experimental data, corresponding to the model of Fig. 8 and Table 2; dashed line: calculated CTRs for a clean, although rough, MgO(0 0 1) surface. Dashed–dot line with circles: CTR measured on a MgO(0 0 1) surface that has been sputtered with Ar^+ ions at 900°C.

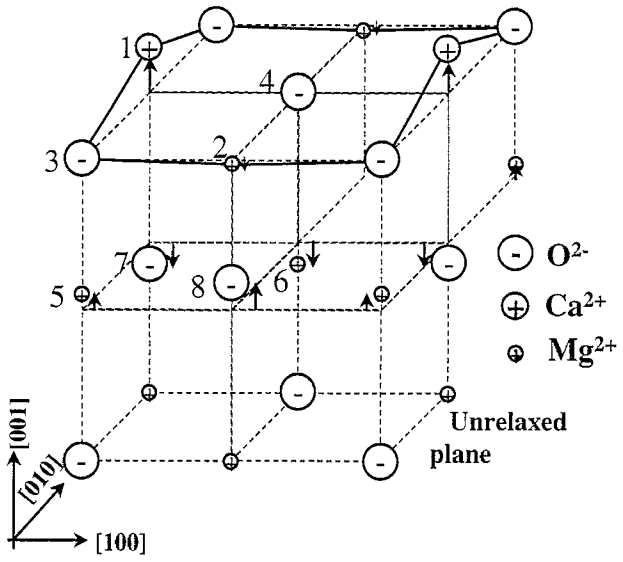

Fig. 8. Schematic representation of the atomic structure of the Ca-segregated MgO(0 0 1) surface. The atoms are labeled, with corresponding displacements reported in Table 2.

reconstruction, yielded an acceptable agreement (see Fig. 7), with $\chi^2 = 1.86$ and 2.1, respectively for the (11*l*) and (20*l*) CTRs. Perpendicular displacements (represented in Fig. 8 and reported in Table 2) were allowed for all atoms of the first two atomic planes, this depth being limited by the maximum number of allowed parameters, given the uncertainty on the data. Neither fractional occupancies, nor incomplete coverage of the surface by the reconstruction had to be introduced: the model corresponds to an exact 50% substitution of Mg sites by Ca ions. Identical scaling factors and rms roughness values (of 2.4 Å) were found for both CTRs, which strongly supports this model.

All in-plane nearest-neighbors and next-nearest-neighbor distances were found to lie within ±10% of the MgO bulk values. Perpendicular distances were found to lie within 20% of the MgO bulk values, excepted for the Ca–O vertical distance (between atoms 1 and 7 of Fig. 8), which is 50% larger than the Mg–O distance, and 25% larger than the Ca–O distance in bulk CaO. This value should be taken with caution since the vertical negative displacement of the underlying oxygen (atom 7) could have been over-estimated, because only relaxation in the first two planes were allowed in the fitting procedure, while it is likely that noticeable displacements propagate deeper into the bulk. An indication of the deeper extension of the reconstruction is the imperfect fit of the oscillation of the (11*l*) CTR at high *l*. The top Ca ions were found to protrude outward from the original MgO plane by 0.63 ± 0.03 Å, which is only slightly larger than the value reported from low energy ion scattering of a Neutral He beam [86] of 0.4 ± 0.1 Å. The signs of the displacement found are in qualitative agreement with those predicted by Masri et al. [82]: top Mg ions are displaced downward, while the underlying O ions go upward; the displacement of the top O ions was not determined, but the negative displacement of the underlying Mg ions is consistent with the calculated one [82].

4.2.2. Clean surface: roughness, relaxation and rumpling

As already mentioned, annealing at high temperature in air was the first step to obtain a good MgO single crystal surface, in view of GIXS studies of this clean surface and of growing metal/MgO

Table 2
Vertical displacements of the eight atoms of the first two planes of the $(\sqrt{2} \times \sqrt{2})$R45° reconstruction of the Ca-segregated MgO(0 0 1) surface, with calcium ions substituting half of the top magnesium ones

	1 : Ca	2 : Mg	3 : O	4 : O	5 : Mg	6 : Mg	7 : O	8 : O
$\Delta z/d$	0.3 ± 0.014	–	0(fixed)±4	0(fixed)±4	0.095± 0.014	-0.2 ± 0.08	0.2 ± 0.12	0.2 ± 0.06
		0.032 ± 0.066						
Δz (Å)	0.63 ± 0.03	-0.066 ± 0.14	0 ± 9	0 ± 9	0.20 ± 0.03	-0.42 ± 0.18	-0.42 ± 0.32	0.42 ± 0.12

The atoms are numbered as indicated in Fig. 8. First row: values relative to the MgO bulk nearest distance of 2.106 Å; second row: absolute displacements.

interfaces. Since this resulted in the surface segregation of Ca, a procedure was developed in order to remove the Ca surface contamination while keeping the MgO surface as perfect as possible. For this purpose, the surface was etched by Ar^+ bombardment at 1550°C, which is a temperature high enough to allow the surface to reorder faster than it disorders, and to keep its smoothness. After this treatment, oxygen or magnesium vacancies could be expected on the surface. In order to restore the surface stoichiometry, a procedure suggested by several groups [70,75,90] was followed: the sample was annealed for 15 min at 700° in a partial oxygen pressure of 10^{-4} mbar. The surface cleanness was checked using AES, and no remaining impurities were found, to the level of 1% of a monolayer. After this preparation, the samples were never exposed to air, in order to avoid the well-known attack of the surface by water vapor [91].

The GIXS measurements on this clean surface were aimed at the determination of the roughness, the relaxation ρ and the rumpling ε, defined according to: $\rho = 1/2\,(\varepsilon_1 + \varepsilon_2)$ and $\varepsilon = \varepsilon_1 - \varepsilon_2$, where ε_1 and ε_2 are, respectively, the fractional displacements of the surface anions and cations, expressed in

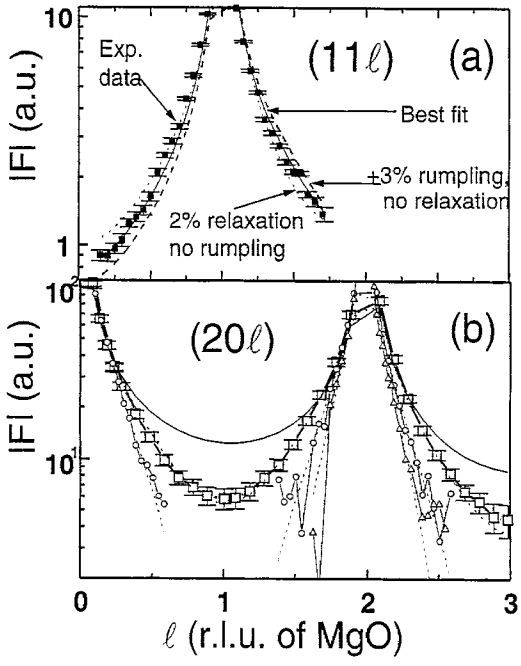

Fig. 9. Modulus of the structure factor of the (11l) (a: top) and (20l) (b: bottom) CTRs of the clean MgO(0 0 1) surface, as a function of the perpendicular momentum transfer l, in reciprocal lattice units of MgO, after 20 min of Ar^+ ion bombardment at 1500°C (squares with error bars). For the (11l) CTR, the continuous line is the best result of a simultaneous fit of the (20l) and (11l) data. Calculated curves without rumpling and with a 2% relaxation (short dashed line) and with 3% rumpling and no relaxation (long dashed line) illustrate the sensitivity of the (11l) CTR to rumpling and relaxation. The measured (20l) CTR is represented for different surface states: after 20 min of Ar^+ ion bombardment at 1500°C (open squares linked with a thick line), after 30 min (open circles) and 2 h (open triangles) of Ar^+ ion bombardment at 900°C. Dotted lines correspond to the best fits, which yield, respectively, rms roughness values of (a) 2.4 Å, (b) 4 Å and (c) 6 Å. The (20l) CTR calculated for a perfectly flat surface is also shown (thin continuous line) for comparison. The rough surfaces are obviously not suitable for a quantitative study.

percentage of the bulk interplanar distance (2.106 Å) perpendicular to the surface. The "strong" (20*l*) CTR was mostly used to determine the rms roughness and the "weak" (11*l*) one to determine the surface relaxation.

On the surfaces prepared as described above, both CTRs, measured by rocking the sample, were everywhere above background, with a very small width ($\sim 0.01°$), always resolution limited, whatever the experimental resolution, which was a confirmation of the high crystalline quality, and a first indication of a small surface roughness. The Lorentzian shape (FWHM 0.01°) at the in plane anti-Bragg location (1 1 0.05) indicates an exponentially decaying height–height correlation function with a terrace length of ~ 6000 Å.

Fig. 9 shows the (20*l*) and (11*l*) CTRs for clean MgO(0 0 1). Fig. 9(a) illustrates the sensitivity of the (11*l*) CTR to rumpling and relaxation, which is obtained only if the roughness is small enough, and when the CTR is measured over an extended range. Both CTRs were simultaneously fitted with four parameters: an overall scale factor, the relaxation and rumpling in the top plane, as well as the rms roughness. The data could not be fitted by restricting the step heights to multiple values of the MgO lattice parameter, i.e. to an even number of atomic planes, which introduces a clear maximum in between Bragg peaks. All step height possibilities had to be introduced, which indicates that most steps are presumably only one atomic plane high, i.e. 2.1 Å. The Debye–Waller factor was fixed at its bulk value of 0.3 $Å^2$ [92] for all ions. The normalized chi-squared agreement factor of 1.1 ± 0.1 was very close to the ideal value of 1, which shows that no new parameter, such as atomic relaxations of deeper atoms, could be added.

All substrates prepared according to our new procedure yielded the same roughness value of 2.4 ± 0.1 Å, which is also the value determined on the Ca-segregated surfaces. One could suggest that further decrease of the roughness would be achieved by stopping the ion sputtering before starting to lower the annealing temperature. This is not obvious because the time for annealing without bombardment is limited by the inevitable new segregation of impurities from the bulk.

Because the relaxation and rumpling are both very small, slightly different values were found on the different substrates. The average values of $\rho = (-0.56 \pm 0.35)\%$, and $\varepsilon = (1.07 \pm 0.5)\%$ are thus given, with the error bar estimated from the uncertainties of each fit, and from the different values obtained.

In the original paper [56], these values are compared to previous experimental and theoretical determinations. Thanks to the high substrate quality and the extended measurement range, the error bars are significantly smaller in the present study. Many early shell model calculations and several experiments (RHEED [93], He diffraction [76] or SEELFS [75]) yielded much too large rumpling values. In most cases, this can be attributed to an inadequate substrate preparation, i.e. exposure to air before introduction in the UHV chamber. Most other theoretical or experimental results are close to the present ones, especially the latest one by medium energy ion scattering [78], which yields similar values of the relaxation and rumpling with larger error bars. The precise values reported in the present work might help further refinement of the theoretical calculations.

In summary, a new procedure has been developed to prepare MgO(0 0 1) surfaces of very high quality. These surfaces are ideally suited to perform GIXS measurements. This offers the opportunity to investigate the atomic structure and morphology of metal/MgO interfaces by this technique, during in situ deposition in UHV by molecular beam epitaxy, from the very early stages of sub-monolayer deposition, up to fairly thick metallic layers. Such measurements will be presented in Section 5.

4.3. α-Al_2O_3(0 0 0 1) surface

4.3.1. Termination and relaxation of the unreconstructed surface [39,94,95]

The (0 0 0 1) surface of sapphire (α-alumina, corundum) is one of the most widely used substrate for the growth of metal, semiconductor or high-temperature superconductor thin films. It is also used as a substrate in silicon on sapphire (SOS) technology. Moreover, its initial state is known to play a role on the overlayer properties [96]. Despite many theoretical calculations of the α-Al_2O_3(0 0 0 1) surface structure and relaxation [19,97–101], the nature (Al or O) of the terminating plane of the unreconstructed surface was still an open topic because of the lack of experimental results. The single Al terminated surface is favored by electrostatic considerations [19] as well as surface energy calculations [97]. Indeed, for an Al termination no dipole moment is left across the surface and only the longer, and thus the weaker, anion–cation bonds are broken. However, the (1 × 1) structure is also experimentally observed on alumina surfaces heated in an oxygen-rich atmosphere and could thus be suspected to be oxygen terminated. As regards the Al-terminated surface, large relaxations have been predicted by pair-potential calculations [98]. More recently, ab initio calculations, by the density functional theory combined with pseudopotential techniques [99] predicted very large relaxation of the last atomic plane (−87%), while Hartree–Fock calculations [100] yielded smaller, although still sizable, relaxation (−40%). A tight binding, total-energy method [101] also predicted large out-of-plane relaxations of the Al planes and in-plane displacements of the oxygen atoms.

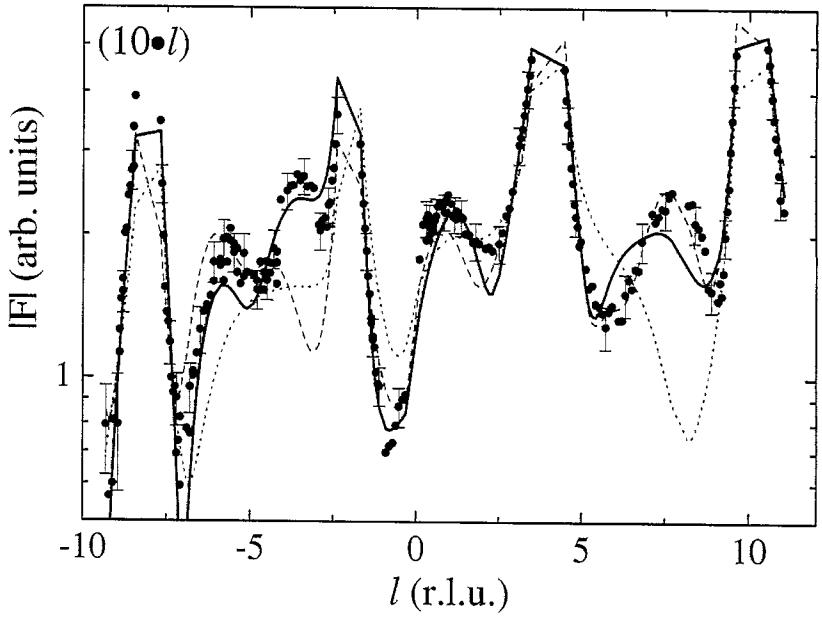

Fig. 10. (10l) CTR of the α-Al_2O_3(0 0 0 1)-(1 × 1) surface. Experimental (solid circles) and best-fit models for each possible termination: single Al layer (thick solid line), double Al layer (dashed line) and oxygen terminated surfaces (dotted line). The logarithm of the structure factor is reported as a function of the out-of-plane momentum transfer in reciprocal lattice units of Al_2O_3.

The aim of the GIXS study was to determine experimentally, for the first time, the nature of the terminating plane and the relaxations of the first few atomic planes below the surface by quantitative measurement and analysis of the CTRs. The experiments were performed on a first sample using the LURE W21 beamline and diffractometer [53], and on a second sample using the ESRF ID3 surface diffraction setup [52]. Both samples were first annealed in air for three hours at 1500°C, resulting in a surface with wide, atomically flat terraces, and a good near-surface crystalline quality. Both data sets yielded exactly the same conclusions. During the second, more precise experiment, eight CTRs were measured over an extended range of perpendicular momentum transfer from 0 up to 7.2 $Å^{-1}$, and corresponding to 873 non-equivalent reflections. The (10l) CTR is reported in Fig. 10.

Bulk sapphire has rhombohedral symmetry, which is usually treated as hexagonal (space group $R\bar{3}c$), with 30 atoms (six Al_2O_3 units) per primitive unit cell. The lattice parameters ($a = b = 4.7570$ Å, $c = 12.9877$ Å) and the internal coordinates ($x = 0.3063$, $z = 0.3522$) are taken from Ref. [102]. The bulk unit cell consists of an alternated stacking, along the c-axis, of two Al^{3+} planes (12 in the unit cell) with one atom per plane, and one oxygen plane (six in the unit cell) with three O^{2-} ions arranged with a threefold symmetry. From a crystallographic point of view, no two planes among the 18 of the unit cell are equivalent, under any translation. For each possible chemical termination (oxygen, single Al or double Al) there are thus six crystallographically non-equivalent terminations. Fortunately, only two of these yield non-equivalent diffraction patterns. The (1 × 1) surface has p3 symmetry with the threefold axis lying on the Al atoms. Hence, only their coordinate along the c-axis can vary, whereas oxygen can also move parallel to the surface plane as long as they keep the threefold symmetry around the Al sites. Because of this symmetry, they must also remain coplanar. The surface model included displacements of three Al_2O_3 units plus those of the terminating planes (15, 16 or 17 parameters depending on the termination). Because of the extremely high sensitivity of CTRs to atomic positions, deeper atomic displacements can enhance fit quality even with very small values but they are not significant for the structure. Al^{3+} and O^{2-} atomic scattering factors were used for all atoms although theoretical arguments [100] as well as an experimental Auger electron spectroscopy study [103] suggests that surface atoms may have a different charge. This should be of little importance especially at large momentum transfer. Debye–Waller parameters were taken to be isotropic and set to the bulk values [102] for all atoms.

Least square fitting and visual inspection (Fig. 10) clearly allowed ruling out the oxygen and double Al terminations. The surface is thus terminated with a single Al layer, which yielded $\chi^2 = 0.92$. Fitted atomic positions are listed in Table 3 and the surface structure is schematically shown in Fig. 11. The top two planes undergo large displacements from their bulk positions (0.34 Å and 0.23 Å, respectively). The top Al layer moves down towards the bulk so that the interplanar spacing with the nearest neighbor oxygen layer is reduced by 51%. The underlying oxygen atoms shift mainly parallel to the surface plane and are repelled from the first layer Al sites, moving almost radially towards the second layer. This is an almost bond length conservative motion: the bond length is only 4.5% (±2.5%) shorter than the bulk nearest neighbor value. Displacements below the first two planes are smaller: relaxations are +16%, −29% and +20% for the next three interplanar spacing.

These results were compared with theoretical calculations. The single Al termination was always the predicted one, because it is the only termination that is "auto-compensated" (both charge neutral and chemically stable) and with no electric dipole moment across the surface. Regarding the surface relaxations, all theoretical studies agreed with the large negative relaxation of the top Al layer. Godin et al. [101] suggested a rehybridization of the top Al atoms from the four-fold coordinated arrangement

Table 3
Atomic positions of atoms in the hexagonal α-Al_2O_3(0 0 0 1) unit ($z > 0$ towards vacuum), for the truncated bulk and for the relaxed surfaces, and absolute displacements between the two

	Truncated bulk			Relaxed surface			Displacement (Å) (±0.05 Å)
	x	y	z	x	y	z	
Al	0.000	0.000	1.148	0.000	0.000	1.122	0.34
O	0.361	0.333	1.083	0.352	0.372	1.090	0.23
O	0.667	0.027	1.083	0.628	−0.021	1.090	0.23
O	0.973	0.639	1.083	1.021	0.648	1.090	0.23
Al	0.333	0.667	1.019	0.333	0.667	1.015	0.05
Al	0.667	0.333	0.981	0.667	0.333	0.988	0.09
O	0.639	0.667	0.917	0.633	0.670	0.911	0.09
O	0.333	0.973	0.917	0.330	0.963	0.911	0.09
O	0.027	0.361	0.917	0.037	0.367	0.911	0.09
Al	0.000	0.000	0.852	0.000	0.000	0.849	0.04
Al	0.333	0.667	0.815	0.333	0.667	0.812	0.03
O	0.694	0.000	0.750	0.692	0.008	0.748	0.05
O	0.000	0.694	0.750	−0.008	0.684	0.748	0.05
O	0.306	0.306	0.750	0.316	0.308	0.748	0.05
Al	0.667	0.333	0.685	0.667	0.333	0.685	0.01
Al	0.000	0.000	0.648	0.000	0.000	0.647	0.01

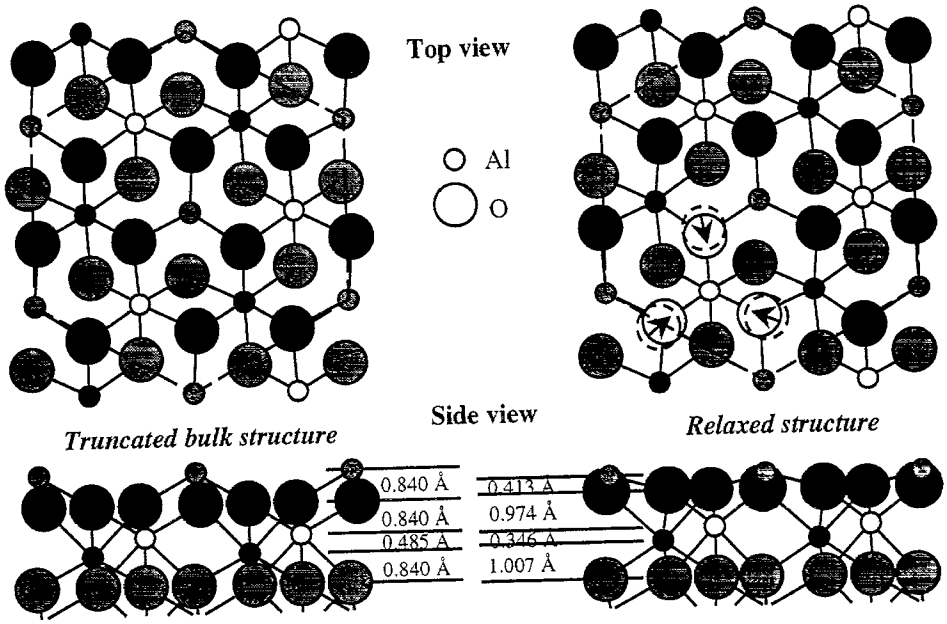

Fig. 11. Illustration of the sapphire (0 0 0 1) surface: truncated bulk and best-fit model obtained from CTRs measurements. The two top planes are strongly shifted with respect to their bulk positions in a nearly bond length conservative displacement.

(which may be thought as a sp^3 configuration) to a nearly perfect sp^2 configuration. More generally, all authors agree on the stronger bonding between Al and oxygen atoms nearby the surface, which is the general trend of the GIXS results, bond lengths being shortened by 4.5–6.1% in the first four planes. The results are also in very good agreement with very recent theoretical [104], and experimental [105] results.

To the author's knowledge, this was the first experimental determination of the relaxations of an oxide surface by GIXS, and the first experimental determination of the relaxation and termination of the α-$Al_2O_3(0\,0\,0\,1)$ surface. Another determination has been performed very recently by combining time-of-flight scattering and recoiling spectrometry with LEED and classical ion trajectory simulations [105] with essentially the same results.

4.3.2. Projected atomic structure of the α-$Al_2O_3(0\,0\,0\,1)(\sqrt{31} \times \sqrt{31})R \pm 9°$ reconstruction [106]

When the α-$Al_2O_3(0\,0\,0\,1)$ surface is heated at high temperature in UHV, several reconstructions appear: $(\sqrt{3} \times \sqrt{3})R30°$ around 1100°C; $(\sqrt{3} \times \sqrt{3})R30°$ around 1150°C; $(3\sqrt{3} \times 3\sqrt{3})R30°$ around 1250°C; and finally $(\sqrt{32} \times \sqrt{31})R \pm 9°$ around 1350°C. Although their electronic structure and symmetry were well characterized [107–109], their atomic structure remained essentially unknown. The $(\sqrt{31} \times \sqrt{31})R \pm 9°$ reconstruction is of particular interest because it has been reported to help epitaxy and enhance adhesion in some cases [110] and because it is unusually stable, even after air exposure. A structural model for this reconstruction had been proposed three decades ago [107]. The LEED pattern was interpreted as the superposition of two reciprocal lattices: that of the hexagonal substrate and that of a nearly cubic overlayer with composition Al_2O or AlO, plus the interference pattern because of double diffraction. However, this model remained controversial. In particular, this interpretation did not include a supercell formation with atomic relaxations. The aim of the GIXS study was to analyze the α-$Al_2O_3(0\,0\,0\,1)(\sqrt{31} \times \sqrt{31})R \pm 9°$ reconstruction in order to get unambiguous answers concerning the presence of a supercell, and ultimately to determine its atomic structure. Clearly, in the case of a reconstruction or of a thin layer, multiple scattering of X-rays is completely negligible. Hence, the GIXS pattern can be fully interpreted using the kinematic theory of diffraction, where only the single scattering events are taken into account.

The α-$Al_2O_3(0\,0\,0\,1)$ single crystals were first annealed in air at 1500°C for three hours, and next heated to $\sim$ 1350°C for $\sim$ 20 min in UHV to obtain the $(\sqrt{31} \times \sqrt{31})R \pm 9°$ reconstruction. Measurements were performed using the LURE W21 beamline and diffractometer [53]. A large number, 366 of which 267 were non-equivalent, of in-plane reflections arising from the reconstruction were measured. All peaks were exactly centered at the expected positions to within 0.001° of azimuthal rotation, which showed that the surface reconstruction is perfectly commensurate with the underlying bulk lattice. Their width and Lorentzian shape indicated an exponential decay in correlations with the decay length of $\sim$ 500 Å. Several reconstruction diffraction rods were also measured. The absence of symmetry of the rod intensity with respect to $l = 0$ showed that the reconstruction has the minimal hexagonal symmetry p3.

The experimental diffraction pattern (Fig. 12) has sixfold symmetry. Measurable intensity was found at all reciprocal lattice points of the reconstructed unit cell, even far away from bulk Bragg peaks. Because X-ray scattering by surfaces is by essence kinematical, this result contradicts previous interpretations of the LEED pattern [107] in terms of multiple electron scattering due to the coincidence of lattice sites between a rearranged surface layer with a small unit cell and the hexagonal substrate. In that case, X-ray diffraction peaks other than bulk would be found only at the reciprocal lattice points of

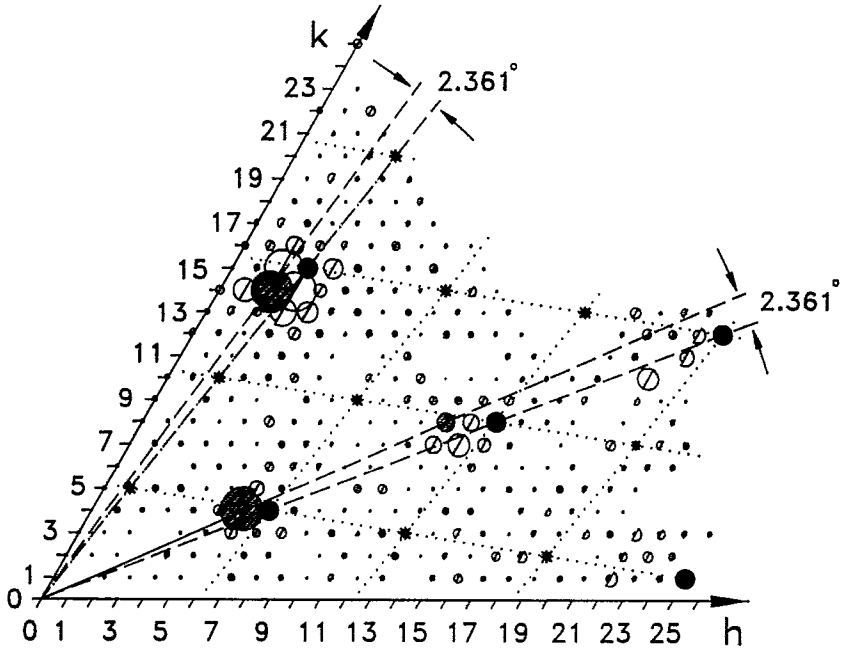

Fig. 12. Experimental diffraction pattern, indexed in the reciprocal space of the reconstructed unit cell (in 1/6 of the $l = 0.12$ reciprocal plane). The radii of the right-hand halves of the open circles are proportional to the experimental structure factors, while the left-hand open circles are calculated from the best model ($\chi^2 = 1.2$). Black disks represent bulk allowed and CTR reflections. The bulk unit mesh is superposed as dotted lines. The three main diffraction peaks of the reconstruction, corresponding to the "parent" phase, are hatched.

the surface and bulk unit cells. The X-ray diffraction intensity distribution proved that there indeed is a genuine $(\sqrt{31} \times \sqrt{31})\mathrm{R} \pm 9°$ supercell formation with atomic relaxations.

The diffraction pattern was shown to be qualitatively very similar to that predicted [111,112] in the case of rotational epitaxy of an hexagonal overlayer, which is expanded and rotated with respect to an ideal overlayer R in perfect registry. The main peaks (hatched in Fig. 12) correspond to the first-order approximation, called "parent" phase, of the adsorbed structure. Their locations yield the expansion, 10.62%, and rotation, 2.361°, applied to the R phase to obtain this rigid hexagonal "parent" phase. The other diffraction peaks are satellites corresponding to the static distortions of this parent phase, and possibly to additional disorder.

Fig. 13 shows the experimental pair-correlation (Patterson) function. Most Patterson peaks have a nearly perfect hexagonal arrangement. The positions of these peaks can be directly constructed by a rotation of $\sim 1.4°$ followed by a small expansion of the projected atomic positions of an FCC(1 1 1) stacking on top of the oxygen HCP(0 0 0 1) stacking of the underlying bulk lattice. Many possible models were tested before the final one was proposed. The reconstructed structure, schematically shown in Fig. 14, was interpreted as a tiling of domains bearing a close resemblance to that of two metal Al(1 1 1) planes, separated by a hexagonal network of domain walls. In the middle of domains, the overlayers are well ordered, with a lattice parameter very close to that of metallic Al (expansion of

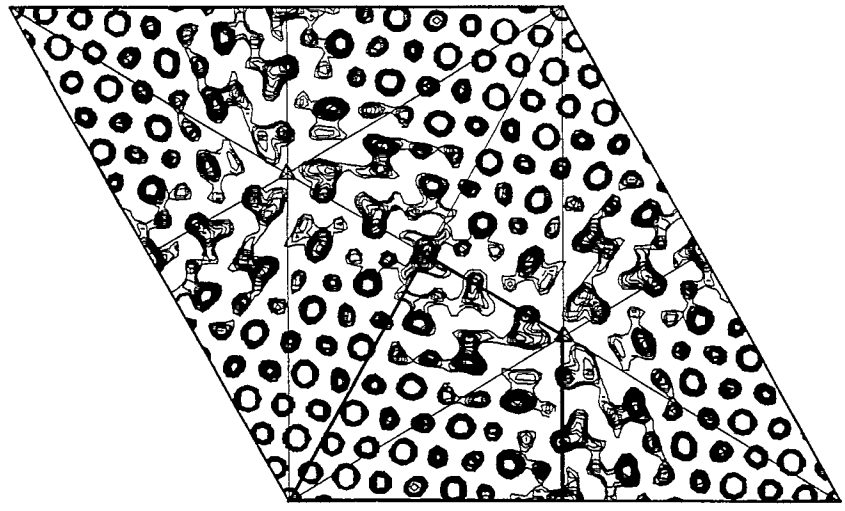

Fig. 13. Experimental Patterson map of the α-$Al_2O_3(0\,0\,0\,1)$-$(\sqrt{31} \times \sqrt{31})R \pm 9°$ reconstruction in the whole reconstructed unit cell. Lines are only guides to locate the three-fold axes and the centered two-fold axis of the Patterson p6 symmetry. Bold lines delimit the asymmetric unit cell of the Patterson map.

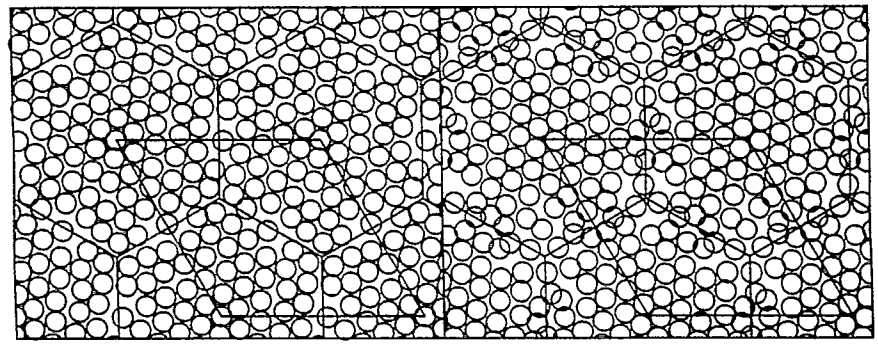

Fig. 14. Several domains of the projected atomic structure of the α-$Al_2O_3(0\,0\,0\,1)$-$(\sqrt{31} \times (\sqrt{31})R \pm 9°$ reconstruction, where the unit cells as well as domain walls are drawn. The two constituting Al planes are shown separately, with evidence of one being much better ordered than the other. Numerical relaxation has shown that the ordered layer could be associated to the second layer, and the more disordered one to the layer adjacent to the substrate.

4% with respect to the registered state), and a small rotation ($\sim 1.46°$ with respect to the R state) with the epitaxial relationships: $(1\,1\,1)Al//(0\,0\,0\,1)Al_2O_3$ and $[\bar{1}\,1\,0]Al//(R1.4°)[1\,1\,\bar{2}\,0]Al_2O_3$. In the domain walls, large expansion and rotation, and even loss of honeycomb network topology were found. The observed structure was interpreted in the spirit of rotational epitaxy with nonlinear distortions.

The study described in Section 4.3.1 showed that the unreconstructed α-$Al_2O_3(0\,0\,0\,1)$ surface is terminated by an Al layer with 1/3 compact packing. Hence, starting from this surface, removing the two last O planes would leave 5 Al layers with 1/3 compact packing occupancy at the surface, which is the observed 5/3 filling ratio. It was then suggested that the reconstruction is obtained after evaporation of the two upper oxygen layers of the unreconstructed surface. The physical origin of the $\sim 4\%$ expansion in the domains is clear, since the overlayer is very close to bulk Al and registry. A minimum-energy numerical simulation of the two Al planes, interacting with each other and with the substrate via a Lennard-Jones potential was performed. The observed atomic structure was shown to be consistent with previous studies of the $(\sqrt{31} \times \sqrt{31})R \pm 9°$ reconstruction [107–113], which yielded an Al enrichment, intermediate oxidation states of surface aluminum atoms and a reduced surface band gap. It is also consistent with the observation [107,114] of a $(\sqrt{31} \times \sqrt{31})R \pm 9°$ reconstruction during the first stage of Al deposition (between 0.4 and 2.5 Al(1 1 1) ML coverage) on an α-$Al_2O_3(0\,0\,0\,1)$ surface with (1×1) structure, followed by Al(1 1 1) domain growth for larger coverage. Thus, a fundamental question was opened concerning the process and dynamics of this reconstruction formation by different routes: reduction or Al deposition. This motivated a structural study of the intermediate reconstructions briefly reported in the next paragraph.

4.3.3. GIXS studies of the $(2\sqrt{3} \times 2\sqrt{3})R30°$ and $(3\sqrt{3} \times 3\sqrt{3})R30°$ reconstruction [115]

The $(2\sqrt{3} \times 2\sqrt{3})R30°$ and $(3\sqrt{3} \times 3\sqrt{3})R30°$ reconstructions were recently investigated by GIXS at the ESRF, on the ID3 and BM32 beamlines, under experimental conditions very similar to those of the $(\sqrt{31} \times \sqrt{31})R \pm 9°$ study. Both reconstructions can be prepared in a very well defined state, with large domain sizes, and very similar data were obtained in both cases. Fig. 15, which shows an in-plane

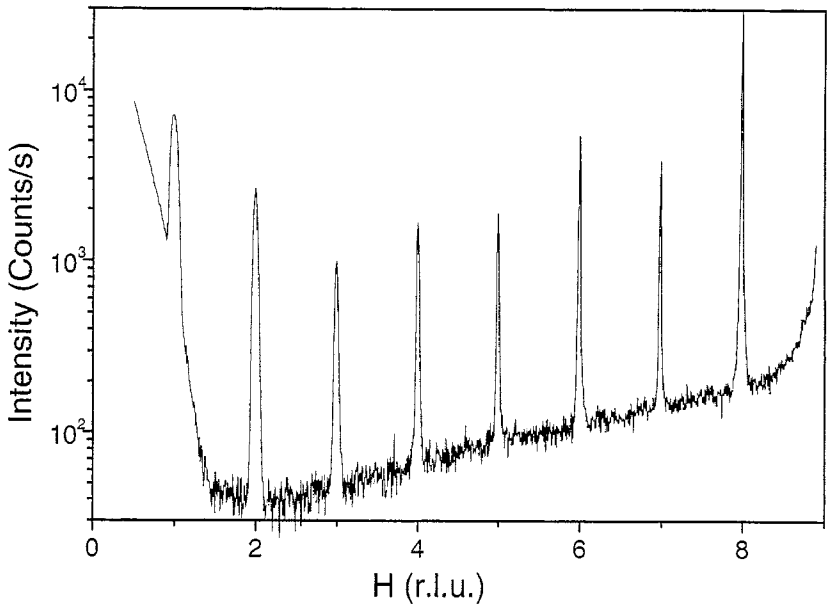

Fig. 15. In-plane radial scan along the (1 0 0) direction of the α-$Al_2O_3(0\bar{0}\,0\,1)$-$(3\sqrt{3} \times 3\sqrt{3})R30°$ reconstruction. h is in reciprocal lattice units of the $3\sqrt{3}$ unit cell. Note the very intense and narrow reconstruction peaks indicating very large domain sizes of several microns.

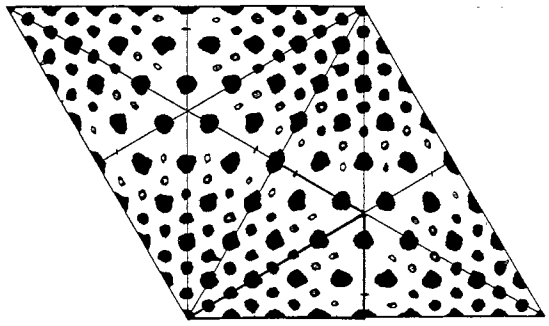

Fig. 16. Experimental Patterson map of the α-$Al_2O_3(0\,0\,0\,1)$-$(3\sqrt{3} \times 3\sqrt{3})R30°$ reconstruction in the whole reconstructed unit cell. Bold lines delimit the asymmetric unit cell of the Patterson map.

radial scan along the $(h\ 0\ 0)$ direction for the $(3\sqrt{3} \times 3\sqrt{3})R30°$ reconstruction, illustrates this high structural quality. The experimental Patterson map of the $(3\sqrt{3} \times 3\sqrt{3})R30°$ reconstruction is shown in Fig. 16. Out-of plane rod measurements showed that, as in the $(\sqrt{31} \times \sqrt{31})R \pm 9°$ case, the thickness of the reconstruction is limited to one or two atomic planes. Although the analysis has not yet been performed, a qualitative comparison with the diffraction pattern and Patterson map of the $(\sqrt{31} \times \sqrt{31})$ $R \pm 9°$ reconstruction shows that the structures are likely to have the same origin, excepted that no rotation is involved in the case of the $(3\sqrt{3} \times 3\sqrt{3})R30°$ reconstruction. More precisely, the structure of the $(3\sqrt{3} \times 3\sqrt{3})R30°$ reconstruction is likely to consist of an overlayer with hexagonal symmetry, made of one or several planes close to compact planes, and with a lattice parameter slightly larger ($\sim$ 12%) than that of sapphire, such that, along the [1 1 0] directions of sapphire, the two lattices coincide every 9 (1 1 0) d-spacing of sapphire, and 8 (1 1 0) d-spacing of the overlayer, yielding the $(3\sqrt{3} \times 3\sqrt{3})R30°$ superlattice unit cell of $\sim$ 25 Å periodicity. Such a rigid overlayer would yield only the strongest peaks of the diffraction pattern. All the other weaker peaks would correspond to harmonics in Fourier decomposition, arising from small displacements of the atomic positions with respect to the average "parent" rigid lattice. A quantitative analysis with modeling of the compact overlayer is required to get a more detailed picture of the structure.

4.4. *TiO_2 surfaces*

The surfaces of rutile TiO_2 have been the subject of intense research because of their photo-catalytic properties for the dissociation of water. The hydroxylation rate on the surface and the kinetics of the reaction were shown to depend strongly on the surface stoichiometry and detailed atomic structure. In addition, like the two above surfaces of sapphire and magnesium oxide, rutile titanium dioxide surfaces stand as model metal oxide surfaces. Their atomic structure is thus of fundamental interest.

4.4.1. *TiO_2(1 1 0) relaxation [116]*

The structure of the TiO_2(1 1 0) surface, depicted in Fig. 17, has been thoroughly studied recently [1,117–119]. This is the most stable surface of rutile TiO_2: only after extensive heating (14 h) at elevated temperatures (900 K) this surface reconstructs to form a (1×2) surface. A recent GIXS study of the CTRs allowed, as in the case of the α-$Al_2O_3(0\,0\,0\,1)$-(1×1) surface, the determination of the structural relaxations of the unreconstructed surface.

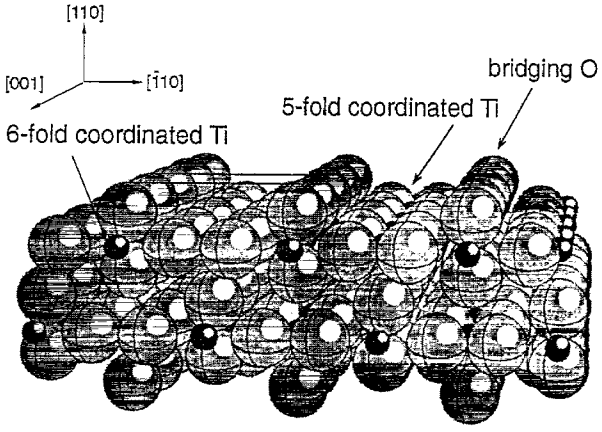

Fig. 17. Space-filling model of bulk terminated $TiO_2(1\,1\,0)$-(1×1). The 1×1 surface unit cell, which has dimensions $6.5\,\text{Å} \times 2.96\,\text{Å}$, is highlighted. Small spheres represent Ti and large spheres represent O. The spheres are scaled to the corresponding ionic radii (reprinted from [116]).

The surface was prepared in situ by repeated cycles of Ar^+ sputtering and annealing at 1100 K. This was followed by an anneal at 900 K and cooling to 550 K in 1×10^6 mbar O_2 to restore the surface stoichiometry. No surface contamination could by detected by AES. The unit cell has lattice vectors $\boldsymbol{a}_1$ and $\boldsymbol{a}_2$ in the plane of the (1 1 0) surface (along the $[\bar{1}\,1\,0]$ and $[0\,0\,1]$ directions, respectively), and $\boldsymbol{a}_3$ is perpendicular to it. Values of $a_1 = a_3 = 6.495\,\text{Å}$ and $a_2 = 2.958\,\text{Å}$ were used. Five CTRs, shown in Fig. 18, were measured from 0 up to $4.8\,\text{Å}^{-1}$. They were fitted using 23 fitting parameters including 13 atomic displacements. The final χ^2 value was 3.8, which is quite large, compared to the ideal value of 1. This could indicate either that a more accurate model could be found, or that the experimental data have additional uncertainties, with respect to the one assigned to the measured structure factors. The displacements are schematically shown in Fig. 19, and the values deduced from the best fit are reported in Table 4. The magnitude range from 0 to 0.27 Å. The main relaxations involve the top layer sixfold coordinated Ti atoms moving out of the surface and the top layer fivefold coordinated Ti atoms moving towards the surface. This creates a rumpling of 0.3 ± 0.1 Å of the top layer, with a period 6.5 Å, the unit cell length along the $[\bar{1}\,1\,0]$ direction. This rumpling is repeated in the next plane of titanium atoms, with an amplitude about half of that in the top Ti plane. The relaxation induced modification to the bond length range from 11.7% contraction to 9.3% expansion. The relaxations deduced from a recent detailed theoretical calculation [120] are reported in Table 4 for comparison. There is good agreement with experimental data in the Ti atom positions, with some significant discrepancy for the relaxation of O atoms. Worse agreement was obtained with other two recent calculations [121,122].

4.4.2. *$TiO_2(1\,0\,0)$-(1×3) reconstruction [123,124]*

Contrary to the (1 1 0) face, the clean (1 0 0) rutile surface is unstable, and facets upon annealing to form (1 1 0) and other low index faces [125,126]. Annealing in UHV the sputter-cleaned (1 0 0) surface at 873 K results in the formation of a (1×3) reconstruction. This reconstruction is particularly interesting because of the photo-catalytic properties of rutile that are believed to be related to a certain defect density on the surface. The atomic structure of this reconstruction has been first studied by a combined GIXS and LEED study in 1992 [123], which provided the basis of a structural model, with

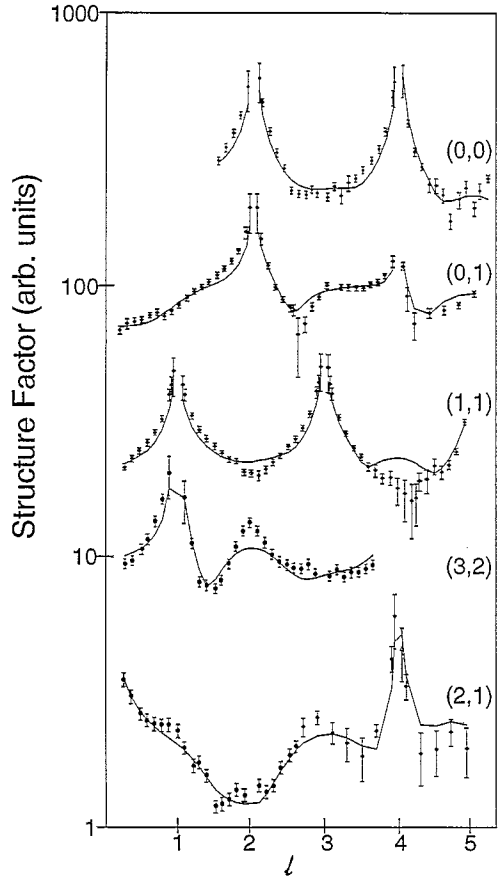

Fig. 18. The five CTRs measured on a log10 scale, together with the result of the best fit. The curves have been shifted perpendicularly for clarity (reprinted from [116]).

formation of {1 1 0} micro facets. The micro-facets model can be explained by the fact that the most stable surface is formed by breaking the minimum number of cation–anion bonds. Recent photoelectron diffraction (PED) [127] and STM [117,128,129] studies have confirmed the micro-facets model, but contradicted the original conclusion that the surface is terminated by an oxygen layer. The large uncertainty on these first measurements could have led to a misleading interpretation. A new detailed GIXS investigation [124] has thus been performed recently to reexamine this reconstruction.

In the first study, both the GIXS and LEED experiments were performed with a portable UHV chamber equipped with a cylindrical Be window, and mounted to a four-circle diffractometer. Because of the restricted geometry of the baby chamber, only a small portion of the reciprocal space was accessible. A total of 19 in-plane surface diffraction peaks were recorded, and a Patterson map was used to propose a model consisting primarily of (1 1 0) planes. Because Ti is a much stronger scatterer than O, the Patterson function is dominated by Ti–Ti pairs. Since the experimental uncertainty was fairly large, and a significant background was present compared to the surface scattering, no attempt was made to locate O atoms from the Patterson map; a composite electron density map was rather used,

Table 4
The atomic displacements from the bulk terminated structure of $TiO_2(1\,1\,0)$-(1×1) derived from GIXS data.

Atom type	Displacement (Å)
Ti(1)	0.12 ± 0.05
Ti(2)	-0.16 ± 0.05
Ti(3)	-0.09 ± 0.04
Ti(4)	0.07 ± 0.04
O(1)	-0.27 ± 0.08
O(2)	-0.16 ± 0.08
O(3)	0.05 ± 0.08
O(4)	0.00 ± 0.08
O(5)	0.02 ± 0.06
O(5)	-0.07 ± 0.06
O(6)	-0.09 ± 0.08
O(7)	-0.12 ± 0.07

Fig. 19 shows the spatial distribution of the atom types, with the symmetry-paired atoms denoted as 2′ and 5′. Of the 13 atomic displacement parameters, 11 are for movement in and out of the surface in the [110] direction. Only two atom types in the unit cell are allowed to move in plane parallel to $[\bar{1}\,1\,0]$; these are the in-plane O atoms in the top (O(2)) and second (O(5)) layers. Each of these O atom types can be considered as existing in pairs. They are constrained to move by an equal distance either towards or away from one another in order to conserve the symmetry of the (1×1) unit cell. A $*$ indicates that the atom position was frozen.

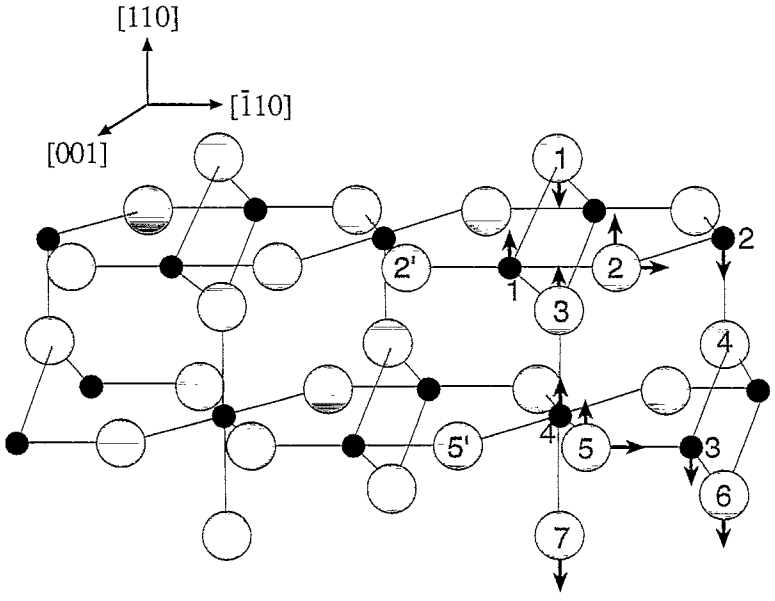

Fig. 19. Real space model of bulk-terminated $TiO_2(1\,1\,0)$-(1×1). Small black circles represent Ti and large gray circles O. The arrows indicate the direction of the relaxations determined. The atom types varied in the structural refinement are shown. Only the in-plane oxygen atoms were allowed to move laterally in the fit. On symmetry grounds the reminder of the atoms were constrained to move perpendicular to the surface (reprinted from [116]).

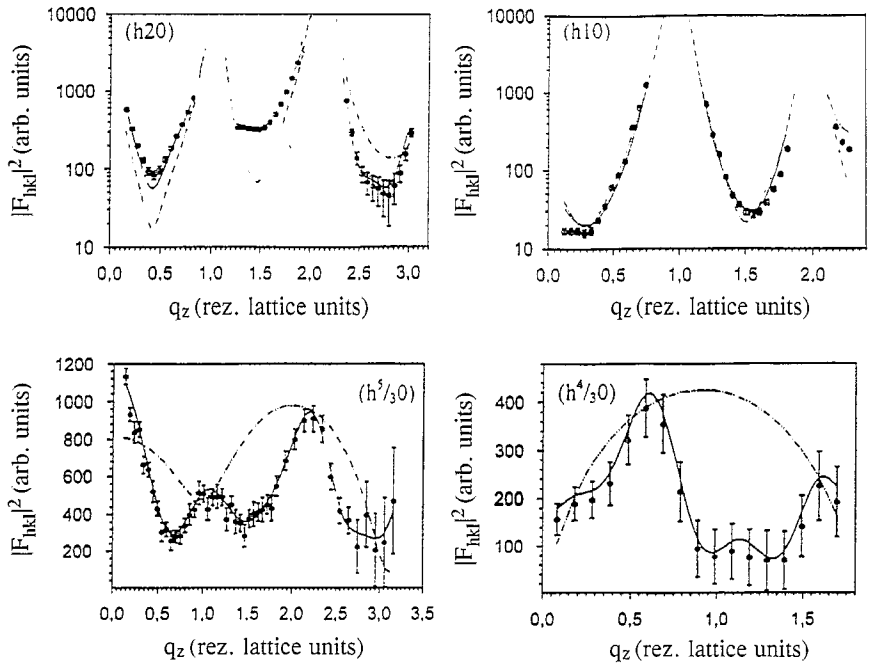

Fig. 20. Intensity of the experimental data (black disks) and for the structure model for the $TiO_2(1\,0\,0)$-(1×3) reconstruction (continuous line), plotted against the momentum transfer normal to the surface. The two top curves are CTRs, and the bottom ones are fractional order rods (reprinted from [124]). The dash–dot line shows the structure factor for an unrelaxed structure.

together with the maximum entropy method. The final in-plane atomic positions were determined by least squares refinement. The determination of the perpendicular atomic positions was done by performing an LEED–I/V experiment including a full dynamical calculation of I–V curve profiles. In the more recent GIXS study, a total of 464 reflections were measured of which 229 were non-equivalent: 22 in plane, 131 fractional order superlattice and 86 CTRs reflections. Fig. 20 shows representative examples of a CTR and a superlattice rod, with the best fit to the data. The rms roughness deduced from the fit is 5.6 Å, which is small enough to allow measurement of the complete CTRs thanks to the large scattering power of Ti. As noted by the authors, and this is a very general remark, the combined use of reconstruction rods and CTRs in the refinement enhances the reliability of the final structure model. Indeed, because both the reconstruction and bulk scattering interfere along the CTRs, the CTRs present a specific phase contrast and are more sensitive to surface relaxations than the reconstruction rods. Fig. 21 shows the Patterson map deduced from in-plane fractional order data, with the corresponding Ti–Ti interatomic distances, and Fig. 22 shows schematically the final structure in a projection along [0 0 1]. Strong lateral and vertical relaxations of the Ti and O atoms in the top layer were found. The coordination numbers of the atoms on the surface facets were found to differ considerably from those derived by Zschack et al. [123]. For instance, the Ti1 atom has a threefold coordination by oxygen on the facet ridges, as opposed to bulk coordination in [123]. In the final model, a surface octahedral interstitial site of the O lattice was found to be occupied by a surface titanium atom, with 40% occupancy per (1×3) cell. Partial occupancies of 60% were also found for the O1 and Ti5 surface atoms. The resulting stoichiometry for this surface structure is $TiO_{1.68}$, which is equivalent to a

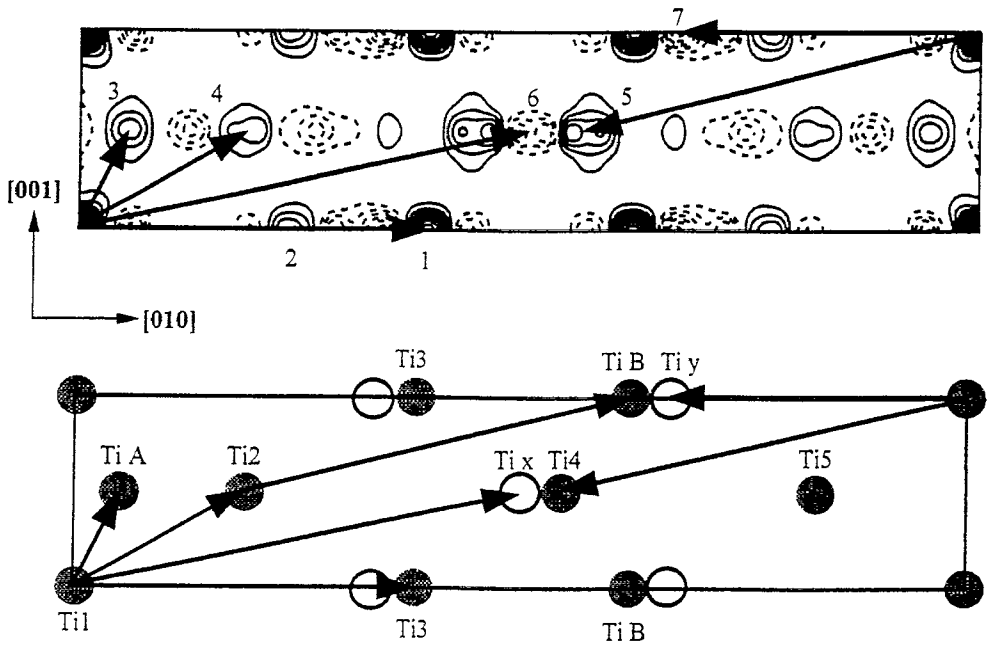

Fig. 21. Patterson map of the in-plane data for the $TiO_2(1\,0\,0)$-(1×3) reconstruction. The arrows indicate the interatomic vectors of the Ti positions in the developed structure model (reprinted from [124]).

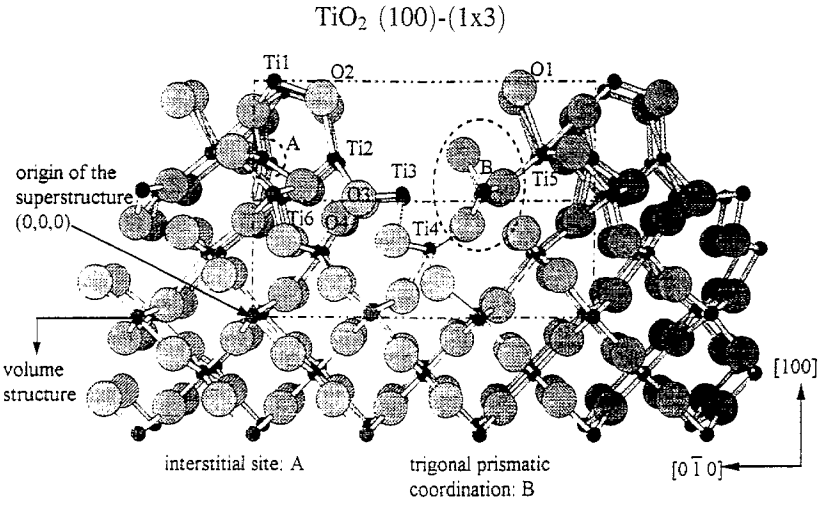

Fig. 22. Final structure model of the rutile $(1\,0\,0)$-(1×3) surface projected along [0 0 1]. An arrow indicates the origin of the superstructure cell. The titanium atoms labeled Ti1–Ti5 and A, B are coordinated by oxygen as follows: Ti1 threefold; Ti2 fivefold; Ti3 bridge site; Ti4 sixfold; Ti5 sixfold; A fivefold (interstitial site) and B sixfold (trigonal prismatic) (reprinted from [124]).

15.5% oxygen deficiency on the surface relative to the bulk. Hence, the refined model can be described as the formation of strongly distorted {1 1 0} micro facets on the surface with oxygen defects and a partial occupancy of an interstitial site. Relaxations are found down to 9 Å below the topmost layer. The different coordinations found for Ti might explain part of the photo-catalytic properties of this surface.

4.5. *NiO(1 1 1) atomic structure [130]*

The NiO(1 1 1) surface has many physical properties that make it attractive for applications, especially as a substrate for future magnetic sensors based on the spin-valves geometry. NiO is a ferromagnetic material with the pure spins planes parallel to the (1 1 1) planes and it is highly resistant to corrosion. In addition, interfacial magnetic ordering effects and enhanced reactivity on NiO based films were recently observed [131–133]. According to the classification of Tasker [19], the ideally truncated NiO(1 1 1) surface is a polar surface and is thus unstable. It was believed for long that this surface should decompose, like MgO(1 1 1), into (1 0 0) facets. However, recent theoretical studies indicate that it may be stabilized by a p(2 × 2) reconstruction [134], in the form of three atomic layer high micro-pyramids exposing (1 0 0) faces. Molecular dynamics simulations [135] predict that the NiO(1 1 1) surface could also be stabilized by oxidation and that Ni atoms should be on top of the pyramids. A few studies have been performed on NiO(1 1 1) ultra-thin films. A p(2 × 2) LEED pattern was reported for 550 K grown films on Au(1 1 1) [136] and for room temperature grown films on Ni(1 1 1) [137]. However, because the NiO(1 1 1) single-crystal surface is a good insulator [138], no experimental investigation with electron based techniques was available on single crystals. This motivated the GIXS study on a NiO(1 1 1) single-crystal surface.

Measurements were first performed on the air-annealed samples just after they were inserted into the UHV chamber, without further treatment. In-plane measurements (Figs. 23(a) and (d)) along the high symmetry directions already showed indications of a p(2 × 2) reconstruction of the surface. Quantitative measurements of the (01l), (10l) and (11l) CTRs showed that the surface of the air-annealed sample is probably terminated by two planes of light elements (C, O or N) [139]. It was not possible with GIXS to distinguish between a Ni terminated surface decorated with CO molecules and an O terminated surface with adsorbed N or C on top, but it ruled out the bulk truncation and a Ni terminated surface covered by hydroxyl molecules. The relaxations for the best model are small: +0.12 Å (1.6%) for the top layer and −0.2 Å (−2.7%) for the second layer, and the overall roughness is extremely small: 0.1 Å rms.

The surface was next annealed in UHV at 860 K during 30 min, resulting in desorption of the typical air contaminants. The in-plane measurements (Figs. 23(b) and (e)) revealed two new and strong features: extra peaks at each half integer value corresponding to a p(2 × 2) reconstruction, and Bragg peaks at the exact positions expected for epitaxial relaxed FCC Ni(1 1 1) ($h = 1.17$ and 2.24 in Fig. 23(b)). Out-of-plane scans confirmed the 3D character of the metallic Ni. The width in l of the Ni Bragg peaks, ~ 0.18, corresponds to an average island height of 19 Ni layers. This contrasted with the almost constant intensity of the p(2 × 2) rods up to large $Q_\perp$'s, that indicated that the p(2 × 2) reconstruction is essentially 2D. No indication was found of the $(\sqrt{3} \times \sqrt{3})$R30° observed in previous investigations, which was attributed to contamination of the surface by Si that had segregated from the bulk. Indeed, AES and XPS experiments do not revealed any contamination.

In addition to these features, a succession of regularly spaced rods arranged on a very well-defined network (Fig. 24) was found, with a periodicity of 0.2 in the NiO(1 1 1) reciprocal lattice corresponding

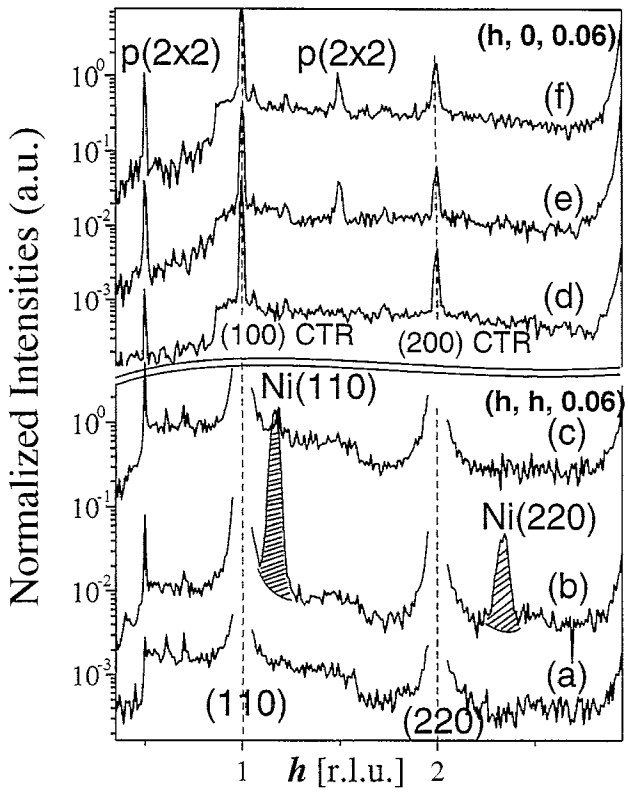

Fig. 23. In-plane measurements along the (h h $l = 0.06$) (a, b and c) and the (h 0 $l = 0.06$) (d, e and f) directions of the NiO(1 1 1) surface after air annealing (a and d), UHV annealing (b and e) and after in situ oxidation (c and f). Note that the strong CTRs of NiO are present in the (h 0 0.06) direction showing again that the topmost surface planes of NiO(1 1 1) are very well defined. The curves were shifted for seek of clarity but the relative intensities are comparable. Ordinate scale is logarithmic. The surface basis vectors describe the triangular lattice that is appropriate for (1 1 1) surfaces, they are related to the bulk ones by: $\boldsymbol{a}_s = [\bar{1}\,1\,0]/2, \boldsymbol{b}_s = [0\,\bar{1}\,1]/2$, and $\boldsymbol{c}_s = [1\,1\,1]$.

to a 5 × 5 superstructure on the coincidence network between NiO and Ni. Indeed the lattice mismatch between 5 periods of NiO and 6 periods of Ni is only 1.3%. The corresponding rods have only significant intensity for $l > 0.2$, and extend to large l's with a smooth maximum around $l = 0.5$. As is shown in Section 5.3, this is typical of a superstructure located at the interface between Ni(1 1 1) islands and the NiO(1 1 1) surface, with a limited extension in the Ni clusters. This superstructure is likely to be an interfacial network of misfit dislocations relaxing the lattice parameter misfit. From these observations, it was concluded that the surface is reduced, when heated to 860 K in UHV.

The surface was next heated in 2.5×10^{-6} mbar partial pressure of oxygen at 860 K during 45 min, which led to vanishing of the metallic Ni clusters and of the associated dislocation network. Only the p(2 × 2) reconstruction remained with its 2D character (Figs. 23(c) and (f)). The signal on the NiO CTRs increased showing that the surface was flatter than in any of the previous situations.

Quantitative measurements of the p(2 × 2) reconstruction were performed on two different samples. A total of 71 reflections were measured with 27 non-equivalent ones. Fig. 25(a) shows the experimental Patterson map, and Fig. 25(b) shows the Patterson map calculated for the octopolar reconstruction

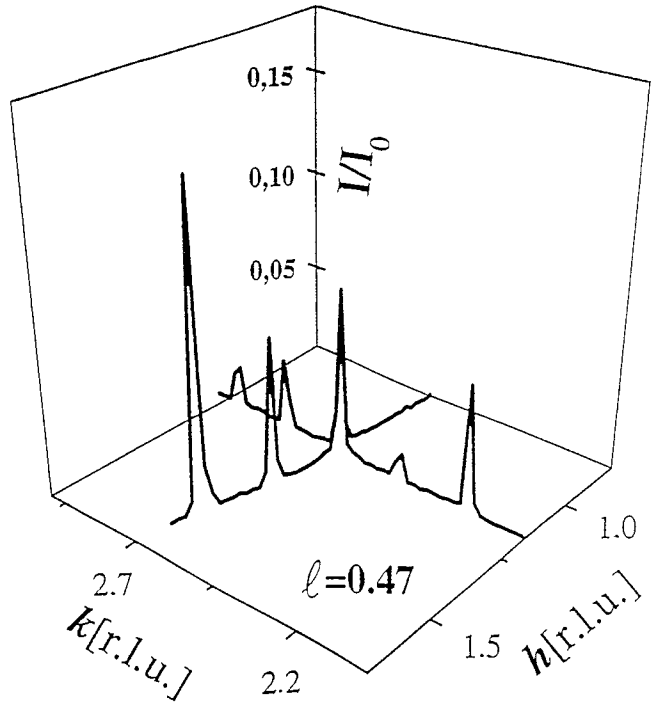

Fig. 24. Scans through the (5 × 5) interfacial superstructure around one of its rods (1.17, 2.57, 0.47). This representation was chosen for ease of data processing although the real angle between [h 0] and [0 k] is 60°. Ordinate scale is linear.

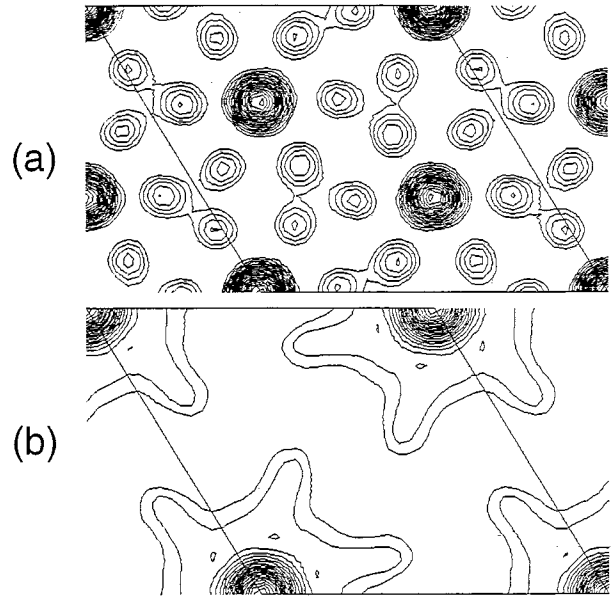

Fig. 25. Experimental Patterson map of the NiO(1 1 1)-p(2 × 2) surface (a, top) and calculated Patterson map for the theoretically predicted p(2 × 2) octopolar reconstruction ($\chi^2 \approx 22$) (b, bottom).

without relaxation, which is identical (except for a scale factor) for O and Ni terminated pyramids. Two prominent features of the experimental map are completely lacking and the χ^2 is large ($\chi^2 \approx 22$). The agreement could not be significantly improved by allowing relaxations of the atom positions. Thus, the structure of the p(2 × 2) reconstruction is clearly not the predicted octopolar one. At the time this report was written, work was under way to propose a new structure from the GIXS data.

In summary, it was shown by GIXS that after an air annealing the NiO(1 1 1) surfaces are stable, flat, and covered by a layer of adsorbed gases. After in situ annealing and oxidation, a p(2 × 2) reconstruction takes place but it is not the theoretically predicted octopolar one. More quantitative investigations of this surface are under way.

4.6. *Other oxide surfaces: $SrTiO_3(0\,0\,1)$, $Cr_2O_3(0\,0\,0\,1)$, ...*

Like the MgO(0 0 1) surface, $SrTiO_3$(0 0 1) is a very commonly used substrate for the growth of high-T_c superconductors, $YBa_2Cu_3O_{7-x}$ in particular. $SrTiO_3$ is also a model photo-catalyst for the dissociation of water. The surface exhibits oxygen and strontium defects, which are believed to act as centers for catalytic reactions. The (0 0 1) surface can terminate with two types of plane, SrO, or TiO_2, and the stoichiometry of each plane can be varied according to the preparation conditions. Fig. 26 shows the ideal surface with both terminations illustrated. Depending on the degree of surface reduction, several reconstructions have been observed: (2 × 1), (2 × 2), c(2 × 2), $(\sqrt{5} \times \sqrt{5})$R26.6°, and c(6 × 2). Substantial relaxation has been theoretically predicted [140] and deduced from LEED measurements [141]. Reconstruction of the SrO terminated surface to a ferroelectric monolayer below 100 K is also predicted and observed by LEED. For these reasons, several groups [142] investigated the $SrTiO_3$(0 0 1) by the GIXS technique.

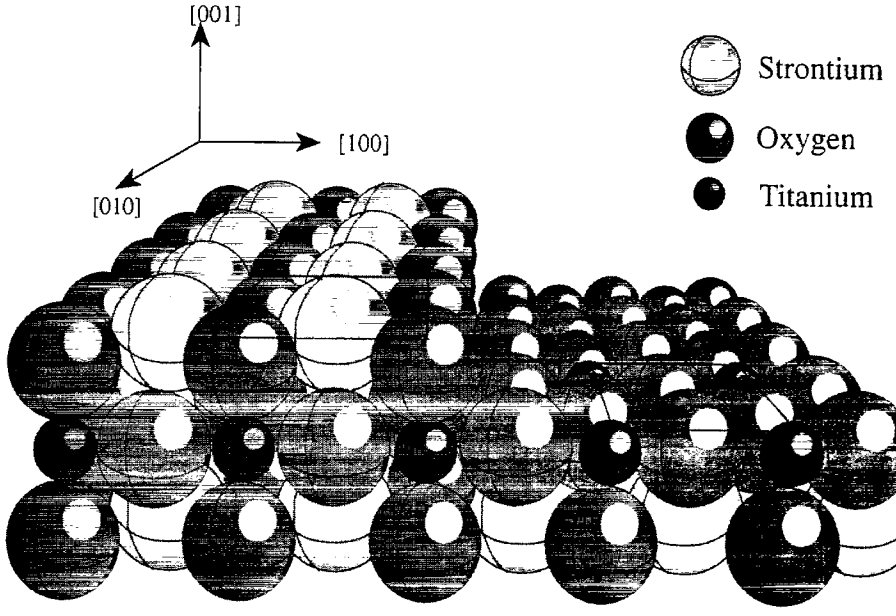

Fig. 26. Space filling model of $SrTiO_3$(0 0 1) showing the SrO terminated surfaces (left-hand side of diagram) and the TiO_2 terminated surface (right-hand side). The unit cell corresponding to each termination is outlined, and has dimensions 3.905 × 3.905 Å (reprinted from [144]).

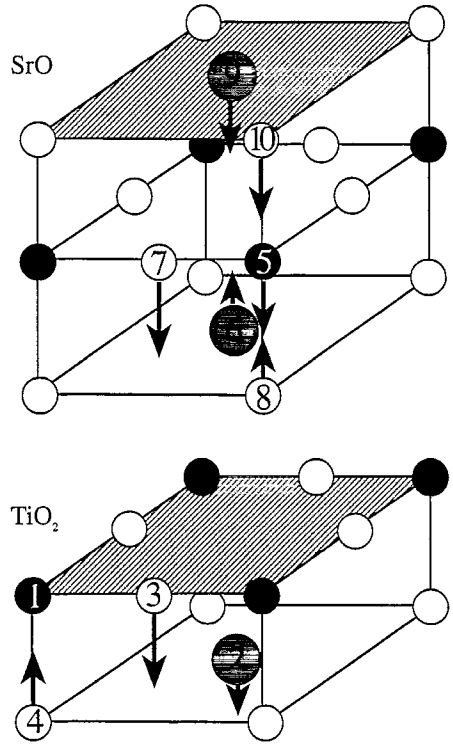

Fig. 27. Diagram showing the atomic displacements for both surface terminations of $SrTiO_3(0\,0\,1)$-(1×1) at room temperature. The black circles represent Ti, the open circles O and the shaded circles Sr (reprinted from [144]).

A recent conference paper [143] describes a GIXS study that allowed determination of the surface termination. Chemically treated surfaces were found to be terminated by a TiO_2 plane, and annealed surfaces were mostly terminated with a TiO_2 plane, with a small portion covered by a SrO plane. Recent measurements were performed on the $SrTiO_3(0\,0\,1)$-(1×1) surface [144] using the ID3 diffractometer of the ESRF. The surface was prepared in situ by repeated cycles of Ar^+ sputtering and annealing at 900 K. This was followed by an anneal at 900 K in 1×10^{-6} mbar O_2 to restore the surface stoichiometry and prevent the formation of reconstructions induced by oxygen vacancies. Three CTRs were quantitatively measured and fitted. Ten atomic displacements and 6 Debye–Waller parameters were used, with three additional parameters: scale factor, roughness, and surface fraction. The best fit was achieved with a surface that is 22% SrO-terminated and 78% TiO_2-terminated. Fig. 27 schematically shows the vertical atomic displacements deduced from the best fit, for the two kinds of terminations. These results do not compare very well with recent theoretical calculations of the surface relaxation [145,146].

The $c(6 \times 2)$ reconstruction, which is obtained by a combination of annealing under oxygen and UHV, has been shown remarkably long-range ordered and stable in O_2 or in ambient air [147]. It has been characterized by LEED and STM [147], and very recently by GIXS [148]. Fig. 28 shows the Patterson map deduced from measurements of in-plane reconstruction rods from this surface, which are still under analysis.

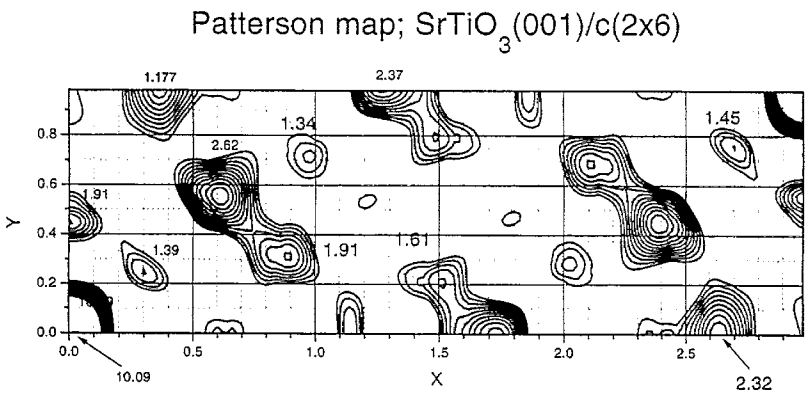

Fig. 28. Patterson map of the $SrTiO_3$(0 0 1)-c(2 × 6) reconstruction (reprinted from [148]).

An original GIXS study was performed on the buried interface of a $SrTiO_3$ bicrystal, prepared by fusing two 18.4° miscut crystals (corresponding to a (1 0 3) orientation of the normal to the interface) at elevated temperature and pressure [149]. CTRs were quantitatively measured. Modeling showed that the interface region is very narrow, with a thickness of ~ 11 Å, and has a significantly changed atomic structure.

Recent measurements of the CTRs have been performed on the Cr_2O_3(0 0 0 1)-(1 × 1) surface [150] in order to determine the termination and relaxation in a way very similar to that described in Section 4.3.1 for the Al_2O_3(0 0 0 1) surface. The data were not yet analyzed at the time this review was written.

5. Metal/oxide interfaces

5.1. *Introduction*

Studying thin films by performing in situ GIXS measurements during metal deposition, from the very early stages up to fairly thick films, allows one to address many fundamental issues in surface science, some of which are listed here.

First, is there epitaxy, and if yes, what are the orientational relationships? What is the structural quality of the growing film? What is the registry of the metal with respect to the substrate, i.e. adsorption site and interfacial distance between the last oxide plane and the first metal plane? In the case of a metal/MgO(0 0 1) interface, is the metal on top of the O ions or the Mg ions of the last MgO(0 0 1) plane or in between, above the octahedral site?

How does this interfacial distance evolve with the thickness of the metal film? What are the growth modes and the morphology of the growing film? How is the accommodation of the lattice parameter misfit performed? When does the transition from elastic to plastic relaxation happen? Which defects are involved in the process of plastic relaxation: stacking faults or interfacial dislocations? What is the interplay between these structural relaxation processes and the morphology? Finally, can we improve the structure and morphology of thick films by UHV annealing? Can annealing studies provide kinetic information?

When the film thickness is larger than a few hundreds of angstroms, the top of the metal film is generally close to be fully relaxed to bulk lattice parameter. From the point of view of elasticity, the relaxation of an epitaxial film on a substrate is governed by the lattice parameter misfit f. In the case of parallel epitaxy, like for Ag/MgO(0 0 1), f is defined by: $f = (a_f - a_s)/a_s$, where a_f and a_s are, respectively, the film and substrate bulk lattice parameters. For small values of f ($< 10\%$), the lattice parameter relaxation is in general realized by localized, ordered misfit dislocations [151], in which case the interface is said "semi-coherent". When f is larger, the misfit dislocation density becomes so large that they cannot remain localized and organized, and the proportion of the interface in "poor epitaxy" increases. In that case, the interface is said "incoherent". There are, however, numerous exceptions. For instance, the Pd/η-Al_2O_3(1 1 1) interface is incoherent with $f = 2.7\%$ [152] as well as the Au/MgO(0 0 1) interface ($f = 3\%$) [153] the Cu/Al_2O_3 interface ($f = 10\%$) [154] and the Ag/CdO one [155], while the Au/ZrO_2(1 1 1) interface is semi-coherent with a very large misfit of 22% [152]. The technique of choice to investigate interfacial dislocations is high resolution transmission electron microscopy (HRTEM) [152]. However, HRTEM does not always provide all the required information concerning dislocations, and may in some cases lead to erroneous conclusions. In these cases, it may be useful to resort to GIXS, as will be shown in the few examples below.

Four examples will be given of in situ studies during growth: first for the three FCC metals, Ag, Pd and Ni, with cube on cube epitaxy on MgO(0 0 1) (with increasing misfit of 3%, 7.6% and 16.4% respectively), second for a BCC metal, Fe, with 45° rotated epitaxy, and a remaining misfit of 3.3%. The Ag/MgO(0 0 1) system has been chosen by most theoreticians as a model because it is one of the most simple metal/oxide interfaces: the MgO(0 0 1) surface is non-polar, epitaxial relationships are particularly simple (square/square) with a small lattice misfit (3%) and chemical and charge transfer contributions to bonding are negligible. Many studies have been devoted to the Pd/MgO(0 0 1) interface because it is a model catalyst. The Fe/MgO(0 0 1) and Ni/MgO(0 0 1) interfaces are also of particular interest because they are simple transition metal/oxide interfaces in which the metal is ferromagnetic.

The analysis of interfacial dislocation network by GIXS will be described in the cases of the Nb/Al_2O_3(0 0 0 1), Ag/MgO(0 0 1) and Pd/MgO(0 0 1) interfaces.

The main characteristics deduced from GIXS in the different systems discussed below are summarized in Table 1.

5.2. *In situ studies of the first stages of formation of metal/oxide interfaces*

5.2.1. *Ag/MgO(0 0 1) [156,157]*

In this model metal/oxide system, all theoretical calculations minimize the interfacial energy with respect to two structural parameters: the silver adsorption site (on top of O atoms, on top of Mg atoms or in between, above the octahedral sites of the substrate), and the interfacial distance between the MgO(0 0 1) surface and the first Ag(0 0 1) plane. However, although crucially needed by theoreticians to evaluate and refine their models [158], no accurate experimental determination of these parameters was available at the time the GIXS study was performed. The aim of the GIXS study was to determine these parameters and their evolution with the Ag thickness, together with analyzing the growth mode.

The scattered X-ray intensity measured during radial in-plane scans along $(h, h, l = 0.1)$ and $(h, 0, l = 0.1)$ is shown in Fig. 29 around $h = 2$, for deposited thickness θ ranging from 0 to 72 Ag monolayers (ML). These scans show the presence of relaxed Ag(0 0 1) in cube/cube epitaxy with the

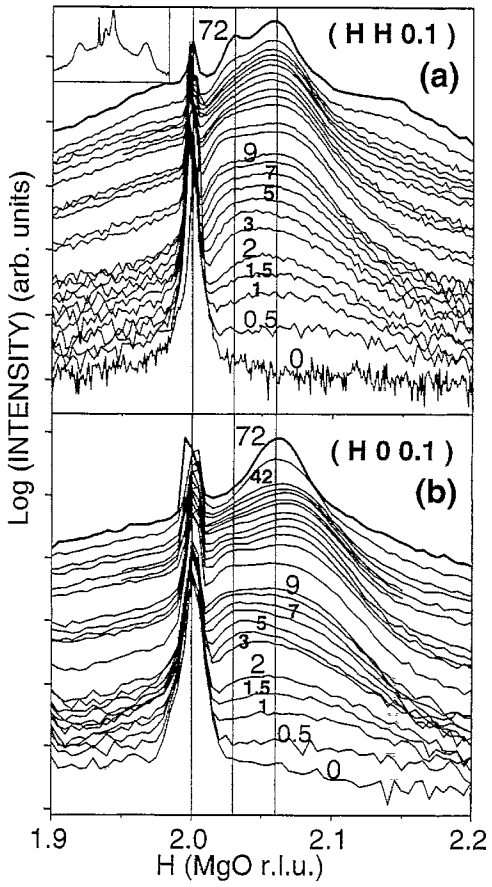

Fig. 29. Radial scans at $l = 0.1$ along the (h h 0.1) (a) and (h 0 0.1) (b) directions, as a function of the amount of deposited Ag (0,0.5,1,1.5,2,3,4,5,6,7,8,9,10,11,13,15,17,19,22,25,28,32,36,42 and 72 ML), which is indicated above the corresponding curves. The curves corresponding to the different deposits have been shifted vertically for clarity. Vertical lines indicate the $h = 2$, $h = 2.03$ and $h = 2.06$ positions. The inset is a scan at $l = 0.16$ along the (h h 0.16) direction, performed at 300 ML.

MgO(0 0 1) substrate from the very beginning of Ag deposition, as revealed by the broad peak in both directions, approximately centered at the expected position ($h = 2.062$) for bulk Bragg peaks of Ag in cube on cube epitaxy. The integrated intensity of this relaxed Ag component increases linearly with θ, showing that, at all deposits, most of the Ag is incorporated in this relaxed part. However, at the early stages of Ag deposition, another significant effect is present: between 0 and 2 ML, a significant decay of the MgO(2,2, $l = 0.1$) intensity occurs. This decrease originates from a destructive interference between the waves scattered by the Ag layer and the substrate on the (2,2,0.1) MgO CTR. This implies that at least part of the deposited Ag is initially perfectly on site, i.e. exactly located above atoms of the substrate. Rocking scans of the MgO(2,2,0.1) peak are resolution limited (0.003°) whether or not Ag is present, and correspond to a correlation length of the registered Ag of at least 200 nm. This indicates that the epitaxial site is perfectly well defined: the Ag atoms responsible for this destructive interference effect are correlated via the substrate. This registered part can be selected in reciprocal space, since it yields rods that are located exactly at the same integer (h, k) values as the MgO CTRs. The interference

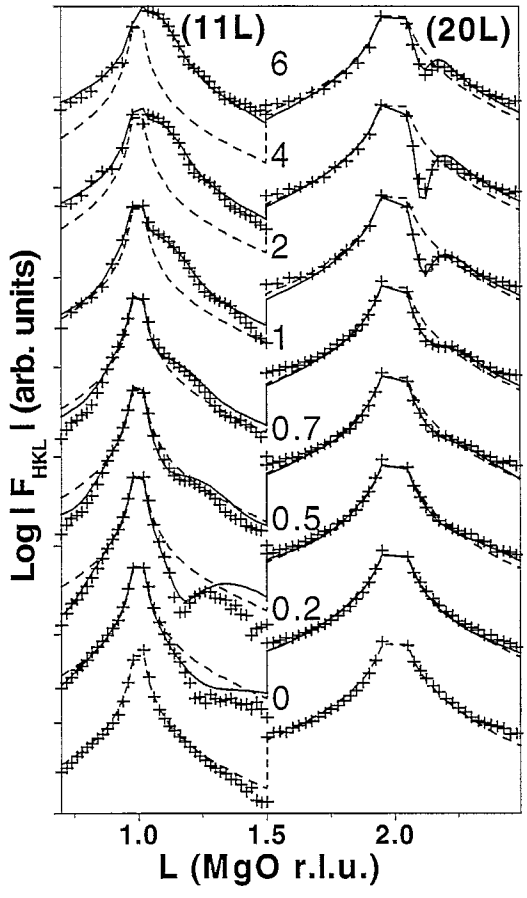

Fig. 30. Comparison between the measured (crosses) and calculated (solid lines) CTRs for various Ag thickness. The dashed lines correspond to the clean MgO. The (11l) and (20l) CTRs have been represented on the same l-scale although they are at different h,k values. The curves corresponding to the different amounts of deposited Ag are shifted vertically for clarity.

between the waves scattered by the MgO substrate and by the registered Ag film yields modulations of the intensity along the bulk CTR directions which can be analyzed to determine the structural parameters of interest: site of epitaxy and interfacial distance.

For this purpose, the (11l) and (20l) rods were measured as a function of θ (Fig. 30). The sign of the interference (destructive on the high l side of both the (1 1 1) and (2 0 2) Bragg peaks of MgO, at least for very small amounts deposited, since for large amounts, the MgO(11l) CTR is rapidly overcome by the Ag one) at the first stages of deposition unambiguously allows the assignment of the epitaxial site: the Ag atoms sit on top of oxygen atoms of the substrate. The location of the Ag intensity in a small l range on the high l side of the MgO Bragg peaks indicates that the surface of the registered part is rougher than the substrate's surface.

Quantitative analysis of the Ag/MgO CTRs was carried out with four parameters: (i) the total occupancy of registered Ag (i.e. the amount of Ag ML that is perfectly on site); (ii) the interfacial distance; (iii) the average out-of-plane distance between registered Ag; and (iv) the additional roughness of the registered Ag film with respect to the substrate. Some of these parameters are reported

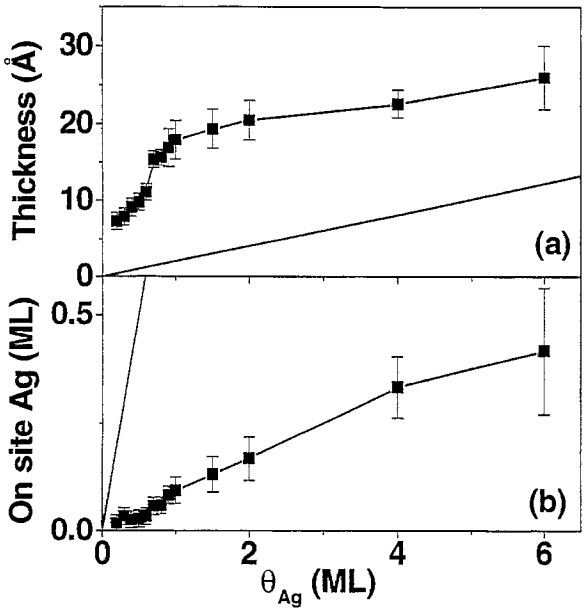

Fig. 31. Evolution with the amount of deposited Ag of the "on site" Ag thickness (a, top) and of the amount of "on site" Ag (b, bottom), expressed in number of ML.

in Fig. 31 as a function of deposited thickness. The main results are that only a small fraction of the deposited Ag, amounting to 10% for $\theta \sim 5$ ML is perfectly on site, and that the thickness of this registered part is always larger than the equivalent thickness deposited, which shows that the growth is three-dimensional from the very beginning. Despite the fact that most of the Ag deposited is relaxed, the selection of the registered fraction on CTRs allowed a determination of the parameters of interest. The interplanar distance in Ag is very close to that in bulk silver, which is consistent with registered Ag surrounded by relaxed Ag. The interfacial distance is found to increase at the beginning of deposition, and stabilize around an average value of 2.5 Å. In the first stages of growth, the smaller interfacial distance may originate from the different local environment of Ag atoms at the interface. Indeed, all theoretical studies indicate that there is little charge transfer between Ag and O, when considering a bulk Ag crystal above the MgO(0 0 1) surface, but this may not be the case for isolated atoms or very thin films on the surface. These results were next compared to the theoretical models of the Ag/MgO(0 0 1) interface. As far as the site of epitaxy is concerned, the image interaction model predicts that the Ag atoms are above the octahedral sites the MgO(0 0 1) surface but this translational state was shown to result from the hard-core repulsion used [159]. The most recent ab initio calculations [160,161] show that the energetically favored configuration is for Ag on top of oxygen atoms of the substrate. The GIXS results experimentally demonstrate this latter conclusion for the first time. They were later confirmed by an EXAFS investigation [162]. Regarding the interfacial distance, the experimental steady state value is very close to the most recent ab initio calculations: 2.49 Å [161,163]. This, along with the adsorption site, shows that recent ab initio calculations give a good description of the Ag/MgO(0 0 1) interface.

This quantitative analysis thus demonstrated for the first time the possibility to characterize by GIXS a small fraction of the Ag film: those Ag atoms that are perfectly on top of substrate sites, and to

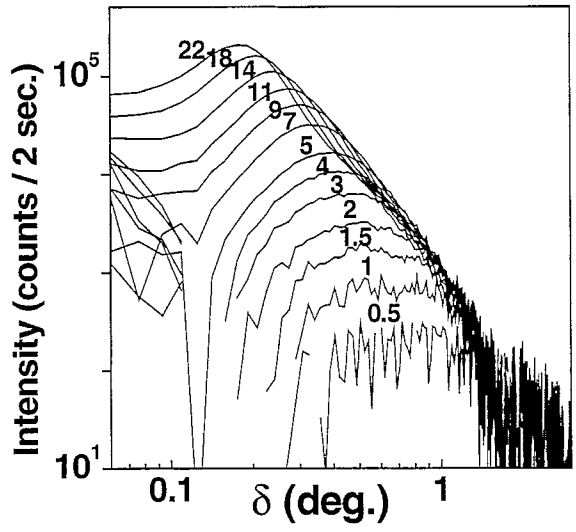

Fig. 32. Intensity scattered at small angles, as a function of the in-plane scattering angle δ, for different amounts of deposited Ag. The amount of Ag in ML is indicated above the corresponding curve. The intensity measured on the clean MgO was subtracted.

precisely determine the epitaxial site and interfacial distance and their evolution from the very early stages of deposition to thick deposits. The next question was what could we learn from GIXS about the morphology and the structure of the major part of the Ag film.

As far as the morphology is concerned, since the adhesion energy of Ag on Ag is larger than Ag on MgO (1.36 eV and 0.45 eV, respectively [164]), Ag is expected to grow in the form of islands. The growth morphology was actually probed by performing GISAXS [44–46] measurements as a function of θ (Fig. 32). A measurable peak appears at $\theta = 0.5$ ML and then increases in intensity with θ, while getting narrower and moving toward the origin of reciprocal space. This small angle pattern is typical of small correlated islands [44,46] that nucleate, grow and coalesce as the film gets thicker. The deposited Ag therefore rapidly evolves toward the classical island growth regime (Volmer–Weber). The average distance between islands can be easily deduced from the location of the intensity maximum, and the average island diameter can also be deduced by several means [40,44–46], assuming given shapes of the islands, for instance, hemispherical in the present case.

If GISAXS can provide useful information of the morphology, GIXS (performed at wide angles) can provide very detailed information on the structure of the relaxed part of the Ag film. For that purpose, rocking scans were systematically performed on the relaxed Ag Bragg peaks as a function of θ. They were all found of Lorentzian lineshape, perfectly centered on the $\langle 1\,1\,0 \rangle$ direction, which shows that there is no rotation between the relaxed structure and the substrate. The lineshape corresponds to exponentially decaying correlation functions with small (~ 100 Å) correlation lengths increasing with θ. The corresponding "domain size" and its evolution with θ was found to be in good agreement with the island size deduced from GISAXS.

Further information was gained on the relaxation process of the lattice parameter by looking in more detail at the intensity distribution along the radial scans of Fig. 29. Apart from a broadening induced by the finite island size, the lineshape mainly reveals the distribution of lattice parameters in the silver film.

Between 0 and 4 ML, the scattering is composed of only one component, whose center progressively shifts from $h = 2.06$, corresponding to Ag fully relaxed to its bulk lattice parameter, towards an intermediate value, ~ 2.03 for $\theta \sim 4$ ML. Above ~ 4 ML, in both directions, the scattering progressively splits into two components centered, respectively, around $h = 2.03$ and $h = 2.06$, and whose exact positions evolve with θ. While these two components remain up to large thickness along the (h h 0.1) direction, the intermediate component, around $h = 2.03$, progressively disappears along the (h 0 0.1) direction, for thickness larger than 20 ML. We will see in Section 5.3.2 that, for thick enough films, the satellite around (2.03 2.03 l) arises from the formation of a well-ordered network of interfacial dislocations releasing the lattice parameter misfit between Ag and MgO. As shown in Section 5.3.2, this ordered network does not yield any satellite around (2.03 0 l), since this is the location of an extinction for this structure. Thus, at intermediate thickness, between $\theta \sim 4$ and 20 ML, the scattering around $h = 2.03$ in both directions does not arise from a new interfacial supercell, but is rather due to an inhomogeneous distribution of lattice parameter within the Ag islands. The observed evolution was analyzed as follows. At the very beginning (below 1 ML), the relaxed Ag fraction is made of very small islands of fully relaxed Ag, with the lattice parameter of bulk Ag. At this stage, the width in radial scans is completely dominated by the finite size effect. As shown by GISAXS and by the decreasing widths of Ag scattering, both radially and transversely, the islands next become larger. At the same time, the Ag becomes more strained by the MgO substrate, with an average in-plane lattice parameter intermediate between that of MgO and Ag for $\theta \sim 4$ ML. This is likely connected to an increased interfacial area over Ag volume ratio, i.e. to a decrease of the aspect ratio (height/width) of the islands. Until 4 or 5 ML, radial scans are composed of only one contribution, because the strain in Ag is homogeneous. In other words, there is continuity between net planes in the MgO substrate and in the Ag islands: the Ag islands are said to be coherent with the substrate. The elastic strain energy stored in the islands increases as the islands grow in size, up to a point, around 4–5 ML, where it becomes energetically more favorable for the islands to release part of the strain by introducing a defect, such as a stacking fault or an interfacial dislocation. At this stage, the coherency with the substrate is lost, and the misfit relaxation is said to be plastic, as opposed to elastic when the islands were still coherent. Therefore, the strain within the islands become inhomogeneous, leading to the two components observed along both radial directions. The component around $h \sim 2.06$ is due to fully relaxed Ag, in which the strain is indeed homogeneous, while the component around $h \sim 2.03$ arises from the regions surrounding the cores of the interfacial dislocations, where the strain is strongly inhomogeneous. A detailed study was performed to determine whether these structural defects were appearing in the center of islands or near their edges [40,157]. The observed intensity distribution in the two directions could only be explained by locating the net plane discontinuity at the edges of the islands. This is the first experimental evidence that misfit dislocations nucleate at the edges of islands during the growth of this kind of metal/oxide systems.

The intensity of the shoulder around $h \sim 2.03$ decreases above 20–30 ML, until complete disappearance above 50 ML. This can be related to the beginning of the coalescence of the Ag islands around 20 ML, as shown for instance by the increase of the critical angle for total external reflection, which is due to an increase in the average density of the Ag layer. As islands coalesce, the interfacial misfit dislocations can reorganize into the energetically favored ordered interfacial network, resulting in an extinction of the intensity around (2.03 0 l), and a well defined satellite around (2.03 2.03 l).

In summary, this GIXS study provides much information concerning the growth and relaxation at the Ag/MgO interface, as summarized in Fig. 33. The growth of Ag on MgO(0 0 1) was shown to be

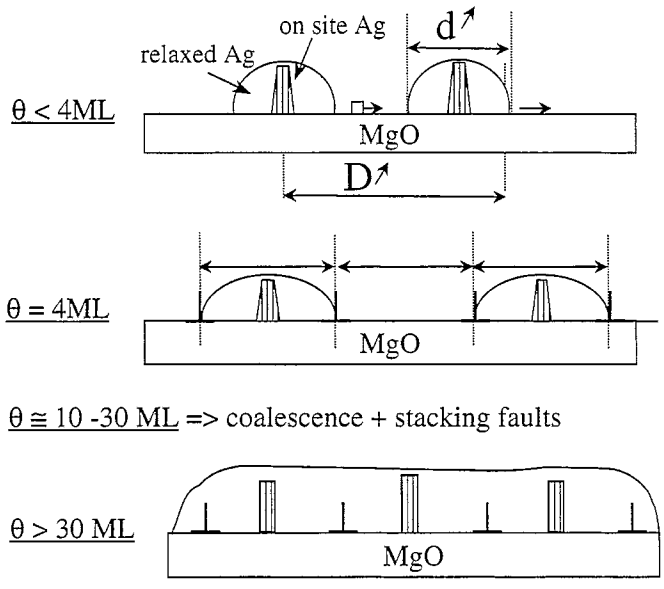

Fig. 33. Schematic representation of the Ag film morphology and structure with three growth regimes: coherent 3D growth incoherent 3D growth and semi-coherent Ag film.

always of the 3D Volmer–Weber type. Between 0 and 4 ML, coherent Ag islands form and grow laterally, with decreasing aspect ratio. Ag is fully relaxed on the edges at the very beginning, and becomes increasingly strained to the MgO in-plane lattice parameter as the islands grow laterally. Around 4 ML, the islands reach a lateral critical size of $\sim$ 100 Å for which interfacial defects such as misfit dislocations and stacking faults are naturally introduced at the edges. The coalescence happens around 10–30 ML. Above 30 ML, the film is continuous, and interfacial dislocations rearrange on a regular network. The fraction of Ag that is on-site is made of columns located at the center of islands before coalescence, and in between dislocation lines after.

5.2.2. *Surfactant-assisted growth of Ag on MgO(0 0 1)*

Finding new ways to improve the adhesion of a metal on a ceramic surface is of great importance for many applications. The growth of Ag on MgO(0 0 1) is 3D because Ag does not thermodynamically "wet" MgO, but also because of the lattice misfit. The introduction of adequate surfactants to promote 2D with respect to 3D growth has been found very efficient in numerous systems, both in homoepitaxy [165–168] and heteroepitaxy [169,170]. In particular, antimony (Sb) has been shown (actually by GIXS) to be a surfactant during the homoepitaxial growth of Ag, of both (1 1 1) [165] and (1 0 0) [166] orientations. For the Ag/MgO system, Sb could be expected to induce several kinetic effects promoting a 2D growth, like an increase of the nucleation density, the concentration of lattice accommodation in Sb rich regions, the earlier formation of the misfit dislocation network as well as earlier appearance of the coalescence or the suppression of stacking faults due to the dendritic shape of islands inducing connections between islands, as has been observed for instance in the case of the homoepitaxial growth of Cu(1 1 1) [167]

A GIXS study was thus performed [40] to investigate the effect of Sb as a surfactant during the heteroepitaxial growth of Ag(0 0 1) on top of MgO(0 0 1). The same measurements as above were

performed under two conditions for Sb deposition: after deposition of 0.2 ML of Sb on the bare substrate on the one hand, and after deposition of ~ 1 ML of Ag before deposition of 0.2 ML of Sb on the other hand, followed by Ag growth. Whatever the growth conditions, only extremely small differences were observed with and without Sb. The conclusion of this study is that Sb modifies neither the structure, nor the morphology, nor the kinetics of the growth of the Ag/MgO(0 0 1) interface. Complementary AES experiments were performed which showed that Sb does not indeed wet MgO(0 0 1), at least for alternated deposition. Nevertheless, the GIXS technique could be useful to test other ideas to modify the growth, such as the association of a wetting tensioactive element like Fe with a surfactant, or the growth under partial oxygen (or CO) pressure, which is found to improve the wetting in some cases.

5.2.3. Pd/MgO(0 0 1) [171]

Unlike the Ag/MgO(0 0 1) interface, the Pd/MgO(0 0 1) interface had been the subject of a large number of studies [172–181], mainly to investigate the kinetics of nucleation in the sub-monolayer regime between 400 and 800 K. Whatever the temperature, the growth was found to be 3D (Volmer–Weber), with nucleation, growth and coalescence of clusters. These clusters are single-crystal particles, fully relaxed and in cube/cube epitaxy, excepted for the first layer in contact with the MgO(0 0 1), which, according to HRTEM results [173] would be perfectly accommodated. No twins could be detected by HRTEM [173,179], and a SEELFS study performed at the Pd $N_{2,3}$ edge [182] concluded that the Pd atoms adsorb on top of Mg ions. In addition, an HRTEM study of the Pd/MgO(0 0 1) interface formed by internal oxidation [179] concluded that the 7.6% misfit is accommodated by a network of interfacial dislocations of $\langle 1\,1\,0\rangle$ orientation and $\frac{1}{2}\langle 1\,1\,0\rangle$ Burgers vector, in agreement with the O-lattice theory.

The GIXS experiments were aimed at studying the growth morphology at room temperature, the epitaxial site and interfacial distance, as well as characterizing the interfacial dislocation network. They were performed during the in situ growth at room temperature of Pd on MgO(0 0 1) substrates of high quality, prepared according to the procedure described in Section 4.2. The ID32 ESRF beamline [54] and the W21 surface diffractometer [53] setup were used.

The (20l) and (31l) CTRs measured on the clean MgO(0 0 1) surface and after the RT deposition of $\theta = 1$ ML of Pd are shown in Fig. 34. The large modification induced by deposition shows that, as in the Ag/MgO case, a significant fraction of the Pd deposited is in perfect registry (i.e. on-site or pseudomorphic), and the sign of the interference allows to rule out the octahedral epitaxial site. A quantitative fit was performed of the integrated and corrected CTR intensity, yielding with high accuracy the amount $\theta = 0.5$ ML of Pd in registry, the additional roughness, 2.7 Å (rms) of the pseudomorphic fraction, and the interfacial distance of 2.216 ± 0.02 Å $= 1.05 \times d^{\mathrm{MgO}}_{(002)}$. This (20$l$) CTR is not sensitive to the difference between O and Mg epitaxial sites, unlike the (11l) or (31l) rods, which are very sensitive to the actual site. This is illustrated in Figs. 34(b) and (c) which show the experimental and calculated (31l) CTRs for 1 ML of Pd deposited, superimposed to the CTRs of the bare substrate. The qualitative comparison allows concluding that Pd is above the O ions and not the Mg ones. This is in contradiction with a previous SEELFS investigation, but both the epitaxial site and interfacial distance are in very good agreement with a recent theoretical calculation [183] yielding 2.18 Å. The evolution of the CTRs with θ is very similar to the Ag/MgO(0 0 1) case: above $\theta \sim 1$ML, only a small fraction of the Pd deposited remains on site, most of the film being relaxed. If the epitaxial site is identical to the case of the Ag/MgO interface, the interfacial distance is much smaller (2.216 Å

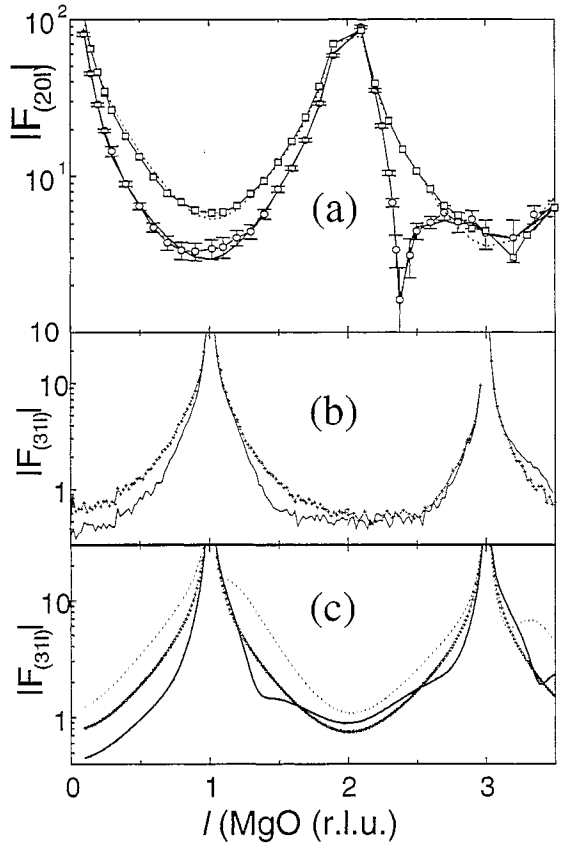

Fig. 34. (a) Modulus of the structure factor of the (20l) CTR, as a function of the perpendicular momentum transfer l, in reciprocal lattice units of MgO, for the clean MgO(0 0 1) substrate (open squares) and after deposition of 1 ML of Pd (open circles with error bars). The best fit is shown by a continuous line. A clear destructive interference effect is observed which yields the amount or registered Pd and the interfacial distance with high accuracy. (b) Experimental modulus of the structure factor of the (31l) CTR, for the clean MgO(0 0 1) substrate (crosses) and after deposition of 1 ML of Pd (continuous line). (c) Simulated (31l) CTR using the parameters deduced from the fit of the (20l) CTR, for the two possible absorption sites, Mg (dashed line) and O (continuous line). The calculated substrate CTR is shown by crosses.

as compared to 2.45 Å in the case of the Ag/MgO interface), likely because of the much stronger bonding in the case of a transition metal like Pd, as compared to a noble one like Ag.

The misfit relaxation process was investigated by performing in-plane radial and transverse scans during growth. Fig. 35 shows the evolution of the intensity along the $(h, h, 0.15)$ and $(h, 0, 0.15)$ directions crossing the MgO CTR (at $h = 2$) and the Pd rod, expected at $h = 2.165$ for fully relaxed Pd. Contrary to the Ag/MgO measurements reported above, the incident angle was kept constant, smaller than the critical angle for total external reflection for both materials. Consequently, only the structure of the top ~ 30 Å is probed and, for thicker deposits, the measurements become insensitive to the interfacial structure. Despite the much larger misfit, the trends are very similar to the Ag/MgO case. Relaxed Pd is found from the very beginning of deposition. At 1 ML of Pd deposited, according to the above result on the registered fraction, half is on site, and half is already relaxed. Although GISAXS was not performed, the growth is almost certainly 3D, since this is the conclusion of all previous

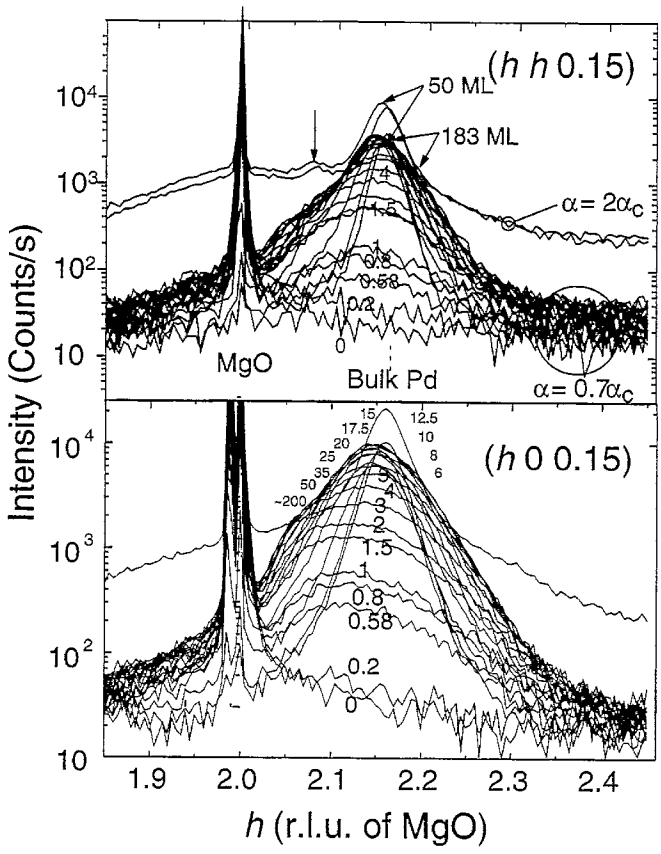

Fig. 35. Radial scans along the (h h 0.15) (top) and (h 0 0.15) (bottom) directions during the growth of Pd on MgO(0 0 1), for different amounts of Pd deposited between 0 and 183 ML.

studies, and is all the way consistent with the X-ray data. Above $\theta \sim 1$ ML, the evolution along both azimuths is very similar to that of the Ag/MgO growth, despite the more than twice larger lattice parameter misfit. The differences with the Ag/MgO case are subtle. Unlike Ag, Pd is never fully relaxed to its bulk lattice parameter, and its average lattice parameter continuously decreases with increasing thickness. It is thus likely that in the Pd/MgO case, the islands are flatter at the beginning than for Ag/MgO, resulting in more strained islands. This deduction is in agreement with HRTEM results, obtained for higher substrate temperatures. Another difference is that the splitting of both the (2 2 0) and (2 0 0) Pd peaks into two contributions, which corresponds to the introduction of misfit dislocations at the edges of the islands, happens earlier, around $\sim$ 1.5 ML. In addition, although special scans were performed to detect the appearance of growth faults, no stacking faults or twins could be detected during the growth of Pd. Finally, the lattice parameter misfit in thick enough films is, as in the Ag/MgO case, relaxed by an interfacial network of misfit dislocations. This is evidenced by the satellite between the MgO and Pd peaks along the (h h 0.15) direction, which is observed when the incidence angle is increased above the critical angle for total external reflection, thus allowing the whole Pd film to be probed.

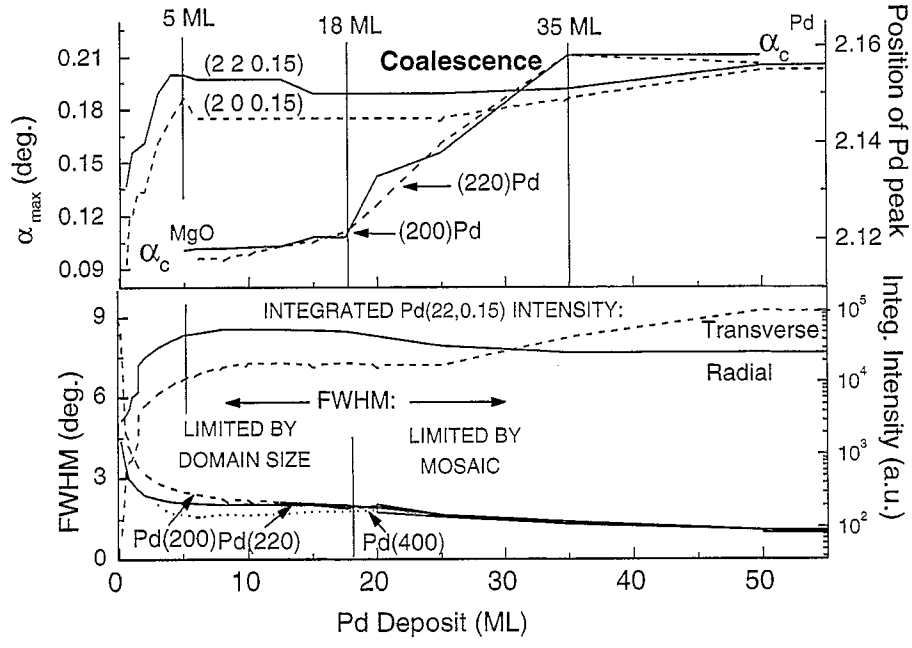

Fig. 36. Evolution with thickness of some parameters of the Pd/MgO interface, deduced from GIXS measurements: critical angle for total external reflection, position of the (200) and (220) Pd Bragg peaks, width and integrated intensity of these peaks.

Additional conclusions can be drawn from Fig. 36, in which the evolution of some parameters is reported as a function of the amount of Pd deposited. The critical angle for total external reflection α_c, measured on the Pd Bragg peaks in both azimuths is found constant below $\theta = 18$ ML, and equal to the critical angle of the MgO substrate. Above 18 ML, it increases linearly until it reaches the critical angle for bulk Pd, for $\theta = 35$ ML, and next stays constant at this value. This evolution can be interpreted as follows: below 18 ML, all the deposit is in the form of small islands, the incident X-ray beam is in transmission through these islands and thus no increase of α_c is found. At 18 ML, the coalescence starts, resulting in some wide islands with a fraction of the surface flat, on which the X-ray beam is totally reflected. During the coalescence process, two effects result in the observed increase of α_c. The first is that more and more islands widen and have a fraction of their surface that is flat and thus externally reflect X-rays. The second is the increase of the film average density toward that of bulk Pd. Above $\theta \sim 35$ ML, the film is continuous. This evolution of α_c thus clearly allows locating the coalescence between 18 and 35 ML. This deduction is corroborated by the evolution of the angular width of the Pd(2 0 0), Pd(2 2 0) and Pd(4 0 0) peaks as a function of θ also reported in Fig. 36. While below $\theta = 18$ ML, these widths are inversely proportional to the modulus of the momentum transfer, which shows that they are dominated by the finite size of the Pd islands, they become equal and independent of it above 18 ML, which shows that they are then dominated by the mosaic spread of the Pd film. The positions of the (2 2 0) and (2 0 0) Pd Bragg peaks are also reported as a function of θ in Fig. 36. They clearly increase very quickly between 0 and 5 ML deposited, and next continue to increase only very slowly. This indicates that the plastic relaxation process is mostly complete at 5ML: nearly all necessary interfacial dislocations are introduced earlier.

In summary, this in situ GIXS study of the Pd/MgO(0 0 1) interface confirmed the possibility to determine unambiguously the epitaxial site, above O ions, and interfacial distance, to locate the coalescence and the onset of misfit dislocations.

A previous GIXS study in this system deserves to be mentioned here [181]. Films of different thickness between 5 and 400 Å were grown in a separate MBE chamber by electron beam evaporation of Pd at a rate of 1 Å/s (1 0 0 times faster than the rate of the study described above) onto MgO(0 0 1) substrates held at 600°C. They were characterized ex situ using a standard laboratory X-ray source. Despite the poor experimental resolution, the average lattice parameter for the (0 0 1) epitaxy was deduced as a function of the deposited thickness. Contrary to our work, no dislocation network was detected, and part of the deposited Pd film was found to have a different epitaxial relationship: Pd(1 1 1)//MgO(0 0 1), with four variants. This is likely to be induced by defects or contamination of the MgO surface.

5.2.4. Ni/MgO(0 0 1) [184]

The misfit for the Ni/MgO(1 0 0) interface in cube on cube epitaxy is much larger (16.4%) than in the two above cases of Ag and Pd. Therefore, the epitaxial strains are not expected to be relaxed by an interfacial dislocation network alone. Alternative processes are expected, such as other epitaxial relationships. In all previous investigations [185–196], Ni films grown on MgO(0 0 1) at room temperature (RT) were claimed to be polycrystalline. Only one group [188] reports a dislocation network associated with the cube on cube (CC) epitaxial relationship. For films deposited by MBE between 400°C and 600°C, pure CC epitaxy is reported in the early stages of the growth, followed by the growth of Ni in (1 1 0) epitaxy [187]. For high temperature and high-pressure growth, interdiffusion and Ni(1 1 1) were observed [189]. An early work [190] has shown that the substrate defects and the strain in the film had large effects on the magnetic domain structure. The magnetism of the Ni atoms was also indirectly used [191–196] to determine the residual strain in the Ni film. However, since all previous investigations of the Ni/MgO(0 0 1) system were performed on films prepared at temperatures above 300°C, the question of the intrinsic strain [191] could only be extrapolated down to RT.

As for the Ag and Pd cases, GIXS was used to describe, in situ, at RT, the growth of Ni on high quality MgO(0 0 1) substrates. Again, the MgO(0 0 1) substrates were prepared as described in Section 4.2, and the experiments were performed at the ESRF, on the BM32 beamline, using the SUV apparatus.

Fig. 37 shows in-plane radial scans along the (h 0 0.1) and (h h 0.1) directions measured for coverage θ between 0 and 125 ML. Ni(0 0 1) in cube on cube epitaxy (CC-Ni(0 0 1)) is found from the very beginning. The peaks of CC-Ni progressively shift towards their expected positions for completely relaxed Ni ($h = 2.39$), although they do not reach it, even at $\theta = 125$ ML. These observations are similar to the Ag and Pd cases, despite the much larger misfit. However, significant differences appear, the first one is that no satellite arising from an interfacial dislocation network could be found, whatever the amount of Ni deposited. This shows that the misfit relaxation must proceed with different routes, and, if interfacial dislocations are present, they are not sufficiently ordered to be observed by GIXS. In addition, new contributions were found: the peak A in Fig. 37(a) and the peaks B and C in Fig. 37(b). The peak A simultaneously appears with the (2 0 0) peak of CC-Ni(0 0 1), increases up to 10 ML and then saturates. The peak B appears around 10 ML and increases up to 50 ML, while the peak C only appears after 50 ML. Rocking-scans showed that all these peaks are well defined, and thus arise from single-crystalline phases of Ni. Because they appear successively, these peaks must belong to different

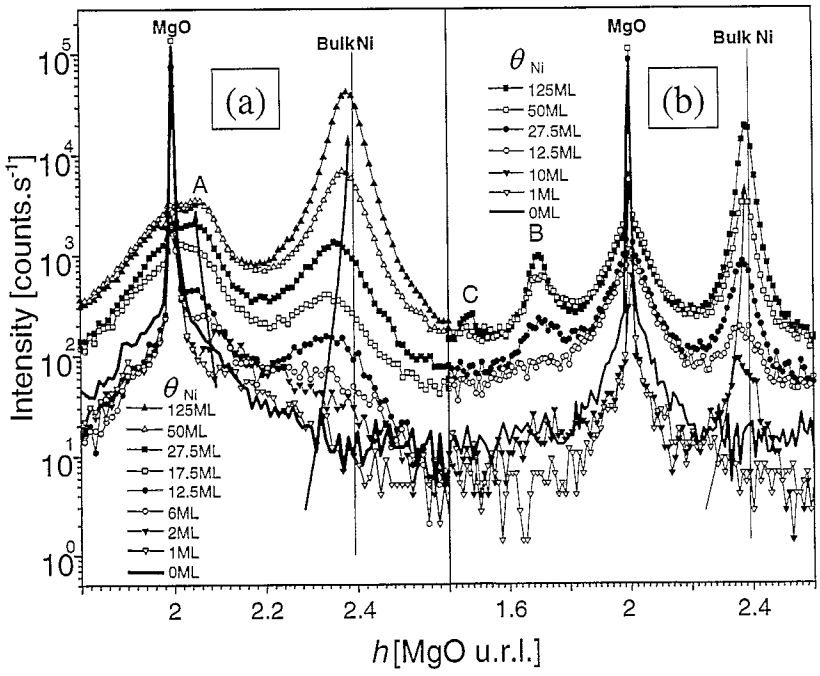

Fig. 37. Evolution of the intensity along the (h 0 0.1) (a, left) and (h h 0.1) (b, right) directions, around $h = 2$, during the growth of Ni on MgO(0 0 1). The arrows indicate the evolution of the peak positions.

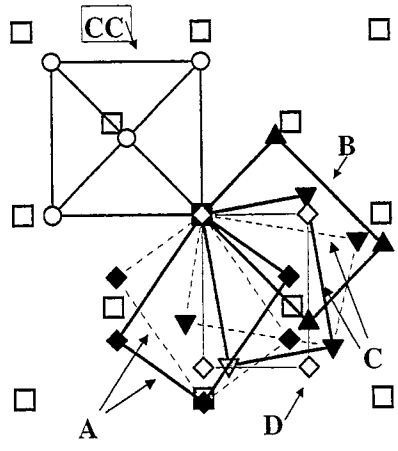

Fig. 38. Schematic representation of the epitaxial relationships. MgO(0 0 1) (□), Ni(0 0 1) (○), A-Ni(1 1 0) (◆), B-Ni(1 1 0) (▲) and C-Ni(1 1 0) (▼).The type of stacking refers to the observed peaks: A occurs between 0 and 10 ML, B between 10 and 50 ML, C after 50 ML and D is always extremely weak.

lattices. An exploration of the reciprocal space showed that they arise from relaxed Ni with the orientation Ni(1 1 0)//MgO(0 0 1) and with three different in-plane orientational relationships labeled A-, B- and C-Ni(1 1 0). These epitaxial relationships are schematically represented in Fig. 38, together with a fourth possible one, labeled D-Ni(1 1 0). All the other peaks measured either in plane or out of

plane were found to arise from one of these five phases (CC, A, B , C and D). It is likely that these different Ni orientations help release the strains in the film. Fig. 38 shows that, among the five possible orientations, A yields the best lattice parameter match along the [1 0 0] MgO direction, with a 2.3% lattice mismatch between [$\bar{1}$ 1 2] Ni and [1 0 0] MgO. The Ni of A orientation is thus likely to grow directly on the MgO(0 0 1) substrate. Since it is in compression, it is likely to help release the tensile strain in the CC-Ni, at least along the [1 0 0] direction. This is corroborated by the significant relaxation of the A-Ni as a function of thickness, opposite to that of the CC-Ni (Fig. 37). Among the three other orientations, B appears first, and is by far predominant. It may be seen from Fig. 38 that its misfit with the MgO is opposite to that of the CC-Ni in one of the ⟨1 1 0⟩ directions, while the misfit between the two orientations, CC and B-Ni is zero in the other ⟨1 1 0⟩ directions.

Transverse scans were systematically performed during growth on several different Bragg peaks of the CC-Ni. The as grown 125 ML (254 Å) thick Ni film has a large in-plane mosaic spread of 3.6°, which dominates all the transverse scans.

Out-of plane scans along the (20l) and (11l) CTRs were also performed. Their intensity strongly decreased during the very first stages of deposition ($\theta < 1$ ML), which showed that, in the submonolayer regime, a significant fraction of the deposited Ni atoms is registered. The observed behavior was well reproduced with a limited increase of the roughness and an O adsorption site. The evolution of the (11l) CTR showed the existence of stacking faults from the very beginning of deposition (0.6 ML), which strongly supports the hypothesis of 3D growth, which is the conclusion of all previous studies.

The 250 Å thick Ni film was next annealed in situ at 950°C for one hour, which resulted in complete disappearance of the Ni(1 1 0) phases, only the CC-Ni(0 0 1) being left, with a much better crystalline quality, as indicated by the smaller peak widths. The in-plane mosaic spread decreased from 3.6° before annealing down to 0.65°. The Ni(0 0 1) was more relaxed ($a_{Ni} = 3.536$ Å) after annealing than after the growth (3.54 Å) but was still not fully relaxed ($a_{Ni} = 3.52$ Å for bulk Ni).

High temperature oxidation of the Ni film was also performed in a constant partial pressure of oxygen (2×10^{-4} mbar). NiO(0 0 1) was found to form from the very beginning, with an associated decrease of the amount of metallic Ni. The resulting NiO layer was slightly expanded ($a = 4.198$ Å as compared to 4.17 Å for bulk NiO). This experiment showed that, when NiO forms, its Bragg peaks are easily resolved, and hence, since no corresponding contribution was observed during the RT growth (Fig. 37), no NiO was formed at the interface.

These different results led to important conclusions. Since most of the atoms of the first Ni layer are on site and since the CC epitaxial relationship is the only one which remains after annealing, a very strong interaction exists between MgO and Ni and the CC epitaxial relationship is the most stable one. However, during the growth at room temperature (RT), i.e. with reduced atomic mobility, other metastable Ni orientations appear (together with large deformations of the CC-Ni), presumably because they help relax the large lattice parameter misfit. Fig. 39 shows the evolution with thickness of the positions of the Ni(2 0 0) and Ni(2 2 0) Bragg peaks, together with their conversions in lattice parameters along both directions. The deformation of the Ni layer is obviously anisotropic. Elasticity theory was shown to reproduce the observed anisotropy only for fairly thick films ($\theta > 30$ ML). It was proposed that the deviation from elasticity for thin deposits is due to the presence of A-Ni(1 1 0), which relaxes the Ni clusters along [1 0 0] and not along [1 1 0].

Since many grains of different orientations were observed, these results could be reconciled with previous TEM investigations, which reported a polycrystalline 3D film. However, even after annealing

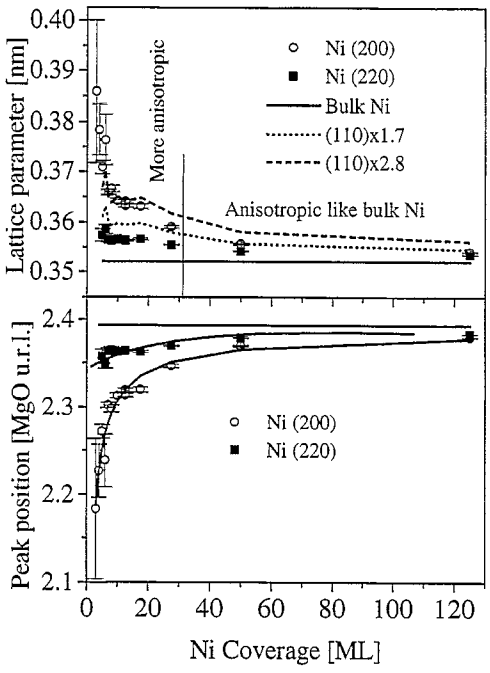

Fig. 39. Positions of the (200) and (220) Bragg reflections from the CC-Ni(0 0 1) (bottom) and their conversion in lattice parameters along both directions (top) (see text).

resulting in a Ni(0 0 1) single crystal film, no ordered network of interfacial misfit dislocations was found. More work is thus needed, for instance by HRTEM, to investigate the interfacial defects, which release the 16.4% lattice misfit at the annealed Ni(0 0 1)/MgO(0 0 1) interface.

5.2.5. *Fe/MgO(0 0 1) [197]*

The above examples show that GIXS is useful to investigate the deformation parallel to the interface and the transition from coherent to incoherent epitaxy. They also show that, in most cases, the interpretation is not straightforward because mosaic and finite domain size effects as well as inhomogeneous deformations must be taken into account in the analysis of the peak profiles. The in situ study of the epitaxial growth of Fe(0 0 1) on MgO(0 0 1) [197] described now is fairly similar, but shows significant differences. The MgO(0 0 1) substrates, provided polished, were organically cleaned, inserted in the vacuum system, and heated to 360°C. This procedure was previously shown to produce a well-ordered LEED pattern, and to result in epitaxial growth of metal films. These substrates were found to possess a high density of step edges, typically 1–3 unit cells in height, which have been found to be nucleation centers for epitaxy. The Fe films were sputtered onto the MgO(0 0 1) substrate held at 360°C by use of planar magnetron sputter guns, operating in 3 mTorr Ar, yielding a sputtering rate of 0.25 Å/s.

Fe growth on MgO(0 0 1) is known to proceed directly through islanding (Volmer–Weber growth), with a 45° rotation between the Fe(0 0 1) and the MgO(0 0 1) unit cell axes. Fig. 40 shows the intensity as a function of $Q_{//}$ in the vicinity of the MgO(2 0 0) Bragg reflection, crossing the Fe(1 1 0) reflection, for different Fe equivalent coverage between 1 and 200 ML. Initially, the Fe(1 1 0) peak position moves to lower momentum transfer values with increasing thickness until about 10 ML, and then increases,

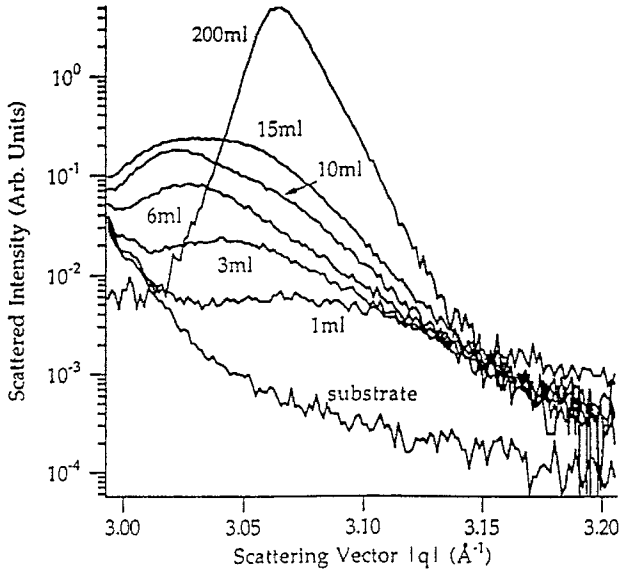

Fig. 40. Measured intensity of the Fe(1 1 0) Bragg peak for various Fe thicknesses, as a function of $Q_{//}$ (radial scan along the MgO(1 0 0) direction) during the growth of Fe(0 0 1) on MgO(0 0 1).

approaching the expected peak location for bulk Fe at 3.087 $Å^{-1}$. The corresponding average lattice spacing is reported as a function of thickness in Fig. 41(a). The lattice parameter at low thickness begins near that of bulk Fe, increases towards the MgO surface net spacing, reaching a maximum at 10 ML, and then decreases back towards the bulk Fe value. The maximum observed average lattice parameter of 2.933 Å corresponds to a 1.9% strain with respect to bulk Fe. This is accompanied by corresponding changes in the diffraction peak width, shown in Fig. 41(b). The peak width first decreases, reaches a local minimum around 10 ML in average thickness, then increases up to 15 ML, and finally decreases for thickness up to 200 ML. Independent GISAXS [44–46] and rocking scan measurements showed that the average island size continuously increases with coverage. The peculiar variations of the $\Delta Q_{//}$ width and lattice parameter were thus analyzed as follows. The Fe initially grows as small islands that are near the bulk Fe lattice parameter. Subsequently deposited Fe causes coarsening of the islands, which are increasingly strained to the substrate lattice parameter, resulting in a lattice parameter that increases away from that of bulk Fe. Agglomeration of the islands into a continuous film occurs at about 20 monolayers of deposited Fe, and, as the film thickens beyond 10 ML, its lattice parameter decreases back toward that of bulk Fe. For low coverage, the notion of homogeneously strained small islands is adequate as a description of the peak width. As the islands become larger, the peak broadening from finite size effects becomes less important, while broadening due to inhomogeneous strain becomes more important because of dislocations entering the islands to relieve the misfit strain. Such dislocation entry is accompanied by an increase in the peak width due to the inhomogeneous strain field of the dislocation and differences in the number of dislocations present in different islands. The increase in peak width at 10 ML is thus associated with the onset of inter-island and intra-island inhomogeneous strain due to the insertion of dislocations into the islands. The subsequent decrease of the peak width above 15 ML is due to strain relaxation and grain growth that occurs in thicker films. A calculation is proposed [197] in terms of an energy balance between the cost

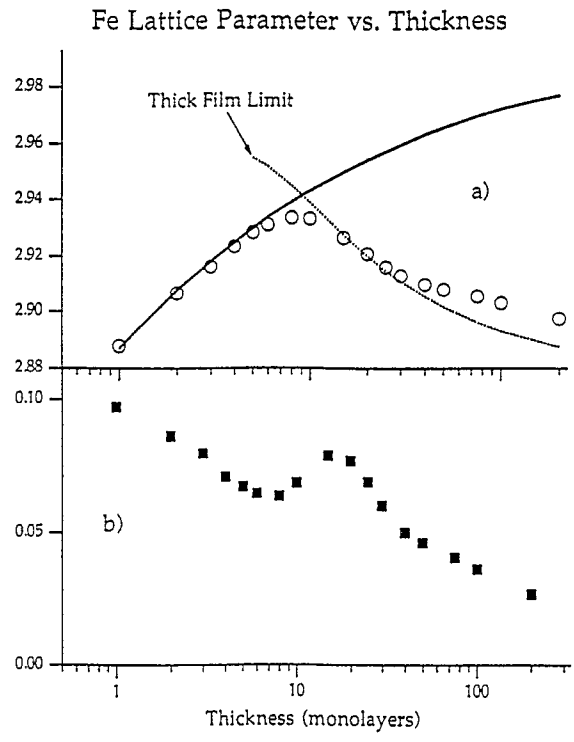

Fig. 41. (a) Fe lattice parameter (in Å) versus thickness. Around 15 ML, the islanded film is strongly strained by the substrate, while the coalesced film is largely relaxed. Solid and dashed curves are fits in the thin film and thick film regimes. (b) Fe scattering peak width (in degrees) versus thickness.

of homogeneous strain, that of inhomogeneous strain (dislocation), the Fe surface energy and the interfacial energy resulting from the atomic bonds with the substrate surface atoms.

Note that a curious feature appeared in the rocking scans for 6 and 15 ML of Fe deposited: a small peak was found on the right-hand side of the main peak, about two orders of magnitude smaller, and 4° away. This peak was interpreted as the signature for discrete rotations of the islands, in connection with dislocations present at the interface. We refer to the original paper for more details concerning theses discrete rotations.

5.2.6. *Cu/TiO_2(1 1 0) [198]*

GIXS has also been used recently to examine the effect of a Cu overlayer on the structural relaxations of the TiO_2(1 1 0)-(1 × 1) surface. This interface was chosen because, as described in Section 4.4, the structure of the clean substrate had been determined previously [116], and because Cu is known to grow epitaxially with the (1 1 1) plane parallel to the surface. A four-monolayer thick Cu(1 1 1) overlayer was deposited at room temperature. Various CTRs were measured up to out-of plane momentum transfer values of 4.8 $Å^{-1}$. Because the overlayer is known to be commensurate in one of the in-plane directions, and incommensurate in the other, it was assumed that the Cu overlayer does not contribute to the measured scattering. Note that this assumption could be discussed in view of our studies of Ag, Pd and Ni/MgO(0 0 1) interfaces, which showed that, despite the virtual absence of

relaxation of the MgO(0 0 1) surface, large effects were observed on the CTRs, and interpreted as arising from interference between the waves scattered by the substrate and those scattered by the overlayer. Since the growth of Cu on TiO_2(1 1 0) is of the Volmer–Weber type, the surface was modeled with two different surface structures, one to represent the bare substrate, with the structural parameters fixed at the values determined previously [116] and Section 4.4.1, and one to represent the covered substrate.

The Cu overlayer was found to have the effect of removing the Ti atom relaxation of the clean surface, while increasing the vertical and lateral displacements of O atoms. This was explained as arising from bonding between the Cu layer and the substrate O. The large O atom displacements give rise to a wide spread of Ti–O distances. The lateral positions of in-plane O atoms were shown consistent with some Cu atoms lying above the [1 0 0]-direction row of five-fold Ti atoms, in agreement with previous LEED and HRTEM measurements.

Recent GIXS measurements of a c-(2×2) reconstruction induced by the adsorption of K on the TiO_2(0 0 1) surface have been performed [150] but the data were not yet analyzed at the time this review was written.

5.2.7. *Comparison between the different metal/oxide interfaces*

The results presented above on the in situ studies by GIXS, during their room temperature growth, of the interfaces of different metals with a MgO(0 0 1) substrate reveal common trends as well as significant differences. Whatever the metal, Ag, Pd, Ni or Fe, the growth is three-dimensional (Volmer–Weber growth), and proceeds via the nucleation, growth, and finally coalescence of islands. This is in agreement with the expected thermodynamical equilibrium shape, since in all cases, the surface tension of the oxide surface is smaller than the sum of the surface tension of the metal and the interfacial energy between the oxide and the metal. In all four cases also, the metal/oxide system is not reactive, and hence the resulting interface is sharp. In the case of Ag, Pd and Ni, the epitaxial site was demonstrated to be above the oxygen ions of the substrate, which is in agreement with all recent theoretical calculations [158,159,161,163,183,199,200,201]. In the case of Fe, the epitaxial site was previously shown to be above oxygen ions as well, by a detailed LEED experiment. The interfacial distance was determined to be 2.34 ± 0.1 Å for a 1 ML thick Ag film, 2.52 ± 0.1 Å for a thick Ag film, and 2.216 ± 0.02 Å in the case of a 1 ML thick Pd layer. All these three values are very close to the values determined in the latest theoretical calculations [161,163,183,202], which shows that the theories are now able to correctly predict these parameters, and thus probably to correctly evaluate the interfacial energy, at least in these simple, non-reactive systems. The smallest interfacial distance in the case of Pd is certainly connected to its much larger binding energy of 0.81 eV as compared to 0.2 eV for Ag [202]. Although the interfacial distance was not obtained in the case of the Ni/MgO(0 0 1) interface, rough simulations show that it is smaller than 2 Å, which is also in agreement with the predicted distance of 1.87 Å [202].

Stacking faults and twins are found to appear very soon during the formation of the Ag/MgO(0 0 1) and Ni/MgO(0 0 1) interfaces, which is not the case of the Pd/MgO(0 0 1) interface. This may arise from the strong bonding of Pd with O ions, but also from links between the Pd clusters grown at room temperature [203].

In the case of Ag, Pd and Fe, the lattice parameter misfit is relaxed by interfacial misfit dislocations, which appear within the islands, probably near their edges, as soon as these islands reach a lateral size of the order of the coincident site lattice between the metal and the MgO substrate. In Ag and Pd, the

epitaxial relationship is cube on cube, and hence the dislocations are pure Lomer-type dislocations with $\frac{1}{2}\langle 1\,1\,0\rangle$ Burger's vectors that are parallel to the interface. The lattice parameter is small enough for them to reorder to form a network, which is the object of the next section. In the case of Fe, the Fe lattice is rotated by 45° with respect to the MgO lattice, which may be the reason why, despite the very small lattice mismatch, no ordered network of dislocation is observed. The cleanness of the substrate could also affect the ordering of dislocations. In the case of Ni, despite the strong binding energy (0.88 eV [202]) with the MgO substrate, the lattice mismatch is so large that alternative relaxation processes are preferred, like the formation of clusters of Ni(1 1 0) on the MgO(0 0 1) surface, with different in-plane orientations. Misfit dislocations may participate to this relaxation process, but if they exist, they are not ordered.

5.3. *Thick metal films on oxide surfaces: network of interfacial dislocations*

5.3.1. *Nb/α-Al_2O_3(0 0 0 1) [204,205]*

Niobium films epitaxially grown on sapphire substrates have been extensively studied as model metal–ceramic interfaces [206], and have also served as good buffer layers for the further growth of different metallic thin films [207]. Several HRTEM studies [208] had evidenced the existence of a network of misfit dislocations at the interface, relaxing the 1.9% lattice parameter misfit between Nb and sapphire. It was thus very seductive to apply the GIXS technique to this system, in order to test whether the network of interfacial misfit dislocations could be investigated with this technique. The MBE grown film, ~ 100 Å thick, had the following orientation relations in the growth directions: Nb(1 1 1)//α-Al_2O_3(0 0 0 1), with a $\sim 1.4°$ substrate miscut. X-ray measurements were carried out both in plane and out-of plane at different grazing incidence angles. The in-plane Nb orientation was found to follow the sixfold symmetry direction, with $[\bar{1}\ 1\ 0]_{Nb}//[1\ 1\ \bar{2}\ 0]_{Al_2O_3}$. Fig. 42 shows in-plane radial scans near the Nb($\bar{2}$ 2 0) peak at incidence angles varying from 0.15° to 0.6°. Three features were clearly identified: a very sharp sapphire (2 2 $\bar{4}$ 0) peak (labeled A), a broad Nb ($\bar{2}$ 2 0) peak (labeled C), the position of which is shifted toward the sapphire peak, and a satellite peak which appears at smaller $Q_{//}$ as the incidence angle is increased. As the incidence angle increases, i.e. the X-rays probe deeper toward the interface, the Nb peak becomes asymmetric. The observed lineshape suggests that a new peak (labeled B) appears at a position even closer to that of bulk sapphire. Note that the satellite peak at the low-Q side can only be seen for grazing incidence angles larger than 0.3°, which is the critical angle for total external reflection for Nb. These new structural features were therefore assumed associated with the Nb–sapphire interface, more precisely to a regular array of misfit dislocations. A simple soliton-type 2D formula was used to model the lattice deformation near the dislocation core. Only one direction parallel to the interface was modeled. Since the individual satellites were not resolved, the separation between dislocations parallel to the interface was assumed to be the calculated one, a/f, where a is the lattice spacing of the sapphire, and f is the misfit between the sapphire substrate and the strained Nb lattice spacing. The calculated 1D diffraction profile was next convoluted with the experimental width of the Nb Bragg peak of 0.03 $Å^{-1}$ FWHM, to account for the finite coherence length of the sample. Note that this experimental width is twice larger than the calculated separation between dislocation-induced satellites, of 0.0137 $Å^{-1}$. The important point is that the amplitudes of these satellites were found to be modulated by an envelope function, which is the result of lattice deformation around the dislocations. The experimental X-ray scattering profiles of the ($\bar{1}$ 1 0), ($\bar{2}$ 2 0) and ($\bar{3}$ 3 0) reflections were satisfactorily reproduced. The calculation shows that the diffuse peaks at the

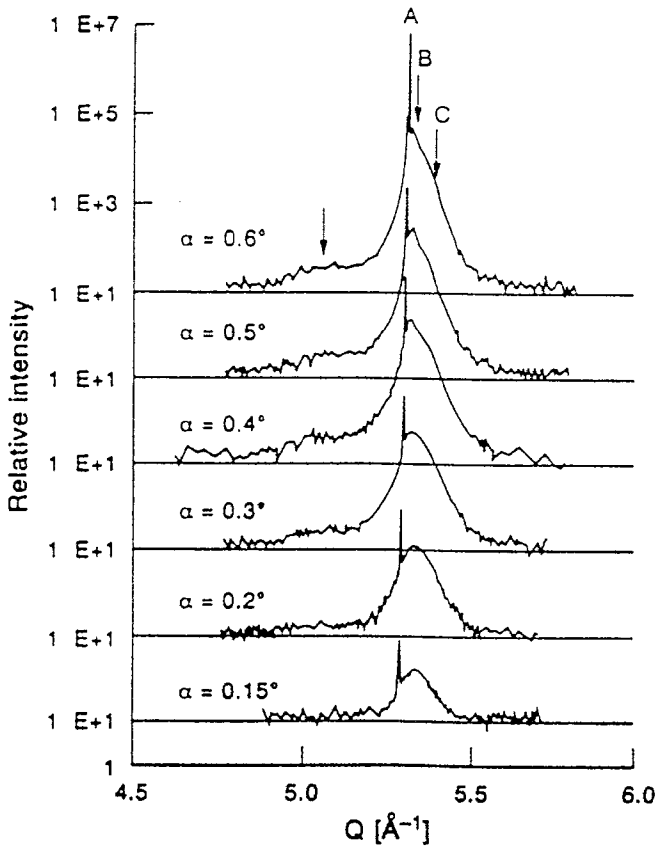

Fig. 42. In-plane radial scan around Nb(2 2 0) peak with incidence angles of X-rays varying from 0.15° to 0.6°. The Bragg peak positions of bulk Al_2O_3(2240) and Nb(2 2 0) are indicated as A and C respectively.

low-Q side of the main peaks originate from the first three Nb layers closer to the interface. In order to reproduce this shoulder, the authors had to assume that the dislocation core is located between the third and fourth layer of Nb, i.e. at a "stand-off" configuration, which is in good agreement with a previous HRTEM study of the dislocation core.

5.3.2. Ag/MgO(0 0 1) [209,210]

For the Ag/MgO(0 0 1) interface, the misfit is $f = -2.98\%$. Hence, a semi-coherent interface would be expected. Ordered, localized interfacial misfit dislocations had actually been observed by HRTEM [164]. The HRTEM conclusion was that the dislocation lines are oriented along ⟨1 0 0⟩ directions, with $a/2$ [1 0 0] Burgers vector. This could only be explained by the co-existence of two possible epitaxial sites for silver in the regions of "good match" between the Ag film and the MgO substrate: regions where the silver atoms sit above oxygen ions of the last substrate plane, and regions where they sit above magnesium ions. This conclusion was very surprising because all theoretical calculations of the epitaxial site performed so far (see Section 5.2.1) concluded to only one kind of epitaxial site, above O ions, which was also our experimental conclusion from GIXS [59]. These discrepancies motivated a GIXS investigation of the interfacial dislocation network [209,210].

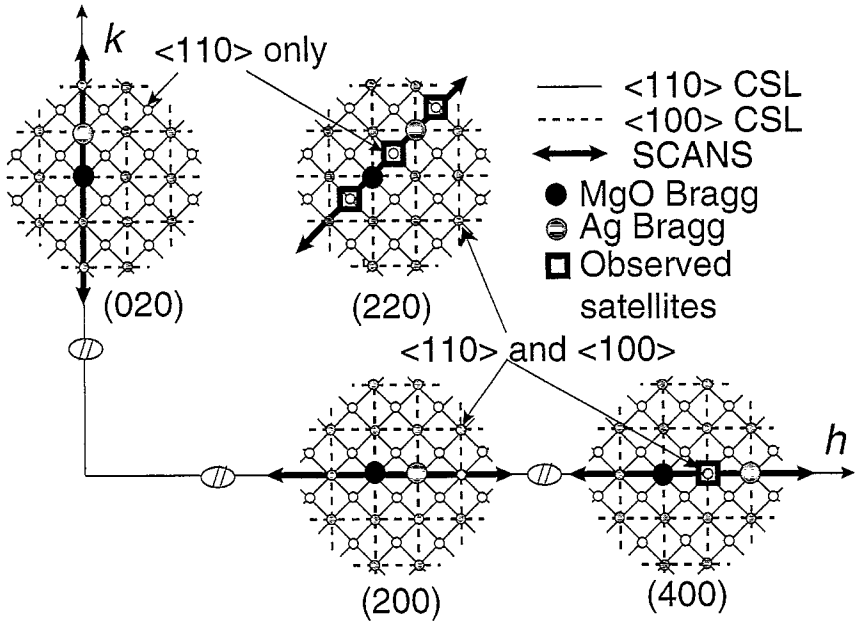

Fig. 43. Schematic representation of the (h k 0) interfacial plane of the reciprocal lattice of the Ag/MgO(0 0 1) interface with an interfacial network of misfit dislocations. The MgO and Ag Bragg peaks are, respectively, represented by large black and gray disks. The reciprocal lattices of the two possible interfacial misfit dislocation networks are also shown, as grids, with continuous lines for the ⟨1 1 0⟩ CSL, and dashed line for the ⟨1 0 0⟩ one. The locations of satellites from the interfacial network are represented as gray disks for the satellites that are common to the two CSL, and as open circles for those satellites that pertain only to the ⟨1 1 0⟩ CSL. The experimental radial scans performed on the different samples are also indicated. A scan along the (1 1 0) reciprocal direction, between the MgO and Ag Bragg peaks, should allow to distinguish unambiguously between the two possible network orientations.

According to the different possible epitaxial sites, different coincident site lattices (CSL) may be considered. In "good match" regions, because of the symmetries of the MgO(0 0 1) plane, the Ag atoms may sit either above oxygen ions of the substrate, or above magnesium ions, or in between, above the octahedral sites, with two possible variants [164]. If they sit above only one of the possible epitaxial sites, a square CSL oriented along ⟨1 1 0⟩ directions is obtained, of 97 Å periodicity. If there are two equivalent epitaxial sites, for instance O and Mg, or the two variants of the octahedral site, then a square network oriented along ⟨1 0 0⟩ directions is obtained, of 69 Å periodicity, $\sqrt{2}$ smaller than for the ⟨1 1 0⟩ CSL. As illustrated in Fig. 43, it is possible to distinguish between the ⟨1 0 0⟩ and ⟨1 1 0⟩ dislocation networks by performing X-ray scattering along the (h 0 0) and (h h 0) directions of the reciprocal space. Indeed, along the (h h 0) direction, the satellite periodicity is double in the case of a ⟨1 1 0⟩ CSL with respect to the ⟨1 0 0⟩ case.

Many different samples were studied, with different Ag thickness ranging from 50 to 1500 Å, different substrate surface preparation and different miscut of the MgO(0 0 1) substrates ranging from 0° to 3°. In all cases, as shown in Fig. 44 for a miscut substrate, and in Fig. 45 for a flat substrate, a satellite was found between the MgO(2 2 0) and Ag(2 2 0) Bragg peaks, which unambiguously demonstrates that the dislocation network is of ⟨1 1 0⟩ orientation and is sufficiently ordered to yield at least a first order satellite diffracted by this network.

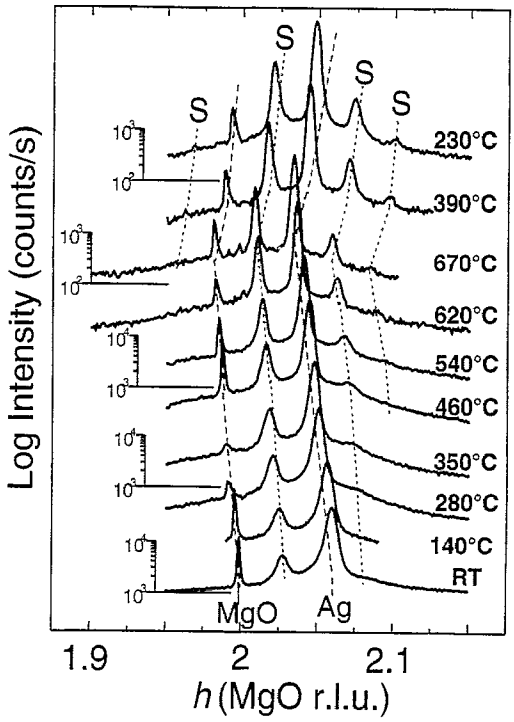

Fig. 44. Radial scans along the (h h 0.1) direction around the (2 2 0) Bragg peak at different temperatures during heating followed by cooling back to room temperature, for a 1500 Å thick Ag film grown by MBE on an MgO(0 0 1) substrate having a 2° miscut.

In addition to the orientation, many other features were deduced from these measurements. On all substrates with a significant miscut, a large background of diffuse scattering was found in the region of the Bragg peaks. It takes the form of two shoulders, symmetric with respect to the Ag peak, with a significant diffuse scattering in between. As shown in Fig. 46 on large radial scans taken at different values of the perpendicular momentum transfer l (in r.l.u. of MgO), the separation between these two peaks increases with l, in such a way that they are aligned on rods along the $(\bar{1}\,\bar{1}\,1)$ and (1 1 1) directions emanating from the Ag Bragg peak located at (2.061 2.061 0.04). These rods were shown to originate from stacking faults along (1 1 1) planes [210,211]. Another interesting feature seen in Fig. 46 is the peak measured around (2.404 2.404 0.35), which was shown to arise from twin formation, corresponding to two crystals of reverse FCC stacking, with a mirror plane at the fault location. Twins no longer produce rods, but produce additional peaks [210] at $(2\,2\,0) + \frac{1}{3}(1\,1\,1)$ and $(2\,2\,0) + \frac{2}{3}(\bar{1}\,\bar{1}\,1)$, in reciprocal lattice units of Ag.

Hence, these data showed that, in addition to the interfacial dislocation network, growth faults are present within the Ag thin film, mainly stacking faults and twins along (1 1 1) planes. These faults are likely to occur during coalescence of neighboring islands of different stacking. The density of stacking faults was found to increase with the step density of the substrate, i.e. its miscut.

In order to get further information on the interfacial dislocation network, measurements of other diffraction satellites were required. This implies samples with a better ordered dislocation network

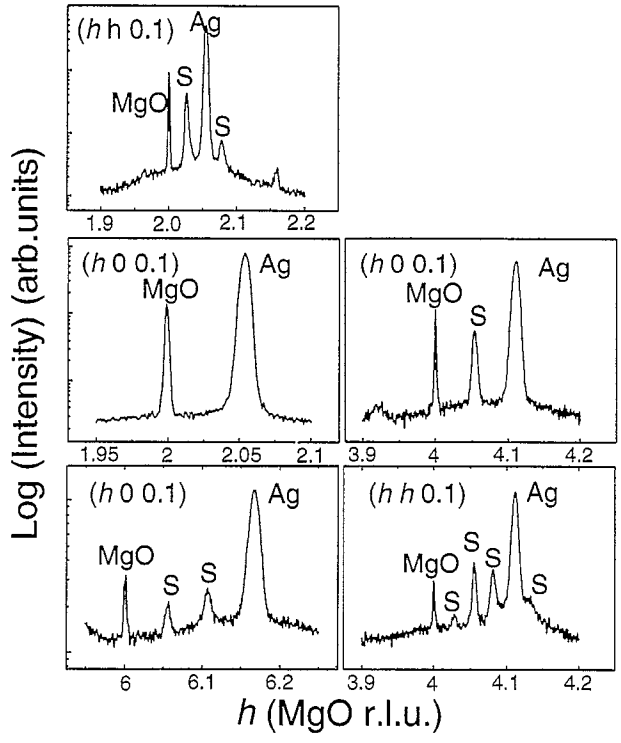

Fig. 45. Radial scans on a 1500 Å Ag film on a MgO(0 0 1) substrate with a very small residual miscut (< 0.1°), after high temperature annealing up to 770 °C. The diffraction satellites from the interfacial network of misfit dislocations are labeled by S.

yielding more satellites of larger intensity, and with as small as possible background diffuse scattering below these satellites. In order to meet these requirements, the samples were annealed at different temperatures. Because the MgO thermal expansion parameter ($13.5 \times 10^{-6}\,K^{-1}$) is smaller than the Ag one ($19.0 \times 10^{-6}\,K^{-1}$) [212], the lattice parameter misfit f decreases with increasing temperature. Hence, at equilibrium, the period of the dislocation network is expected to increase with temperature, resulting in a larger separation between dislocations. Fig. 44 illustrates the evolution of the intensity along radial scans during increasing and next decreasing annealing temperatures. During heating, all peaks shift toward smaller h values because of thermal expansion. Several features were deduced from the observed evolution. Firstly, upon annealing, the background due to the stacking faults decreases and disappears completely around 300°C. Secondly, the main satellite always remains exactly centered in between the MgO and Ag peaks, whatever the temperature. This indicates that, whatever the temperature, the period of the dislocation network changes in order for it to be exactly on the CSL. Thirdly, annealing clearly induces a re-crystallization of the Ag thin film, as revealed by a narrowing of the Ag peak in both radial and transverse directions. Transverse measurements of different orders of diffraction by the Ag film revealed that the crystalline quality is limited by a finite mosaic spread, which decreases from $\sim 0.25°$ down to $\sim 0.1°$ after annealing. At the same time the dislocation network strongly reorders, as revealed by the much larger intensity of the satellites, and by the appearance of additional satellites, both on the right of the Ag peak and on the left of the MgO one.

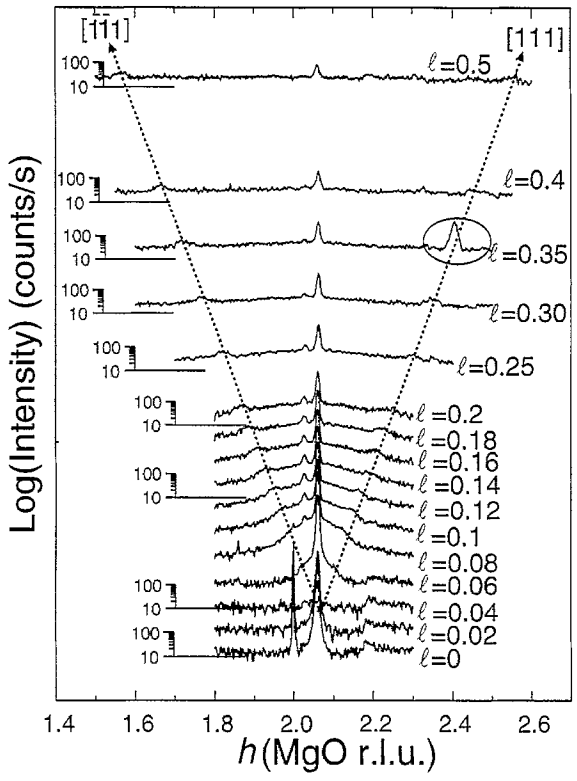

Fig. 46. Radial scans $(h\ h\ l)$ around $h = 2$ on a 1500 Å thick Ag film having a 2.5° miscut. A vertical translation, proportional to the l coordinate, has been introduced between the different scans. In addition to the MgO and the Ag CTRs and to the dislocation satellite rod, there are additional rods of scattering, oriented along the $\langle 1\ 1\ 1 \rangle$ directions, crossing the relaxed Ag peak around $l \sim 0.04$. These rods are due to stacking faults in the silver film. The peak around $h = 2.404$ and $l = 0.35$ arises from twinned Ag domains. The shift in l (0.04) of the origin of the stacking fault rods is due to refraction in the Ag film.

Around 350°C, the second satellite on the right of the Ag peak becomes clearly visible, and two other satellites appear around 620°C.

The above results demonstrate that the annealed sample is, as expected, the best suited for quantitative measurements of the dislocation satellites. For this purpose, all measurable dislocation satellites were recorded. An incidence angle of $\alpha = 2\alpha_c$ and an l-value of 0.1 were selected because they yielded the optimal satellite intensity over background ratio. Fig. 46 shows the radial measurements, which all again confirm the $\langle 1\ 1\ 0 \rangle$ orientation of the dislocation network. All in-plane peaks had a transverse FWHM of $0.1° \pm 0.02°$, thus limited by the Ag film mosaic spread. They were integrated both radially and transversely, and corrected for the active area, monitor normalization, polarization and appropriate Lorentz corrections. One important goal of this study was to quantitatively compare the experimental results with calculated intensities, in order to test the ability of the available models to calculate the main characteristics of the dislocation network, as probed by X-ray diffraction. An analytical model [213,214], developed in the framework of linear elasticity in a continuous and isotropic medium was used to compute the complete 3D displacement field, that is all atomic positions,

within a Ag(0 0 1) film of finite thickness in semi-coherent epitaxy with MgO(0 0 1). The structure factors of all main satellites were next calculated and fitted to the data with only three parameters: a scale factor common to all satellite peaks, a different scale factor for Ag Bragg peaks in order to take into account the finite thickness simulated, and a Debye–Waller factor taken identical for all atoms. The χ^2 factor was found to be very sensitive to the ratio $k = \mu_{Ag}/\mu_{MgO}$ of the respective shear moduli of the film and the substrate. The best agreement was obtained for $k = 0.28$, which yields $\chi^2 = 1.5$, close to the ideal value of 1.

This simulation showed that the substrate is effectively deformed upon epitaxy of the Ag film, and this deformation significantly contributes to the experimental data. The best agreement was found for $k = 0.28$, which is the value deduced from the bulk shear moduli. This clearly demonstrates that the theory of elasticity is well adapted to calculate the deformation field in both the substrate and the film, despite the hypothesis of elastic isotropy of both media, and is also well adapted to calculate the properties of the interface, without invoking a weaker "effective interfacial modulus". These results validate the choice of this quantitative model, and show that a numerical simulation that would be required to better describe the detailed structure of the very core of the dislocation is not necessary to reproduce these data. This actually implies that for this l value, the scattered intensity is mainly sensitive to atomic displacement far from the dislocation cores, rather than to the dislocation core itself. Further measurements of the dislocation satellites as a function of the perpendicular coordinate l would be required to determine if, for large l values, X-ray scattering could be sensitive to the atomic structure of the dislocation cores.

Additional information was gained by analyzing the residual deformation in Ag, which was found to depend upon the thickness of the film, the density of steps on the substrate and the state, as-grown or annealed, of the samples. These observations were discussed in detail [210]. In particular, the residual deformations measured on the different samples before and after annealing, were compared to the calculated deformation [214] as a function of the film thickness. Excepted for the as-grown samples on the flat substrate, the experimental residual deformations were always larger than the calculated ones. For thin films, very large and anisotropic residual deformation were found, which were explained by the fact that the 100 Å and 200 Å thick films have not yet fully coalesced. Since for 3D islands, the deformation, and thus the strain, is imposed only on the atomic plane that is in contact with the substrate, the relaxation may partly proceed on the edges. The observed non-biaxial deformation was then related to the elastic anisotropy of Ag. The decreasing difference between the residual deformation along the two kinds of directions with increasing thickness was connected to the fact that, when the film gets thicker, a smaller fraction is in the form of islands, and hence the deformation tends to be more biaxial.

For thick, continuous films, during increasing annealing temperature, the difference in lattice parameters deduced from the MgO(2 2 0.1) and Ag(2 2 0.1) peak positions was found to behave as expected according to the respective thermal expansion coefficients of Ag and MgO. By contrast, whatever the final temperature reached, the difference in lattice parameters back to room temperature was smaller after high temperature annealing than before. On miscut samples, a room temperature misfit value of $2.8 \pm 0.02\%$ was found after annealing, to compare with 2.98% before annealing. The corresponding difference in lattice parameter amounts to $2.82 \pm 0.05\%$, i.e. a residual deformation of $+0.16\%$ in silver, which is by far larger than the theoretical elastic deformation for 1500 Å thick films. On the flat sample, the residual deformation found after high temperature annealing, of $0.31 \pm 0.05\%$, was even larger.

These observations were discussed in detail [210], and were shown to prove the existence of an energetic barrier to the nucleation of misfit dislocations. A brief summary of the discussion is given hereafter. If we suppose that all the relaxation is due to the misfit edge dislocations, the dislocation density is directly related to the misfit parameter f. At 800°C, a state is reached where $f \sim 2.5\%$, which corresponds to 17% less dislocations than at RT. Since the misfit measured after cooling is larger than 2.5%, there must have been nucleation of new dislocations during cooling. Because the gliding plane is the interface plane, this introduction must proceed at the edges of islands or of the silver film. However, because the substrate steps pin the dislocations, the larger the step density, the smaller the number of dislocations that are eliminated at high temperature. The excess dislocations must stay on their terrace and should not stay pinned by the steps, since in that case, the larger the step density, the larger should be the residual deformation, which is contrary to the experimental observation. Hence, the larger the step density, the less the number of dislocations that have to be re-introduced during cooling, because steps are a reservoir of dislocations. Finally, it is found that the larger the number of dislocations that have to be reintroduced during cooling, the larger the residual deformation, which can only be explained by the existence of a barrier to the nucleation of new dislocations.

This study also provided an important information concerning the initial formation of interfacial dislocations during growth. Indeed, on all 1500 Å thick as-grown samples, the Ag film was fully relaxed. This implies that the introduction of dislocations during growth is a progressive process, probably linked with the coalescence of islands, rather than a simple nucleation followed by gliding, because in the latter case, a significant residual deformation should be observed. This deduction is in good agreement with the model for the introduction of misfit dislocations that was deduced from GIXS measurements during the in situ growth.

5.3.3. Pd/MgO(0 0 1)

It has been shown in Sections 5.2.1 and 5.2.3 that the growth and relaxation processes at the Ag/MgO(0 0 1) and Pd/MgO(0 0 1) interfaces are very much alike. This may be connected with the fact that, despite the much larger lattice parameter misfit $f = -7.6\%$ for Pd (compared to -2.98% for Ag), the bonding of Pd with MgO is stronger. Like in the Ag/MgO case, an interfacial misfit dislocation network was detected by GIXS, which is in agreement with a previous HRTEM observation of the Pd/MgO interface obtained by internal oxidation [179]. In both systems, the metal lattice parameter is smaller than that of the oxide. However, if the thermal expansion coefficient of Ag is larger than that of MgO, which results in a smaller misfit and thus a smaller dislocation density at high temperature, the opposite is true for Pd. The Pd thermal expansion coefficient ($11 \times 10^{-6}\,K^{-1}$) is smaller than that of MgO ($13.5 \times 10^{-6}\,K^{-1}$), and hence the misfit increases with temperature, corresponding to a larger density of misfit dislocations. In order to test the hypothesis of an energetic barrier to the nucleation of dislocations, it was natural to perform on this system an experiment similar to the one described in the case of Ag.

The 356 Å thick Pd film deposited in situ on the high quality MgO(0 0 1) surface (Section 5.2.3) already presented an interfacial dislocation network, but which was fairly disordered, as shown by the small intensity and large width of the main dislocation satellite. This film was thus annealed at increasing temperatures. Like in the Ag/MgO case, this resulted in a dramatic recrystallization of the Pd film and reordering of the dislocation network, as shown in Fig. 47. Before annealing, only a small and broad satellite was present between the MgO and Pd peaks, and the Pd peak was very large in the radial direction, revealing a large distribution of lattice parameters in the Pd film. Rocking scans on

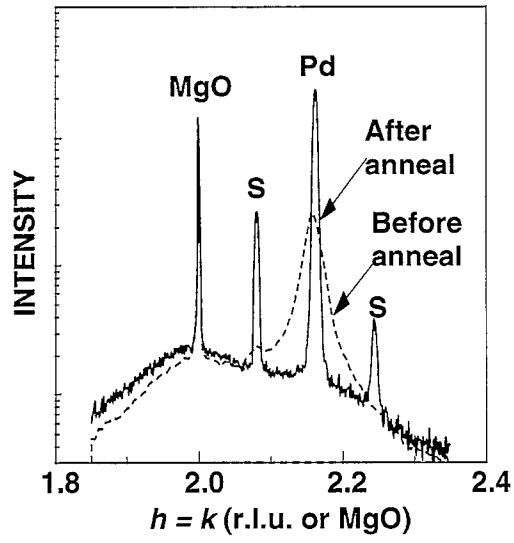

Fig. 47. Logarithm of the intensity measured during a radial scan along the (h h 0.15) direction around $h = 2$, for the as-grown 183 ML thick Pd(0 0 1) film on the MgO(0 0 1) substrate, and after 30 min annealing around 750°C. The peak at $h = 2$ corresponds to the MgO(2 2 0.15) CTR, and the peak at $h = 2.165$ is the Bragg peak of the Pd film. The peaks denoted S are satellites of diffraction by the interfacial network of misfit dislocations. This network and the Pd film are clearly much better ordered after this high temperature annealing.

different Pd peaks also showed a large in-plane mosaic spread as large as 1°. Annealing resulted in a strong increase and narrowing of the Pd peak along the radial direction, revealing a much narrower distribution of lattice parameters. A dramatic decrease of the mosaic spread, from 1° down to 0.13°, was also observed. Annealing also resulted (Fig. 47) in a strong increase and narrowing of the main satellite, and in the appearance of a very well defined and narrow second satellite on the right of the Pd Bragg peak. This phenomenon of film recrystallization together with reordering of the dislocation network is thus probably general.

Interestingly, and contrary to the Ag/MgO case, the Pd film was not fully relaxed after growth (with a peak position of $h = 2.157$), while annealing led to full relaxation ($h = 2.163$). Hence, in that case, the equilibrium density of dislocations is not obtained during the growth, but, since the misfit increases during annealing, new dislocations are introduced at the edges during heating. While most of these new dislocations were eliminated during cooling, some of them remained in order for the interface to reach its equilibrium configuration at room temperature.

5.3.4. Comparison between the different metal/MgO(0 0 1) interfaces

The above studies have shown that, for thick films that have already coalesced, the lattice parameter misfit at the Ag/MgO(0 0 1) and Pd/MgO(0 0 1) interfaces is relaxed by a regular network of dislocations. This network can be characterized in detail by GIXS, which can provide the orientation of the dislocation lines, as well as their Burger's vectors. In both cases, annealing strongly improves the crystalline quality of the film and the ordering of the dislocation network. The mosaic-spread decreases and the domain size increase. In the Fe/MgO(0 0 1) case, although misfit dislocations are present, they do not order in a network, presumably because of the different orientation and Burger's vector. In the

Ni/MgO(0 0 1) case, the misfit is too large for the relaxation to proceed via misfit dislocations alone, and clusters of other orientations are preferred. However, annealing also leads to a drastic recrystallization, and to complete disappearance of the Ni with (1 1 0) orientation, only cube on cube Ni(0 0 1)//MgO(0 0 1) is left, which demonstrate that, despite the large misfit, it is the most stable orientation relationship. Misfit dislocations are likely to be present at the interface to relax the misfit, but they are not ordered.

6. Oxide thin films characterized by grazing incidence X-ray scattering

6.1. *Superconductor thin films: structure and strain relaxation*

Since the discovery of oxide superconductors with high critical temperature, many efforts have been devoted to prepare them as thin films by different routes, and to characterize them with different techniques, including laboratory and synchrotron GIXS. Numerous papers may be found on this subject, and only representative ones will be recalled below.

One of the very first GIXS study performed on $YBa_2Cu_3O_{7-x}$ (YBCO) thin films grown on $SrTiO_3$(0 0 1) (STO) substrates [215] demonstrated the possibilities of the method. GIXS is routinely used to determine the film epitaxial relationships [216,217], as well as X-ray reflectometry, to determine the density and thickness [218], in particular for amorphous films [219]. GIXS was also used to analyze the lattice relaxation of superconductor thin films, such as in the case of YBCO on Nb-doped STO [2 2 0]. GIXS was later used to analyze ultra-thin YBCO epitaxial films grown in situ on STO and MgO(0 0 1) substrates by ozone-incorporating activated reactive evaporation [221]. Excellent quality with no interfacial disorder was revealed by the appearance of Laue oscillations. For the well lattice-matched YBCO/STO system, the crystalline quality was deteriorated due to defect introduction at the critical layer thickness (130 Å), which is the thickness above which the lattice parameter misfit is relaxed by interfacial dislocations. For the poorly lattice-matched YBCO/MgO(0 0 1) system on the other hand, excellent crystalline quality was found even above the critical thickness of 24 Å. This was explained by 3D growth below 40 Å, and by invoking an anomalous misfit relaxation mechanism. The orientation relationships were also determined by GIXS on thin YBCO films grown by laser ablation on Ag(0 0 1), Ag(1 1 0) and Ag(1 1 1) single crystals and buffer layers [222].

It is worthy to note the use of a related technique, X-ray standing waves [223], to investigate the epitaxy of YBCO on STO [224]. GIXS allowed one to show for the first time the presence of micro-twinning along the ⟨1 1 0⟩ directions in YBCO thin films prepared by laser-ablation [225] on STO substrate surfaces, with *c*-axis aligned with the (0 0 1) axis of the substrate. Such twinning was later observed and characterized in detail by GIXS in YBCO thin films prepared by metal organic chemical vapor deposition on different substrates: $YAlO_3$(0 0 1), MgO(0 0 1), $SrTiO_3$(0 0 1) and $LaAlO_3$(012) surfaces [226]. In the case of $YAlO_3$(0 0 1), a particular epitaxial relationship was found, with only one twinning direction with respect to the substrate. The [1 1 0] and [1 $\bar{1}$ 0] directions of YBCO were found aligned with the ⟨1 0 0⟩ directions of $YAlO_3$. This twinning geometry was explained by coherency strains. The surface morphology and in-plane epitaxy of thin films of $SmBaCu_3O_{7-x}$ grown on STO with various thickness have also been recently investigated in a combined STM and GIXS study [227]. Because of the smaller lattice parameter mismatches with STO (of 1.2% and −0.5% along the ***a*** and ***b***

axes respectively), SmBCO films as thick as 500 Å were found to grow pseudomorphic, in comparison with a maximum of 130 Å for YBCO (with mismatches of 2% along ***a*** and 0.7% along ***b***). A density modulation was observed in the thinnest films. For thicker films, introduction of screw dislocations was found to lead to spiral growth. A very recent GIXS study revealed a strong correlation between the miscut of vicinal STO substrates and the degree of interfacial strain and twinning in thin YBCO films grown on them [228]. Depending on the proper choice of miscut orientation and angle, one of the two twin systems could be suppressed and $\sim$ 70% untwinned growth was achieved.

6.2. Oxide films with particular magnetic or electric properties: $Dy_2BiFe_4GaO_{12}$, $BaTiO_3/Si(1\,1\,1)$, $Fe_2O_3/Si(1\,1\,1)$, $Cr_2O_3/Si(1\,1\,1)$, $Fe_2O_3(0\,0\,0\,1)/\alpha$-$Al_2O_3(0\,0\,0\,1)$, Cr_2O_3/Al_2O_3, $Cr_2O_3(0\,0\,0\,1)/Cr(1\,1\,0)$...

Some metal oxide materials have magnetic properties, which make them attractive for many applications. We may quote for instance the development of new magnetic recording media and reading heads for increased information density. The synthesis of magnetic oxide thin films is thus a field that has developed very fast in the last years, and most of the films obtained by different growth techniques were characterized by GIXS. In most cases, the film thickness was of the order of a few hundreds to a few thousands of angstroms. Again, it is not our purpose to make a complete list of the works that have been performed, but rather to give relevant examples.

Very complicated oxides have recently been investigated, such as $Dy_2BiFe_4GaO_{12}$ garnet films for magneto-optic applications [229]. The films were synthesized by pyrolysis on a glass substrate, and annealed above the glass transition temperature. The lattice parameter variation was examined as a function of depth below the surface by looking at an asymmetric Bragg diffraction peak, and varying the angle of incidence. The strain was found larger near the glass/film interface as compared to near the film surface. The stress induced during cooling, due to the thermal expansion difference between the substrate and the film, induces in turn a magnetic anisotropy. This anisotropy was found to be maximum at a critical film thickness of 600 Å. The multilayer structures of thin films of $BaTiO_3$ prepared by different routes were also examined by GIXS [230], and a growth mechanism of the film was proposed based on these data. The strain field in $BaTiO_3$ films deposited by metal-organic deposition on Si(1 1 1) substrates was studied by GIXS [231]. A substantial relaxation of the *d*-spacing of planes parallel to the surface was measured after 64 h annealing, while the *d*-spacing perpendicular to the surface remained essentially unchanged.

A combined GIXS, AFM and TEM study of Fe_2O_3 and Cr_2O_3 thin films ($\sim$ 1 000 Å thickness) deposited on silicon wafers is described in [232]. X-ray reflectivity was used to estimate the changes in density of the films, and GIXS to determine the orientational relationships. GIXS was also used to follow the ion beam mixing effect at the Fe_2O_3/α-Al_2O_3 interface, the $\sim$ 500 Å thick Fe_2O_3 layers being deposited by pulsed laser ablation [233]. Sub-stoichiometric phases were evidenced.

GIXS was combined with XPS to characterize thin oxide films formed by heating at 873 K in air FeCr alloys with different concentrations [234]. The main crystallographic structure of the oxide film was found corundum type structures of Fe_2O_3 and Cr_2O_3, although it depends on the bulk chromium concentration.

The oxidation of Cr(1 1 0) surfaces is of fundamental as well as applied interest for effective surface protection [235]. In addition, thin oxide films of Cr(1 1 0) have recently proven as model systems for the study of heterogeneous catalytic reactions at solid state surfaces [236]. The oxidation of Cr(1 1 0)

surfaces has thus been studied by many techniques. However, open questions were left regarding the exact oxide film thickness, the oxide growth laws and the relation of the oxide microstructure to the oxidation behavior. The oxidation process was thus characterized by GIXS [237–240] as a function of temperature, oxygen exposure and time. The single crystal Cr(1 1 0) films were prepared by MBE on a Nb(1 1 0)/Al_2O_3(1 1 $\bar{2}$ 0) buffer system, with thickness ranging from 100 to 1000 Å. Oxidation was performed with typical oxygen partial pressure of 5×10^{-5} mbar, in the temperature range from 400 to 800 K. X-ray reflectivity was performed in situ to deduce the thickness of the growing oxide layer, its defect density and the roughness of the oxide surface and the metal/oxide interface for different times and temperatures. Below 725 K, the oxidation was found to proceed by a layer-by-layer growth without roughening of the metal/oxide interface. Fairly thin (a few 10 Å) oxide layers were obtained, with a density smaller than that of bulk Cr_2O_3. The oxide film thickness in quasi-equilibrium was found to increase linearly with temperature, and the oxide surface and metal/oxide interface remained smooth on the order of 2–4 Å. After a rapid decrease of the oxide thickness in the early growth stage, saturation of the thickness was observed. It was found to depend markedly on the oxidation temperature, indicative of an oxidation process that is controlled by the Cr-ion diffusion. The activation energy for the cation diffusion was determined to be 1.4 eV, which is a factor of 2 smaller than that for bulk interstitial diffusion. Above 725 K, the oxide surface was found to roughen, and cavities were found to form at the metal/oxide interface. The transition from layer-by-layer to 3D island-like growth mode was explained in terms of epitaxial growth models. In-plane and out-of plane GIXS measurements allowed the identification of the oxide structure as orthorhombic α-Cr_2O_3 with the (0 0 0 1) axis parallel to the Cr(1 1 0) axis, Cr_2O_3[1 1 $\bar{2}$ 0]//Cr[1 $\bar{1}$ 0] and Cr_2O_3[1 $\bar{1}$ 0 0]//Cr[0 0 1], and with sixfold symmetry. Good epitaxy occurs in the Cr[0 0 1] direction because the misfit is less than 0.5%. Annealing in UHV at higher temperature (850 K) was found to significantly improve the oxide crystalline quality, with a decrease of the mosaic distribution from 5.1° to 3.7°. The same group also investigated the thermal oxidation of a 13 Å thick (1 1 0)-oriented Fe film grown epitaxially on Cr(1 1 0) [241], by X-ray reflectivity, GIXS and AES measurements. The final oxide layer was larger than expected when only the Fe layer had been oxidized. Indeed, an additional Cr_2O_3(0 0 0 1) layer was found to form on top of the Fe-oxide layer, providing evidence that the Cr-ion is the diffusing species during oxidation. A 22 Å thick Cr layer grown of top of the Fe(1 1 0) one was found to transform into a 46 Å thick Cr_2O_3(0 0 0 1) film protecting the Fe layer against oxidation, thus showing that Fe-ion diffusion through the Cr-oxide layer is more difficult than through the Fe-oxide layer because of the smaller defect density in the former.

The same group also has recent GIXS and reflectivity data on the oxidation of Ni(1 1 1) films [242] but the results are not yet published. A recent investigation of the oxidation of the NiAl(1 0 0) surface has also been undergone at the ESRF [242]. The formation of a 20 Å thick θ-Al_2O_3 overlayer with a 2×1 superstructure was observed. The substrate atoms near the interface also show a 2×1 modulation. The detailed structure of the interface is under investigation.

6.3. *Others: PbO, SnO_2, MgO layers, oxides on stainless steel, TiO_xN_y, CeO_2*

PbO is a potential solid lubricant for use at high temperature in oxidizing environments. GIXS was combined with XPS and Raman spectroscopy to investigate the chemistry and structure of PbO layers deposited by pulsed laser deposition for varying substrate temperatures and oxygen partial pressures [243]. Films deposited at room temperature were found to retain the crystal structure, but to be oxygen

deficient. Increasing temperature and O_2 partial pressure led to increased O/Pb ratio, and changes in the structure and orientation.

SnO_2, which has the rutile structure, is an important metal-oxide from the point of view of applications, as it is used as a gas sensor. GIXS and XPS were again combined to probe the growth mechanism of sprayed SnO_2 films deposited with different Sn concentrations in the precursor solution [244]. As the Sn concentration was increased, the preferred growth changed from the (1 1 0) to the (2 0 0) direction.

It has been known for a long time that nearly perfectly stoichiometric MgO thin layers can be prepared by electron-beam evaporation or r.f. sputtering of a MgO target. High quality epitaxial MgO thin films have recently been prepared by electron bombardment on Fe(0 0 1) surfaces, themselves prepared by MBE deposition of Fe on MgO(0 0 1) substrates [245]. MgO(0 0 1) was observed to grow epitaxially on Fe(0 0 1), with a 45° rotation between the respective unit cell axes. The growth was characterized in situ by different techniques and ex situ by HRTEM and laboratory GIXS. The degree of relaxation of the MgO layer was determined as a function of thickness, and compared with that expected by a model of the interfacial dislocations. GIXS and X-ray reflectometry were also used to characterize 0.1, 0.5 and 1 μm thick MgO layers deposited on different alumina and glass substrates with different substrate temperatures and oxygen partial pressures [246]. The films were found polycrystalline with different ⟨1 0 0⟩ textures depending on the substrate temperature, while the oxygen partial pressure did not influence the film structure. The profiles of MgO Bragg reflections were found to be influenced by the substrate roughness.

GIXS has also been used to characterize Cr_2O_3 and $FeCr_2O_4$ oxide films formed by thermal oxidation of stainless steel [247], and to study the effects of yttrium implantation on the initial stages of thermal oxidation of Ni–20Cr alloys [248]. Note also a determination of residual stress in sapphire implanted with Cr^+ ions, by measurements of both in-plane and out-of-plane diffraction peaks positions and profiles [249]. Let us cite also the combined use of TEM and GIXS for the characterization of the microstructure of epitaxial $La_{0.5}Sr_{0.5}CoO_3/Pb_{0.9}La_{0.1}(Zr_{0.2}Ti_{0.8})_{0.975}O_3/La_{0.5}Sr_{0.5}CoO_3$ hetero-structures on $LaAlO_3$, with particular ferroelectric properties [250], or the use of GIXS to study the interfacial properties of a thin Cu layer deposited on SiO_2, and mixed with 80 keV Ar^+ at different temperatures [251].

The crystallographic structure of thin (28–110 nm) TiO_xN_y coatings elaborated by dual ion beam sputtering was also characterized by GIXS [252]. The incorporation of oxygen was observed to greatly improve the adhesion of the films on the glass substrate. In the range of up to 14% of the oxygen to nitrogen flux ratio, an FCC TiN phase was observed, with (1 1 1) texture. Amorphous-like films were found for higher oxygen concentrations.

GIXS was used in an energy dispersive mode to analyze the structure of CeO_2 overlayers deposited on the (0 0 1) surface of cubic yttrium stabilized zirconia [253]. The CeO_2 layers were shown to form epitaxial islands with 5–15 monolayers in thickness with a nearly relaxed lattice constant. The discussion was mainly oriented toward the new possibilities offered by energy dispersive GIXS.

6.4. X-ray magnetic scattering by the UO_2(0 0 1) surface

Although this is clearly out of the scope of this review, we have to mention the use of the grazing incidence geometry to characterize magnetic surfaces by magnetic X-ray scattering. The first study of this kind was indeed performed on an oxide surface: the (0 0 1) surface of UO_2 [254,255]. The

resonance of the magnetic scattering cross-section at the M_{IV} edge of uranium was used to get enhanced magnetic scattering at and below the bulk Néel temperature T_N. Scattering associated with the (01l) magnetic truncation rod was measured as a function of the photon energy around the edge, and observed to vanish at T_N on heating. The characteristic Vineyard profile of the intensity as the angle of incidence was swept through the critical angle was observed for the first time for magnetic scattering.

7. Conclusions and future outlook

The aim of this review was to give examples of the information that has been gained so far by use of the GIXS technique on oxide surfaces and metal/oxide interfaces. This technique is now well established and many dedicated UHV surface diffractometers of high accuracy are available to perform the experiments. This review was mostly restricted to in situ studies, which explains why X-ray investigations of metal/oxide multilayers, which are mostly performed ex situ using X-ray reflectivity, were not included. The strengths and the many possibilities of GIXS have been shown in details and thus will not be recalled here. It is important to point out that the GIXS technique also has limitations. One limitation is the need for single crystals and surfaces of very high quality, which are often difficult to obtain. Polycrystalline or structurally complicated samples are very difficult to study. However, the use of the very intense X-ray beam of third generation synchrotron sources like the ESRF should allow investigating buried interfaces obtained by internal oxidation for instance. A complete characterization of the growth mode by GIXS alone is often difficult, and complementary measurements such as AES, XPS or low energy ion scattering (LEIS) [256] are necessary. GIXS also often requires synchrotron radiation, which means that a limited amount of time is devoted to a particular study, so that all pertinent parameters (such as for instance a substrate temperature or defect density) cannot be systematically varied, which requires laboratory experiments and thus other techniques. When studying the growth conditions of an epilayer in heteroepitaxy, other in situ tools such as the RHEED technique, especially when it is combined with image acquisition on a computer or tape, can provide information on the surface relaxation and morphology in real time, and can thus be used to monitor the growth. They are often a good and cheap alternative to GIXS measurements. However, they are limited to the few top atomic layers, they suffer from charging effects on insulating substrates, and are very difficult to analyze quantitatively because of multiple scattering of the electrons.

It is now a widely accepted idea that research in material science will resort more and more to numerical simulations in the future, in order to propose new materials with specific properties [11,257]. This implies the development of very accurate theories. These theories are still under development in the case of oxide surfaces and metal/oxide interfaces. In order to test their adequacy, precise experimental results on the structure and morphology of these systems are required. In this framework, most experimental studies presented in this review were performed on model oxide surfaces and metal/oxide interfaces.

The determination by GIXS of the atomic structure of several model oxide surfaces that are either relaxed or reconstructed was described. In all cases, these surfaces are not only model surfaces for theoretical calculations, but also have important applications, mostly as substrates for the growth of overlayers of technological interest, such as superconductors with a high critical temperature.

The relaxation and rumpling at the MgO(0 0 1) surface, which are both very small, were determined with the highest accuracy achieved so far, and shown to compare very well to the latest theoretical

calculations. The termination and the large relaxations of the sapphire unreconstructed α-$Al_2O_3(0\,0\,0\,1)$ surface were determined with a high accuracy, and were again shown to be well predicted by the latest computer predictions. Complicated reconstructions obtained by in situ reduction of this surface in UHV were also investigated, and structural models were proposed, that could not have been inferred from electron diffraction measurements because of multiple scattering effects and of the insulating nature of the surface. GIXS studies of the relaxation of the unreconstructed $TiO_2(1\,1\,0)$ surface and reconstructed $TiO_2(1\,0\,0)$-(1×3) surface were described, and again compared with theoretical calculations. Recent experiments on the antiferromagnetic $NiO(1\,1\,1)$ surface were also reviewed, and this surface, thought for a long time to be unstable, was shown to be stabilized either by adsorption of gases, or by a $p(2 \times 2)$ reconstruction, whose structure still has to be refined. Recent GIXS experiments on other important oxide surfaces such as $SrTiO_3(0\,0\,1)$ and $Cr_2O_3(0\,0\,0\,1)$ were reported.

Most of the interactions at metal/oxide interfaces depend on the adsorption site of the metal, and vary rapidly with the interfacial distance between the last plane of the oxide surface, and the first atomic plane in the metallic overlayer. Providing experimental values of this adsorption site and interfacial distance is thus crucial to test the different theoretical representation of the metal/oxide interaction. These parameters are very difficult to determine accurately with most techniques. They were determined with GIXS in several metal/oxide systems, mainly the metal/$MgO(0\,0\,1)$ interfaces, the metal being Ag, Pd, Ni or Fe. In these systems, the latest theories were again found to yield a correct prediction of these parameters.

Overall, these different results show that the available theories are sufficiently well developed for these simple, non-reactive metal/oxide systems. The way is thus opened to simulate, and of course experimentally investigate systems that are more complex.

In addition to these purely structural studies, GIXS was shown to provide a lot of information on the structure and morphology of metal/oxide interfaces during their growth from the very beginning to fairly thick deposits, or during subsequent annealing resulting in reordering of the metallic epilayer. The evolution during growth of the mosaic spread, average domain size, average lattice parameter and lattice parameter distribution can be followed. The introduction of stacking faults, twins and dislocations can be detected, as well as the onset of coalescence. When the lattice parameter mismatch is not too large, it may be plastically relaxed in thick enough films by a network of interfacial misfit dislocations. Detailed characterization of this network by GIXS was described, and shown very useful in the case of weakly bound interfaces like Ag/$MgO(0\,0\,1)$, for which HRTEM investigations may be very difficult. The evolution of this network of misfit dislocations with the lattice parameter mismatch, which is itself varied by using the different thermal expansion between the metal and the oxide substrate, was also followed, and used to deduce qualitative arguments on the nucleation of misfit dislocations.

Many examples also showed that GIXS is now a routine technique used to examine the structure of oxide thin films, their epitaxial relationship to the substrate and the relaxation of the elastic strains.

Some of the results presented could prove to be useful in technological applications, especially when the detailed structure of the substrate may change the properties of layers that are grown on it. This is the case for instance of the α-$Al_2O_3(0\,0\,0\,1)$ surface which is a substrate of choice for the growth of new large gap III–V materials such as $Al_xGa_yIn_zN$ in which the defect type and density have already been shown to depend on the previous surface treatment [258]. The preparation of $MgO(0\,0\,1)$ or $SrTiO_3(0\,0\,1)$ substrates of high quality may also be technologically important, for instance because they influence the structure of epitaxial high T_c oxide thin films.

Only a very small number of oxide surfaces and metal/oxide interfaces have been investigated so far by GIXS. However, the number of studies is expected to increase steadily, since more and more teams are involved in this field. Many experiments have just been performed and are in the analysis process (on the CoO(1 1 1) surface, on the $SrTiO_3$(0 0 1) reconstructed [148] or unreconstructed [144] surface, on the Cr_2O_3(0 0 0 1) and K/TiO_2(0 0 1)-c(2 × 2) surfaces [150], the oxidation of Ni(1 1 1) and NiAl(1 1 0) surfaces [242]), or are going to be performed in the near future on the ZnO(0 0 0 1)–O and –Zn and NiO(0 0 1) surfaces [259], and Fe_3O_4(0 0 1) and (1 1 1) single-crystal or thin-film surfaces [150,260] as well as on other surfaces and interfaces of particular interest.

This field is expected to grow very fast in the coming years, and exciting studies still have to be attempted in different directions. The investigation of the reactivity of the surface oxide ions, and the adsorption of different gaseous species on oxide surfaces is expected to develop. Investigations of stepped oxide surfaces and the effect of the miscut of vicinal substrates on the structure of the overlayer still have to be done, as well as the in situ investigation of reactive metal/oxide interfaces or of the metal oxidation process. The use of surfactant species, either gaseous, liquid or solid, to promote wetting at metal/oxide interfaces is still in its infancy, and a lot is expected in this field. More and more research is devoted to the growth of oxide thin films of high quality. GIXS has been demonstrated on metal surfaces to be a very powerful probe of the growth mode during homoepitaxy, and will almost certainly be used to investigate the homoepitaxial or heteroepitaxial growth of oxides on different substrates, metal, semiconductors or ceramics. The advent of highly intense X-ray sources also makes possible micro-GIXS studies with lateral resolution by scanning the incident X-ray beam or the in situ investigation of fast kinetic processes involved at interfaces. Finally, note that GIXS is one of the very rare surface probes that do not require a UHV environment. Investigation of the growth by different liquid or vapor phase epitaxy techniques is foreseen in the near future, together with investigation of surfaces under gaseous pressure between UHV and high pressure and of oxide/liquid interfaces, reactive or not.

Acknowledgements

I first would like to thank my colleagues B. Villette, P. Guénard, A. Barbier, O. Robach, who were all strongly involved in the work from our team described here. I would like to acknowledge T.E. Madey, A. Barbier, M. Belakhovsky, M. Gautier-Soyer and A. Stierle for critical reading of the manuscript. I also would like to thank G. Thornton, W. Moritz, S. Ferrer, J. Zegenhagen and A. Stierle for providing unpublished results and allowing use of their figures, published or not. I am greatly indebted to Professor T. Madey for having invited me to write this review.

References

[1] V.E. Henrich, P.A. Cox, The Surface Science of Metal Oxides, Cambridge University Press, Cambridge, UK, 1994.
[2] V.E. Henrich, The surfaces of metal oxides, Rep. Prog. Phys. 48 (1985) 1481.
[3] C. Noguéra, Physics and Chemistry at Oxide Surfaces, Cambridge University Press, Cambridge, UK, 1996.
[4] J. Nowotny, Louis-Claude Dufour, Surface and Near-surface Chemistry of Oxide Materials, Elsevier, Amsterdam, 1988.
[5] E.A. Colbourn, Surf. Sci. Rep. 15 (1992) 281.

[6] M. Rühle, A.G. Evans, M.F. Ashby, J.P. Hirth (Eds.), Metal–Ceramic Interfaces, Acta-Scripta Metall. Proc. vol. 4 Pergamon Press, Oxford, 1990.
[7] Proceedings of the International Symposium on Metal–Ceramic Interfaces Acta Metall. Mater. S40 (1992).
[8] J. Nowotny, Science of Ceramic Interfaces, Elsevier, Amsterdam, The Netherlands, 1991.
[9] H. Bialas, K. Heneka, Vacuum 45 (1994) 79.
[10] F. Reniers, M.P. Delplancke, A. Asskali, V. Rooryck, O.Van Sinay, Appl. Surf. Sci. 92 (1996) 35.
[11] G. Pacchioni, in: R.U. Lambert, G. Pacchioni (Eds.), Chemisorption and Reactivity on Supported Clusters and Thin Films, Kluwer Academic Publishers, Dordrecht, 1997, p. 395.
[12] M.W. Finnis, Acta Metall. Mater. 40 (1992) S25.
[13] A.M. Stoneham, P.W. Tasker, J. Phys. C18 (1985) L543.
[14] J.R. Smith, T. Hong, D.J. Srolovitz, Phys. Rev. Lett. 72 (1994) 4021.
[15] U. Schönberger, O.K. Andersen, M. Methfessel, Acta Metall. Mater. 40 (1992) S1.
[16] P. Blöchl et al., in: M. Rühle, A.G. Evans, M.F. Ashby, J.P. Hirth (Eds.), Metal–Ceramic Interfaces, Pergamon Press, Oxford, 1990.
[17] D.M. Duffy, J.H. Harding, A.M. Stoneham, Acta Metall. Mater. 40 (1992) S11.
[18] L. Spiess, Surf. Rev. Lett. 3 (1996) 1365.
[19] P.W. Tasker, Adv. Ceram. 10 (1984) 176.
[20] C.T. Campbell, Surf. Sci. Rep. 27 (1997) 1.
[21] W.C. Marra, P. Eisenberger, A.Y. Cho, J. Appl. Phys. 50 (1979) 6927; P. Eisenberger, W.C. Marra, Phys. Rev. Lett. 46 (1981) 1081.
[22] R. Feidenhans'l, Surf. Sci. Rep. 10 (1989) 105.
[23] I.K. Robinson, D.J. Tweet, Rep. Prog. Phys. 55 (1992) 599.
[24] P.H. Fuoss, S. Brennan, Annu. Rev. Mater. Sci. 20 (1990) 365.
[25] I.K. Robinson, in: by G.S. Brown, D.E. Moncton (Eds.), Handbook on Synchrotron Radiation, vol. 3, Elsevier, Amsterdam, Oxford, 1991, pp. 221.
[26] H. Dosch, Springer Tracts in Mod. Phys. 1992, Springer, Berlin, p. 126.
[27] S. Dietrich, A. Haase, Phys. Rep. 260 (1995) 1.
[28] E. Vlieg, I.K Robinson, in: P. Coppens (Ed.), Synchrotron Radiation Crystallography, Academic Press, London, 1992.
[29] H. Chen, Mat. Chem. Phys. 43 (1996) 116.
[30] P.H. Fuoss, K.S. Liang, P. Eisenberger, in: R.E. Bachrach (Ed.), Synchrotron Radiation Reserach: Advances in Surface Science, Plenum, New York, 1989.
[31] J.D. Jackson, Classical Electrodynamics, Wiley, New York; or M. Born, E. Wolf, Principles of Optics, 5th ed., Pergamon, New York.
[32] B.E. Warren, X-Ray Diffraction, Addison-Wesley, Reading, MA, 1969; or R.W. James, The Optical Principles of the Diffraction of X-Rays, Ox Bow, Connecticut, 1982.
[33] S.R. Andrews, R.A. Cowley, J. Phys. C 18 (1985) 6247.
[34] I.K. Robinson, Phys. Rev. B 33 (1986) 3830.
[35] T. Harada, M. Asano, Y. Mizumati, J. Cryst. Growth 116 (1992) 243.
[36] E. Vlieg, J. Appl. Cryst., in press.
[37] C. Schamper, H.L. Meyerheim, W. Moritz, J. Appl. Cryst. 26 (1993) 687.
[38] M.F. Toney, D.G. Wiesler, Acta Cryst. A 49 (1993) 624.
[39] P. Guénard, Ph.D. Thesis, University of Grenoble, 1996.
[40] O. Robach, Ph.D. Thesis, University of Grenoble, 1997.
[41] M.B. Véron, Ph.D. Thesis, University of Paris-VI, 1996.
[42] E.D. Specht, F.J. Walker, J. Appl. Cryst. 26 (1993) 166.
[43] M.F.C. Laad, R.A. Palmer, Structure Determination by X-Ray Crystallography, Plenum Press, New York, 1978.
[44] J.R. Levine, J.B. Cohen, Y.W. Chung, P. Georgopoulos, J. Appl. Cryst. 22 (1989) 528.
[45] D. Thiaudière, Thesis, University of Poitiers, 1996.
[46] J.R. Levine, Ph.D. Thesis, Northwestern University, 1990.
[47] S. Brennan, P. Eisenberger, Nucl. Instr. Meth. 222 (1984) 164.
[48] K. Akimoto, J. Mizuki, I. Hirosawa, J. Matsui, Rev. Sci. Instr. 60 (1989) 2362.
[49] E. Vlieg, A. Van't Ent, A.P. de Jongh, H. Neerings, J.F. Van der Veen, Nucl. Instr. Meth. A 262 (1987) 522.

[50] P. Claverie, J. Massies, R. Pinchaux, M. Sauvage-Simkin, J. Frouin, J. Bonnet, N. Jedrecy, Rev. Sci. Instr. 60 (1989) 2369.
[51] P.H. Fuoss, I.K. Robinson, Nucl. Instr. Meth. 222 (1984) 171.
[52] S. Ferrer, F. Comin, Rev. Sci. Instr. 66 (1995) 1674.
[53] G. Renaud, B. Villette, P. Guénard, Nucl. Instr. Meth. B 95 (1995) 422.
[54] ESRF Beamline Handbook on http://www.esrf.fr and Ref. [53].
[55] ESRF Beamline Handbook on http://www.esrf.fr and R. Baudoing-Savois, M. De Santis, M.C. Saint-Lager, P. Dolle, O. Geaymond, P. Taunier P. Jeantet, J.P. Roux, G. Renaud, A. Barbier, O. Robach, O. Ulrich, A. Mougin, G. Bérard, A new UHV diffractometer for surface structure and real time molecular beam deposition studies with Synchrotron radiations at ESRF, to be published.
[56] O. Robach, G. Renaud, A. Barbier, Surf. Sci. 401 (1998) 227.
[57] Y.C. Lee, P. Tong, P.A. Montano, Surf. Sci. 181 (1987) 559.
[58] C. Li, R. Wu, A.J. Freeman, C.L. Fu, Phys. Rev. B 48 (1993) 8317.
[59] P. Guénard, G. Renaud, B. Villette, Physica B 221 (1996) 205.
[60] G. Bordier, C. Noguera, Phys. Rev. B 44 (1991) 6361.
[61] J. Goniakowski, C. Noguera, Surf. Sci. 323 (1995) 129.
[62] A.J. Martin, H. Bilz, Phys. Rev. B 19 (1979) 6593.
[63] F.W. de Wette, W. Kress, U. Schröder, Phys. Rev. B 32 (1985) 4143.
[64] P.W. Tasker, D.M. Duffy, Surf. Sci. 137 (1984) 91.
[65] M. Causa, R. Dovesi, C. Pisani, C. Roetti, Surf. Sci. 175 (1986) 551.
[66] G. Pacchioni, T. Mierva, P.S. Bagus, Surf. Sci. 275 (1992) 450.
[67] G.V. Lewis, C.R.A Catlow, J. Phys. C 18 (1985) 1149.
[68] J.P. LaFemina, C.B. Duke, J. Vac. Sci. Technol. A 9 (1991) 1847.
[69] C.G. Kinniburgh, J. Phys. C: Solid State Phys. 9 (1976) 2695.
[70] T. Urano, T. Kanaji, Surf. Sci. 134 (1983) 109.
[71] M.R. Welton-Cook, W. Berndt, J. Phys. C: Solid State Phys. 15 (1982) 5691.
[72] M. Prutton, J.A. Walker, M.R. Welton-Cook, R.C. Felton, J.A. Ramsey, Surf. Sci. 89 (1979) 95.
[73] H. Nakamatsu, A. Sudo, S. Kawai, Surf. Sci. 194 (1988) 265.
[74] P.A. Maksym, Surf. Sci. 149 (1985) 157.
[75] A. Santoni, D.B. Tran Thoai, J. Urban, Solid State Commun. 68 (1988) 1039.
[76] K.H. Rieder, Surf. Sci. 188 (1982) 57.
[77] D.L. Blanchard, D.L. Lessor, J.P. LaFemina, D.R. Baer, W.K. Ford, T. Guo, J. Vac. Sci. Technol. A 9 (1991) 1814.
[78] J.B. Zhou, H.C. Lu, T. Gustafsson, P. Häberle, Surf. Sci. 302 (1994) 350.
[79] M. Stoneham, P.W. Tasker, J. Phys. C 18 (1985) L543.
[80] P. Wynblatt, R.C. Mc Cune, in: J. Nowotny, L.-C. Dufour (Eds.), Surface and Near-Surface Chemistry of Oxide Materials, Elsevier, Amsterdam, 1988, p. 247.
[81] A.J. Burggraf, A.J. Winnubst, in: J. Nowotny, L.-C. Dufour (Eds.), Surface and Near-Surface Chemistry of Oxide Materials, Elsevier, Amsterdam, p. 449.
[82] P. Masri, P.W. Tasker, J.P. Hoare, J.H. Harding, Surf. Sci. 173 (1986) 439.
[83] P. Masri, P.W. Tasker, Surf. Sci. 149 (1985) 209.
[84] A.M. Stoneham, P.W. Tasker, in: J. Nowotny, L.C. Dufour, (Eds.), Surface and Near-Surface Chemistry of Oxide Materials, Elsevier, Amsterdam, 1988, p. 1.
[85] Z.L. Wang, J. Bentley, E.A. Kenik, L.L. Horton, R.A. McKee, Surf. Sci. 273 (1992) 88.
[86] R. Souda, T. Aizama, Y. Ishiszawa, C. Oshima, J. Vac. Sci. Technol. A 8 (1990) 3218.
[87] P.A. Crozier, M. Gadjardziska-Josifovska, J.M. Cowley, Microsc. Res. Tech. 20 (1992) 426.
[88] P.A. Crozier, M. Gajdardiziska-Josifovska, Ultramicroscopy 48 (1993) 63.
[89] M. Gajdardziska-Josifovska, P.A. Crozier, M.R. McCartney, Surf. Sci. 284 (1993) 186.
[90] V.E. Henrich, G. Dresselhaus, H.J. Zeiger, Phys. Rev. B 22 (1980) 4764.
[91] C. Duriez, C. Chapon, C.R. Henry, J.M. Rickard, Surf. Sci. 230 (1990) 123.
[92] International Table of X-Ray Crystallography, vol. III, Kynoch Press, Birmingham, UK, 1962, p. 232.
[93] T. Gotoh, S. Murakami, K. Kinosita, Y. Murata, J. Phys. Soc. Jpn. 50 (1981) 2063.
[94] P. Guénard, G . Renaud, A. Barbier, M. Gautier-Soyer, Mater. Res. Soc. Symp. Proc. 437 (1996) 15.

[95] P. Guénard, G. Renaud, A. Barbier, M. Gautier-Soyer, Surf. Rev. Lett. 5 (1998) 321.
[96] M. Gautier, J.P. Duraud, L. Pham Van, Surf. Sci. 249 (1991) L327.
[97] J. Guo, D.E. Ellis, D.J. Lam, Phys. Rev. B 45 (1992) 13647.
[98] W.C. Mackrodt, R.J. Davey, S.N. Black, R. Docherty, J. Cryst. Growth 80 (1987) 441.
[99] I. Manassidis, M.J. Gillan, J. Am. Ceram. Soc. 77 (1994) 335; Surf. Sci. 285 (1993) L517.
[100] M. Causá, R. Dovesi, C. Pisani, C. Roetti, Surf. Sci. 215 (1989) 259.
[101] T.J. Godin, J.P. LaFemina, Phys. Rev. B 49 (1994) 7691.
[102] A. Kirfel, K. Eichhorn, Acta Cryst. A 46 (1990) 271.
[103] G.C. Ndubuisi, J. Liu, J.M. Cowley, Microsc. Res. Tech. 20 (1992) 439.
[104] V.E. Puchin, J.D. Gale, A.L. Shluger, E.A. Kotomin, J. Günster, M. Brause, V. Kempter, Surf. Sci. 370 (1997) 190.
[105] J. Ahn, J.W. Rabalais, Surf. Sci. 388 (1997) 121.
[106] G. Renaud, B. Villette, I. Vilfan, A. Bourret, Phys. Rev. Lett. 73 (1994) 1825.
[107] T.M. French, G.A. Somorjai, J. Phys. Chem. 74 (1970) 12.
[108] S. Baik, D.E. Fowler, J.M. Blakeley, R. Raj, J. Am. Ceram. Soc. 68 (1985) 281.
[109] M. Gautier, J.P. Duraud, L. Pham Van, M.J. Guittet, Surf. Sci. 250 (1991) 71.
[110] M. Gautier, J.P. Duraud, L. Pham Van, Surf. Sci. 249 (1991) L327.
[111] A.D. Novaco, J.P. McTague, Phys. Rev. Lett. 38 (1977) 1286; J.P. McTague, A.D. Novaco, Phys. Rev. B 19 (1979) 5299.
[112] H. Shiba, J. Phys. Soc. Jpn. 48 (1980) 211.
[113] E. Gillet, B. Ealet, Surf. Sci. 273 (1992) 427.
[114] M. Vermeersch, R. Sporken, Ph. Lambin, R. Caudano, Surf. Sci. 235 (1990) 5.
[115] G. Renaud, A. Barbier, M. Gautier-Soyer, unpublished results.
[116] G. Charlton, P.B. Howes, C.L. Nicklin, P. Steadman, J.S.G. Taylor, C.A. Muryn, S.P. Harte, J. Marcer, R. McGrath, D. Norman, T.S. Turner, G. Thornton, Phys. Rev. Lett. 78 (1997) 495.
[117] P.W. Murray, F.M. Leibsle, C.A. Muryn, H.J. Fisher, C.F.J. Flipse, G. Thornton, Phys. Rev. Lett. 72 (1994) 689.
[118] P.W. Murray, N.G. Condon, G. Thornton, Phys. Rev. B 51 (1995) 10989.
[119] H. Onishi, Y. Iwasawa, Phys. Rev. Lett. 76 (1996) 791.
[120] M. Ramamoorthy, D. Vanderbilt, R.D. King-Smith, Phys. Rev. B 49 (1994) 16721.
[121] D. Vogtenhuber, R. Podloucky, A. Neckel, S.G. Steinnemann, A.J. Freeman, Phys. Rev. B 49 (1994) 2099.
[122] P. Reinhardt, B.A. Hess, Phys. Rev. B 50 (1994) 12015.
[123] P. Zschack, J.B. Cohen, Y.W. Chung, Surf. Sci. 262 (1992) 395.
[124] H. Zajonz, H.L. Meyerheim, T. Gloege, W. Moritz, D. Wolf, unpublished.
[125] Y.W. Chung, W.J. Lo, G.A. Somorjai, Surf. Sci. 64 (1977) 588.
[126] L.E. Firment, Surf. Sci. 116 (1980) 205.
[127] P.J. Hardman, N.S. Prakash, C.A. Muryn, G.N. Raikar, A.G. Thomas, A.F. Prime, G. Thornton, R.J. Blake, Phys. Rev. B 47 (1993) 16056.
[128] P.W. Murray, F.M. Leibsle, H.J. Fisher, C.F.J. Flipse, C.A. Muryn, G. Thornton, Phys. Rev. B 46 (1992) 12877.
[129] G.W. Clark, L.L. Kesmodel, Ultramicroscopy 41 (1992) 77.
[130] A. Barbier, G. Renaud, Surf. Sci. 392 (1997) L15.
[131] S. Soeya, S. Nakamura, T. Imagawa, S. Narishige, J. Appl. Phys. 77 (1995) 5838.
[132] D.M. Lind, S.-P. Tay, S.D. Berry, J.A. Borchers, R.W. Erwin, J. Appl. Phys. 73 (1993) 6886.
[133] D. Cappus, C. Xu, D. Ehrlich, B. Dillmann, C.A. Ventrice et al., Chem. Phys. 177 (1993) 533.
[134] D. Wolf, Phys. Rev. Lett. 68 (1992) 3315.
[135] P.M. Oliver, G.W. Watson, S.C. Parker, Phys. Rev. B 52 (1995) 5323.
[136] C.A. Ventrice, Jr., Th. Bertrams, H. Hannemann, A. Brodde, H. Neddermeyer, Phys. Rev. B 49 (1994) 5773.
[137] F. Rohr, K. Wirth, J. Libuda, D. Cappus, M. Bäumer, H.J. Freund, Surf. Sci. 315 (1994) L977.
[138] J.E. Keem, J.M. Honig, L.L. Van Zandt, Phil. Mag. B 37 (1978) 537.
[139] A. Barbier, G. Renaud, A. Stierle, Surf. Sci. 402–404 (1998) 757.
[140] W.C. Mackrodt, Phys. Chem. Miner. 15 (1988) 228.
[141] N. Bickel, G. Schmidt, K. Heinz, K. Muller, Phys. Rev. Lett. 62 (1989) 2009.
[142] G. Thornton, personal communication.
[143] Z. Liu, S. Ogota, T. Morishita, Proc. SPIE 2696 (1996) 627.
[144] G. Charlton, Ph.D. Thesis, Manchester University, 1997.

[145] V. Ravikumar, D. Wolf, V.P. Dravid, Phys. Rev. Lett. 74 (1995) 960.
[146] W.C. Mackrodt, Phys. Chem. Miner. 15 (1988) 1674.
[147] A. Jiang, J. Zegenhagen, Surf. Sci. 367 (1996) L42.
[148] J. Zegenhagen, personal communication.
[149] A. Kazimirov, J. Zegenhagen, I. Denk, J. Maier, D.-M. Smilgies, R. Feidenhans'l, Surf. Sci. 352 (1996) 875.
[150] W. Moritz, personal communication.
[151] J.H. van der Merwe, Phil. Mag. A 45 (1982) 127, 145, 159.
[152] T. Epicier, C. Esnouf, J. Phys. III 4 (1994) 1811.
[153] R.H. Hoel, H.-U. Habermeier, M. Rühle, J. Phys. 46 (1989) C4-141; R.H. Hoel, Surf. Sci. 169 (1986) 317; R.H. Hoel, J.M. Penisson, H.U. Habermeier, J. Phys. 51 (1989) C1-837.
[154] F. Ernst, P. Pirouz, A.H. Heuer, Phil. Mag. A 63 (1991) 259.
[155] G. Necker, W. Mader, Phil. Mag. Lett. 58 (1988) 205.
[156] P. Guénard, G. Renaud, B. Villette, Physica B 221 (1996) 205.
[157] O. Robach, G. Renaud, A. Barbier, P. Guénard, Surf. Rev. Lett. 5 (1998) 359.
[158] C. Li, Ruqian Wu, A.J. Freeman, C.L. Fu, Phys. Rev. B 48 (1993) 8317.
[159] U. Schonberger, O.K. Andersen, M. Methfessel, Acta Metall. Mater. 40 (1992) S1.
[160] P. Bloch et al., in: M. Rühle, A.G. Evans, M.F. Ashby, J.P. Hirth (Eds.), Metal–Ceramic Interfaces, Pergamon Press, Oxford, 1990.
[161] J.R. Smith, T. Hong, D.J. Srolovitz, Phys. Rev. Lett. 72 (1994) 4021.
[162] A.M. Flanck, R. Delaunay, P. Lagarde, M. Pompa, J. Jupille, Phys. Rev. B 53 (1996) 1737.
[163] L. Spiess, Surf. Rev. Lett. 3 (1997) 1365.
[164] A. Trampert, F. Ernst, C.P. Flynn, H.F. Fischmeister, M. Rühle, Acta Metall. Mater. 40 (1992) S227.
[165] H.A. van der Vegt, H.M. van Pinxteren, M. Lohmeier, E. Vlieg, J.M.C. Thornton, Phys. Rev. Lett. 68 (1992) 3335.
[166] H.A. van der Vegt, W.J. Huisman, P.B. Howes, E. Vlieg, Surf. Sci. 330 (1995) 101.
[167] H.A. van der Vegt, J. Alvarez, X. Torrelles, S. Ferrer, E. Vlieg, Phys. Rev. B 52 (1995) 17443.
[168] T.C.Q. Noakes et al., Surf. Sci. 307–309 (1994) 101.
[169] J. Massies, N. Grandjean, Phys. Rev. Lett. 71 (1993) 1411.
[170] M. Horn-von-Hoege et al., Phys. Rev. Lett. 71 (1993) 3170.
[171] G. Renaud, A. Barbier, unpublished results.
[172] C.R. Henry, Surf. Sci. Rep. 31 (1998) 231; C. Goyhenex, M. Croci, C. Claeys, C.R. Henry, Surf. Sci. 353 (1996) 475.
[173] S.G. Giorgio, C. Chapon, C.R. Henry, G. Nihoul, Phil. Mag. B 67 (1993) 773.
[174] C. Goyhenex, M. Meunier, C.R. Henry, Surf. Sci. 350 (1996) 103.
[175] C.R. Henry, C. Chapon, C. Duriez, S. Giorgio, Surf. Sci. 253 (1991) 177.
[176] C. Goyhenex, C.R. Henry, J. Urban, Phil. Mag. A 69 (1994) 1073.
[177] C.R. Henry, M. Meunier, S. Morel, J. Cryst. Growth 129 (1993) 416.
[178] S. Bartuschat, J. Urban, Phil. Mag. A 76 (1997) 783.
[179] P. Lu, F. Cosandey, Acta Metall. Mater. 40 (1992) S259.
[180] K. Heinemann, T. Osaka, H. Poppa, M. Avalos-Borja, J. Catal. 83 (1983) 61.
[181] H. Fornander, J. Birch, L. Hultman, L.-G . Petersson, J.-E. Sundgren, Appl. Phys. Lett. 68 (1996) 2636.
[182] C. Goyhenex, C.R. Henry, J. Electron Spectrosc. Rel. Phen. 61 (1992) 65.
[183] J. Goniakovsky, Phys. Rev. B 57 (1998) 1.
[184] A. Barbier, G. Renaud, O. Robach, submitted.
[185] H. Bialas, K. Heneka, Vacuum 45 (1994) 79.
[186] F. Reniers, M.P. Delplancke, A. Asskali, V. Rooryck, O. Van Sinay, Appl. Surf. Sci. 92 (1996) 35.
[187] G. Raatz, J. Woltersdorf, Phys. Status Solidi 113 (1989) 131.
[188] H. Nakai, H. Qiu, M. Adamik, G. Sáfran, P.B. Barna, M. Hashimoto, Thin Solid Films 263 (1995) 159.
[189] R.H. Hoel, J.M. Penisson, H.U. Habermeier, Coll. Phys. 51 (1990) C1-837.
[190] H. Sato, R.S. Toth, R.W. Astrue, J. Appl. Phys. 33 (1962) 1113.
[191] A.A. Hussain, J. Phys.: Condens. Matter 1 (1989) 9833.
[192] H. Bialas, Li-Shing Li, Phys. Status Solidi 42 (1977) 125.
[193] N.I. Kiselev, Yu.I. Man'kov, V.G. Pyn'ko, Sov. Phys. Solid State 31 (1989) 685.
[194] H. Maruyama, H. Qiu, H. Nakai, M. Hashimoto, J. Vac. Sci.Technol. A 13 (1995) 2157.

[195] H. Qiu, A. Kosuge, H. Maruyama, M. Adamik, G. Safran, P.B. Barna, M. Hashimoto, Thin Solid Films 241 (1994) 9.
[196] M.R. Fitzsimmons, G.S. Smith, R. Pynn, M.A. Nastasi, E. Burkel, Physica B 198 (1994) 169.
[197] B.M. Lairson, A.P. Payne, S. Brennan, N.M. Rensing, B.J. Daniels, B.M. Clemens, J. Appl. Phys. 78 (1995) 4449.
[198] G. Charlton, P.B. Howes, C.A. Muryn, H. Raza, N. Jones, J.S.G. Taylor, C. Norris, R. McGrath, D. Norman, T.S. Turner, G. Thornton, submitted.
[199] G. Pacchioni, N. Rösch, J. Chem. Phys. 104 (1996) 7329
[200] N.C. Bacalis, A.B. Kunz, Phys. Rev. B 32 (1985) 4857
[201] A.M. Ferrari, G. Pacchioni, J. Phys. Chem. 100 (1996) 9032.
[202] N. Rösch, G. Pacchioni, in: R.U. Lambert, G. Pacchioni (Eds.), Chemisorption and Reactivity on Supported Clusters, Thin Films, Kluwer Academic Publishers, Dordrecht, 1997, p. 353.
[203] C.R. Henry et al., unpublished results.
[204] C.H. Lee, K.S. Liang, Acta Metall. Mater. 40 (1992) S143.
[205] C.H. Lee, K.S. Liang, F.S. Shieu, S.L. Sass, C.P. Flynn, Mater. Res. Soc. Symp. Proc. 209 (1991) 679.
[206] J. Mayer, C.P. Flynn, M. Rühle, Ultramicroscopy 33 (1990) 51.
[207] C.P. Flynn, in: M. Rühle, A.G. Evans, M.F. Ashby, J.P. Hirth (Eds.), Metal–Ceramic Interfaces, Pergamon Press, New York, 1990.
[208] J. Mayer, G. Gutekunst, G. Möbus, J. Dura, C.P. Flynn, M. Rühle, Acta Metall. Mater. 40 (1992) S217.
[209] P. Guénard, G. Renaud, B. Villette, M.H. Yang, C.P. Flynn, Scripta Metall. Mater. 31 (1994) 1221.
[210] G. Renaud, P. Guénard, A. Barbier, Phys. Rev. B, in press.
[211] M.S. Patterson, J. Appl. Phys. 8 (1952) 805.
[212] Goldsmith, Waterman, Hirschorn (Eds.), Handbook of Thermophysical Properties of Solid Materials, vol. 3, MacMillan, New York, 1961.
[213] R. Bonnet, Phil. Mag. A 43 (1981) 1165.
[214] R. Bonnet, J.L. Verger-Gaugry, Phil. Mag. A 66 (1992) 849.
[215] E. Matsubara, Y. Waseda, K.T. Jacob, J. Mater. Sci. Lett. 10 (1991) 677.
[216] D.G. Walmsley, H.F. Sakeek, T. Morrow, C. Rowan, R.J. Turner, Mater. Sci. Eng. B 13 (1992) 15.
[217] G. Ockenfuss, F. Baudenbacher, W. Prusseit-Elffroth, K. Hirata, P. Berbereich, H. Kinder, Physica C 180 (1991) 30.
[218] H. Asami, Y. Watanabe, Jpn. J. Appl. Phys. 33 (1994) L1073.
[219] R.J. Gaboriaud, E. Salmon, S. Benayoun, J. All. Comp. 195 (1993) 259.
[220] Q.D. Jiang, K.G. Huang, M. Rao, J. Zegenhagen, Physica C 235(1994) 677.
[221] T. Kamigaki, H. Terauchi, T. Terashima, Y. Bando, K. Iijima, K. Yamamoto, K. Hirata, K. Hayashi, I. Nakagawa, Y.J. Tomii, Appl. Phys. 69 (1991) 3653.
[222] J.D. Budai, R.T. Young, B.S. Chao, Appl. Phys. Lett. 62 (1993) 1836.
[223] J. Zegenhagen, Surf. Sci. Rep. 18 (1993) 199.
[224] J. Zegenhagen, T. Siegrist, E. Fontes, L.E. Berman, J.R. Patel, Solid State Commun. 93 (1995) 763.
[225] Youngtae-Kim, Y.J. Song, K.H. Koh, J. Korean. Phys. Soc. 28 (1995) 369.
[226] C. Dubourdieu, J.P. Senateur, O. Thomas, F. Weiss, B.P. Thrane, M. Brunel, Appl. Phys. Lett. 69 (1996) 1942.
[227] Q.D. Jian, D.M. Smilgies, R. Feidenhans'l, M. Cardona, J. Zegenhagen, Solid State Commun. 98 (1996) 157.
[228] J. Brötz, H. Fuess, T. Haage, J. Zegenhagen, Phys. Rev. B 57 (1998) in print.
[229] J.H. Lee, W.K. Choo, Y.S. Kim, D.W. Yun, J. Appl. Phys. 75 (1994) 2455.
[230] N. Ishizawa, M. Hayashi, H. Banno, S. Mizunuma, H. Yamagutchi, S.E. Yoo, M. Yoshimura, Report of the Research Laboratory of Engineering Materials, Tokyo Institute of Technology 16 (1991) 9.
[231] E. Sanchez-Carambot, L.J. Martinez-Miranda, E. Smela, Y. Shi, J.J. Santiago-Aviles, in: E.R. Myers, A.I. Kingon (Eds.), Ferroelectric Thin Film Symposium, vol. 205, 1990,
[232] T. Kosaka, S. Suzuki, M. Saito, Y. Waseda, E. Matsubara, K. Sadamori, E. Aoyagi, Thin Solid Films 289 (1996) 1.
[233] G. Marest, S.B. Ogale, B. Hannoyer, S. Joshi, A. Benyagoub, N. Moncoffre, J. Appl. Phys. 80 (1996) 2228.
[234] T. Kosaka, S. Suzuki, H. Inoue, M. Saito, Y. Waseda, E. Matsubara, Appl. Surf. Sci. 103 (1996) 55.
[235] A. Atkinson, Rev. Mod. Phys. 57 (1985) 437.
[236] C. Xu, M. Hassel, H. Kuhlenbeck, H.-J. Freund, Surf. Sci. 258 (1991) 23.
[237] A. Stierle, P. Bödeker, H. Zabel, Surf. Sci. 327 (1995) 9.
[238] A. Stierle, Ph.D. Thesis, Ruhr-Universität Bochum, 1996.
[239] A. Stierle, H. Zabel, Europhys. Lett. 37 (1997) 365.

[240] A. Stierle, H. Zabel, Surf. Sci. 385 (1997) 167.
[241] A. Stierle, H. Zabel, Surf. Sci. 385 (1997) 310.
[242] A. Stierle, Private communication.
[243] J.S. Zabinski, M.S. Donley, V.J. Dyhouse, R. Moore, N.T. McDevitt, in: Phase Formation and Modification by Beam–Solid Interactions Symposium, Mater. Res. Soc. Proc. 849 (1992).
[244] C. Agashe, M.G. Takwale, V.G. Bhide, S. Mahamuni, S.K. Kulkarni, J. Appl. Phys. 70 (1991) 7382.
[245] J.L. Vassent, M. Dynna, A. Marty, B. Gilles, G. Patrat, J. Appl. Phys. 80 (1996) 5727.
[246] H. Wulff, J. Klimke, E. Gerova, Surf. Interf. Anal. 23 (1995) 148.
[247] M. Saito, T. Kosaka, E. Matsubara, Y. Waseda, Mater. Trans. JIM 36 (1995) 1.
[248] T.A. Crabb, P.N. Gibson, E. McAlpine, Corrosion Sci. 34 (1993) 1541.
[249] E.D. Specht, C.J. Sparks, C.J. McHargue, Appl. Phys. Lett. 60 (1992) 2216.
[250] S.G. Ghonge, E. Goo, R. Ramesh, T. Sands, V.G. Keramidas, Appl. Phys. Lett. 63 (1993) 1628.
[251] K.S. Kim, I.S. Choi, Y.S. Lee, Y.W. Kim, S.S. Kim, H.K. Kim, D.W. Moon, C.N. Whang, Nucl. Instr. Meth. Phys. Res. B 80/81 (1993) 1300.
[252] A. Rizzo, L. Mirenghi, L. Tapfer, M. Alvisi, L. Vasanelli, F. Sarto, S. Scaglione, Proc. SPIE 2776 (1996) 392.
[253] W. Dmowski, T. Egami, R. Gorte, J. Vohs, Physica B 221 (1996) 420.
[254] G.M. Watson, D. Gibbs, G.H. Lander, B.D. Gaulin, H. Matzke, W. Ellis, Physica B 221 (1996) 405.
[255] G.M. Watson, D. Gibbs, G.H. Lander, B.D. Gaulin, H. Matzke, W. Ellis, Phys. Rev. Lett. 77 (1996) 751.
[256] R. Persaud, T.E. Madey, in: The Physical Chemistry of Solid Surfaces, vol. 8, Elsevier, Amsterdam, 1997, p. 407.
[257] N. Rösch, G. Pacchioni, in: R.U. Lambert, G. Pacchioni (Eds.), Chemisorption and Reactivity on Supported Clusters and Thin Films, Kluwer Academic Publishers, Dordrecht, 1997, p. 353.
[258] F. Widmann, R. Langer, B. Daudin, G. Feuillet, A. Barski, unpublished.
[259] N. Jedrecy, Personal communication.
[260] M. Gautier-Soyer, Personal communication.